Optimal Aerodynamic Design of Conventional and Coaxial Helicopter Rotors in Hover and Forward Flight

by

Eli B. Giovanetti

Department of Mechanical Engineering and Materials Science
Duke University

Date: _____

Approved:

_____
Kenneth C. Hall, Supervisor

_____
Earl H. Dowell

_____
Laurens E. Howle

_____
Donald B. Bliss

_____
Thomas P. Witelski

Dissertation submitted in partial fulfillment of the requirements
for the degree of Doctor of Philosophy in the
Department of Mechanical Engineering and Materials Science
in the Graduate School of Duke University
2015

Abstract

Optimal Aerodynamic Design of Conventional and Coaxial Helicopter Rotors in Hover and Forward Flight

by

Eli B. Giovanetti

Department of Mechanical Engineering and Materials Science
Duke University

Date: _____

Approved:

_____
Kenneth C. Hall, Supervisor

_____
Earl H. Dowell

_____
Laurens E. Howle

_____
Donald B. Bliss

_____
Thomas P. Witelski

An abstract of a dissertation submitted in partial fulfillment of the requirements for the degree of Doctor of Philosophy in the Department of Mechanical Engineering and Materials Science
in the Graduate School of Duke University
2015

Abstract

This dissertation investigates the optimal aerodynamic performance and design of conventional and coaxial helicopters in hover and forward flight using conventional and higher harmonic blade pitch control. First, we describe a method for determining the blade geometry, azimuthal blade pitch inputs, optimal shaft angle (rotor angle of attack), and division of propulsive and lifting forces among the components that minimize the total power for a given forward flight condition. The optimal design problem is cast as a variational statement that is discretized using a vortex lattice wake to model inviscid forces, combined with two-dimensional drag polars to model profile losses. The resulting nonlinear constrained optimization problem is solved via Newton iteration. We investigate the optimal design of a compound vehicle in forward flight comprised of a coaxial rotor system, a propeller, and optionally, a fixed wing. We show that higher harmonic control substantially reduces required power, and that both rotor and propeller efficiencies play an important role in determining the optimal shaft angle, which in turn affects the optimal design of each component. Second, we present a variational approach for determining the optimal (minimum power) torque-balanced coaxial hovering rotor using Blade Element Momentum Theory including swirl. We show that the optimal hovering coaxial rotor generates only a small percentage of its total thrust on the portion of the lower rotor operating in the upper rotor's contracted wake, resulting in an optimal design with very different upper and lower rotor twist and chord distributions. We also show

that the swirl component of induced velocity has a relatively small effect on rotor performance at the disk loadings typical of helicopter rotors. Third, we describe a more refined model of the wake of a hovering conventional or coaxial rotor. We approximate the rotor or coaxial rotors as actuator disks (though not necessarily uniformly loaded) and the wake as contracting cylindrical vortex sheets that we represent as discrete vortex rings. We assume the system is axisymmetric and steady in time, and solve for the wake position that results in all vortex sheets being aligned with the streamlines of the flow field via Newton iteration. We show that the singularity that occurs where the vortex sheet terminates at the edge of the actuator disk is resolved through the formation of a 45° logarithmic spiral in hover, which results in a non-uniform inflow, particularly near the edge of the disk where the flow is entirely reversed, as originally hypothesized by previous authors. We also quantify the mutual interference of coaxial actuator disks of various axial spacing. Finally, we combine our forward flight optimization procedure and the Blade Element Momentum Theory hover optimization to form a variational approach to the multipoint aerodynamic design optimization of conventional and coaxial helicopter rotors. The resulting nonlinear constrained optimization problem may be used to map the Pareto frontier, i.e., the set of rotor designs for which it is not possible to improve upon the performance in one flight condition without degrading performance in the other. We show that for both conventional and coaxial rotors analyzed in hover and high speed flight, a substantial tradeoff in performance must be made between the two flight conditions. Finally, computational results demonstrate that higher harmonic control is able to improve the Pareto efficiency for both conventional and coaxial rotors.

Contents

List of Tables

List of Figures

List of Abbreviations and Symbols

Symbols for Forward Flight, Hover, and Multipoint Optimization

A	Rotor disk area, πR^2
$\mathbf{A}$	Matrix relating control inputs $\boldsymbol{\theta}$ to circulation $\boldsymbol{\Gamma}$
A_n	nth Fourier coefficient of blade pitch
B_n	nth Fourier coefficient of blade pitch
B	Number of blades
$\mathbf{B}$	Matrix relating force $\mathbf{F}$ to circulation $\boldsymbol{\Gamma}$
C_{Fx}	Propulsive force coefficient, $F_x/\rho A\Omega^2 R^2$
C_L	Lift coefficient, $L/\rho A\Omega^2 R^2$
C_T	Thrust coefficient, $T/\rho A\Omega^2 R^2$
C_Q	Torque coefficient, $Q/\rho A\Omega^2 R^3$
C_P	Power coefficient, $P/\rho A\Omega^3 R^3$
c_d	Airfoil sectional drag coefficient
c_ℓ	Airfoil sectional lift coefficient
$c_{\ell\alpha}$	Lift curve slope
c	Blade chord
$\mathbf{D}$	Matrix relating moment $\mathbf{M}$ to circulation $\boldsymbol{\Gamma}$
D	Drag
E	Kinetic energy per period in wake
F	Prandtl tip loss factor

$\mathbf{F}$	Time-averaged aerodynamic force vector
k	Empirically determined parameter used in the mutual interference model
$\mathbf{K}$	Quadratic power matrix
L	Vehicle lift
M	Number of quadrilateral elements in the vortex lattice wake
$\mathbf{M}$	Time-averaged aerodynamic moment vector
N	Number of harmonics in higher harmonic control
n	Fourier coefficient index
$\mathbf{n}$	Unit vector normal to wake surface
P	Power
$\mathbf{P}_{V\Gamma}$	Gradient of profile power $\mathbf{P}_V$ with respect to the circulation $\boldsymbol{\Gamma}$
$\mathbf{P}_{V\theta}$	Gradient of profile power $\mathbf{P}_V$ with respect to design variables $\boldsymbol{\theta}$
Q	Torque
r	Radial position
R	Rotor radius
$\mathbf{R}$	Vector function describing the relationship between the circulation $\boldsymbol{\Gamma}$ and the control inputs $\boldsymbol{\theta}$
$\mathbf{R}_\Gamma$	Jacobian of $\mathbf{R}$ with respect to $\boldsymbol{\Gamma}$
$\mathbf{R}_\theta$	Jacobian of $\mathbf{R}$ with respect to $\boldsymbol{\theta}$
R_{CO}	Root cutout radius
$\mathbf{r}$	Moment arm from vehicle center to lifting surface
T	Temporal period of the wake, or thrust
u	Relative fluid velocity perpendicular to span
U	Inflow velocity
w	Axial induced wash velocity
V	Vehicle forward speed, or airspeed relative to the airfoil

$\mathcal{W}$	Wake sheet surface
$\mathbf{w}$	Induced velocity in far wake
α	Weighting parameter
β	Weighting parameter, $1 - \alpha$
α_{eff}	Effective angle of attack
α_{shaft}	Rotor disk angle of attack
δ	Variational operator
Γ	Circulation
γ	Vorticity
θ_0	Fixed blade twist distribution
θ	Blade pitch angle
$\boldsymbol{\theta}$	Vector of design variables
$\boldsymbol{\lambda}$	Equality constraint Lagrange multiplier
$\boldsymbol{\lambda}_F$	Lagrange multiplier for force constraint
$\boldsymbol{\lambda}_M$	Lagrange multiplier for moment constraint
$\boldsymbol{\lambda}_R$	Lagrange multiplier for vector function $\mathbf{R}$
$\boldsymbol{\lambda}_Q$	Lagrange multiplier for torque balance constraint
$\boldsymbol{\lambda}_T$	Lagrange multiplier for thrust constraint
λ	Total axial inflow velocity, $U + w$
μ	Advance ratio, $V/\Omega R$
ν_Q	Lagrange multiplier for torque balance constraint in hover optimization
ν_T	Lagrange multiplier for thrust constraint in hover optimization
$\boldsymbol{\xi}$	Kelvin linear impulse
Π	Power Lagrangian
ρ	Fluid density

σ	Rotor solidity, $Bc/\pi R$
σ_{TW}	Thrust weighted rotor solidity
σ_{TWM}	Modified thrust weighted rotor solidity
ϕ	Velocity potential function, or, relative flow angle
ψ	Azimuthal angle
Ω	Rotor rotational speed
$\bar{()}$	Non-dimensional quantity

Symbols for Actuator Disk Wake Model (Chapter 4)

$\mathbf{ds}$	Distance between successive vortex rings
m	Constant used to set spacing of vortex rings
$\dot{m}$	Mass flow rate
r	Radius of a vortex ring
$\mathbf{R}$	Residual vector
u	x (radial) component of induced velocity
V_c	Axial free stream velocity; positive indicates climbing flight, negative descending flight
V_i	Induced velocity at the actuator disk
$\mathbf{V}$	Induced velocity field
w	z (axial) component of induced velocity
$\boldsymbol{\theta}$	Vector of angles between a segment of the vortex sheet and the positive x axis

Subscripts

c	Contracted quantity
i	Induced
ℓ	Lower

max	Maximum value
prop	Variable associated with the propeller
R	Prescribed value
req	Prescribed value in hover optimization
rotor	Variable associated with the rotor system
tot	Total
u	Upper
v	Viscous
z	A position or velocity associated with the axial direction
θ	A position or velocity associated with the circumferential (swirl) direction

Superscripts

k	Iteration number

Abbreviations

LOS	Lift offset, $\Delta M_x/LR$ where ΔM_x is the roll moment
FOM	Figure of Merit

Acknowledgements

I would like to thank Dr. Kenneth Hall for his invaluable technical support, mentorship, and patience over the last four and a half years. I would also like to thank my entire committee for their support and guidance: Dr. Donald Bliss, Dr. Earl Dowell, Dr. Laurens Howle, and Dr. Thomas Witelski. Outside of Duke, I would like to thank Dr. Robert Ormiston for his technical expertise and support of this work, particularly in its early stages. I would like to thank my colleagues in the MEMS program for making my graduate career a fun and (at times) productive pursuit. I owe a great deal to my parents, Kevin and Lisa, for their unconditional support. Finally, a special thanks to my fiancèe Caitlin for being with me every step of the way.

I was fortunate enough to receive financial support from many sources, for which I am very thankful. Thanks to the Pratt-Gardner first year fellowship at Duke University for support in 2011-2012. The early portions of this work (2012) were funded in part by a contract from Sikorsky Aircraft Corporation, whose support is gratefully acknowledged. Thanks to the Vertical Flight Foundation for a scholarship in 2013 and the National Defense Science and Engineering (NDSEG) fellowship for full financial support of my graduate studies from 2013 - 2015. Lastly, thanks to the U.S. Army Research Office for their support of this work under Award No. W911NF-13-1-0469.

1

Introduction

Helicopters are versatile vehicles that can perform a large variety of missions outside the capabilities of a fixed wing aircraft. The ability to take off and land vertically, as well as to operate in hovering flight for extended periods of time, are crucial for a variety of civilian and military applications. However, conventional helicopters are inefficient in forward flight relative to fixed wing aircraft, in part because the asymmetric wake structure of a conventional rotor leads to larger than ideal induced power losses [1, 2]. Other factors, such as advancing blade compressibility and retreating blade stall, also contribute to the inefficiency of conventional rotors in forward flight, thus limiting their top speed [3, 4].

One method to improve the forward flight performance of a helicopter is by compounding the thrust of the rotor with a second source of propulsion, often in the form of a propeller. This arrangement, which is known as a compound helicopter, combines the hover capabilities of a helicopter with substantially improved aerodynamic performance in high speed flight, both in terms of reduced power requirements and increased maximum speed [1, 5, 6, 7]. Compound configurations also frequently include a wing to supplement the lift of the rotor in high speed flight. Compounding

FIGURE 1.1: Eurocopter X3 compound helicopter, which uses a lifting wing with two propellers for auxilliary propulsion [10].

both the thrust and lift of the vehicle allows the rotor to be slowed and offloaded in high speed flight, reducing losses due to compressibility and stall [7]. Additionally, eliminating the requirement that the rotor be indepently trimmed (as the rotor rolling moment can be counteracted by an equal and opposite moment from the wing) can also reduce the high induced power losses of the rotor at high advance ratios [1]. The Cheyenne helicopter of the late 1960's used a rotor and wing in combination with a pusher propeller to achieve a maximum speed of over 200 knots [8]. More recently, the Eurocopter X3 compound helicopter, shown in Figure 1.1, achieved speeds of 255 knots in level, stabilized flight [9] with a design using two propellers and a conventional rotor.

A coaxial rotor is defined as a pair of counter-rotating rotors that rotate about a common shaft axis. Coaxial rotors have an extensive history dating back to some of the earliest vertical flight vehicles. In fact, Igor Sikorsky had built a non-piloted coaxial prototype by 1909, and many other early attempts at sustained vertical flight involved coaxial rotors [3]. In 1930, Corradine d'Asconio built a coaxial helicopter capable of controlled flight [3]. The Russian helicopter manufacturer Kamov has built a succesful line of coaxial rotor helicopters beginning in the late 1940's, although the

Kamov coaxial helicopters do not use an auxiliary source of propulsion and are not designed for high speed.

In the 1970's, the Sikorsky X-59 made use of a coaxial, rigid rotor in combination with an external propulsor in a system referred to as the Advancing Blade Concept (ABC) [11]. The ABC achieves improved forward flight efficiency by offloading the retreating side of each rotor in high speed flight, achieving roll trim by balancing the moments transmitted to the hub by the opposing advancing side blades. This arrangement results in each rotor carrying a lateral lift offset (LOS), wherein the majority of lift is generated on the advancing side of each rotor. The resulting wake structure is symmetric and is naturally trimmed in roll, resulting in low induced power requirements at high speeds [1]. Additionally, eliminating the need to operate each rotor as independently trimmed results in a decrease in profile power losses, as the retreating side can be offloaded, and allows for the rotor to be slowed in high speed flight, reducing compressibility losses on the advancing side [12]. The X-59 was designed for high speed flight and was originally designed to include turbine engines for auxiliary propulsion, thus making the vehicle a true compound.

While the X-59 never went into production, Sikorsky's X2 Technology Demonstrator (X2 TD) recently revitalized the ABC with updated technologies. The X2 TD, as described by Bagai [12] and shown in Figure 1.2, used a rigid coaxial rotor system with a pusher propeller to achieve speeds of 250 knots in level flight [13] in 2010. The ABC concept successfully demonstrated on the X2 TD is being used on Sikorsky's next generation verticle lift vehicles, including the S-97 Raider and SB-1 Defiant, the latter of which will be an entry to the US Army's Joint Multirole program [14].

Another benefit of coaxial helicopters, in addition to their high speed performance, is that they are more efficient in hover compared to two isolated single rotors of the same area [16]. Several authors have investigated the performance of

FIGURE 1.2: Sikorsky X2 technology demonstrator, which uses a coaxial rotor and a pusher propeller [15].

coaxial rotors in hover, often arriving at differing conclusions about optimal rotor design [17, 18, 19, 20, 21]. Coaxial helicopters also have the added benefits of eliminating the need for an anti-torque device, thus saving additional power. Finally, coaxial rotors allow for a larger lift capacity for a given rotor diameter, which can be an advantage in applications where vehicle size is constrained by its total "footprint," for example in Naval applications.

A sizeable body of research seeks to model and improve the performance of compound helicopters, including those using coaxial rotors. Much of the work uses the comprehensive rotor code CAMRAD II to explore compound vehicle performance and optimal design [7, 16, 22, 23, 24]. Other authors, including Orchard and Newman [6], Ormiston [5], and Rand and Khromov [25], have used various analytical and numerical approaches to understand the optimal design and performance of compound helicopters.

Higher harmonic control (HHC) is defined as using harmonic pitch inputs to the blade in addition to the traditional zero and one per revolution control typically achieved with a swashplate. Historically, HHC has been studied for its applications to vibration or noise reduction. However, many researchers have also investigated its potential effectiveness at improving the aerodynamic performance of conventional

rotors in forward flight, through both analytical and numerical methods [26, 27, 28, 29, 30, 31, 32, 33, 34, 35] and through experiments [36, 37, 38]. In general, these analyses have found that HHC can reduce both the induced and profile components of power for a conventional rotor in forward flight, with an increased potential for aerodynamic performance improvement at higher advance ratios.

Hall and Hall [1], building upon their work on the minimum induced loss lift distribution of helicopters in forward flight [31], used a variational approach to compute the theoretically optimal aerodynamic performance of conventional and coaxial rotors in trimmed high speed flight. They found that the power required for coaxial and wing-rotor compounds can be substantially reduced by producing a more efficient wake structure and by reducing the induced power associated with roll trim. The resulting analysis – which is the viscous helicopter rotor analogue of Goldstein's inviscid propeller theory [39] – gives rigorous upper bounds on the performance of conventional and coaxial helicopters, and may be used to predict the rotor loadings that produce optimal performance. Their analysis does not consider the specific rotor design required to achieve the optimal circulation distribution; rather, it assumes a "rubber rotor" that can be articulated with unlimited degrees of freedom to achieve the desired optimal circulation distribution.

Hall and Giovanetti [40] built upon this work to develop a method for computing the optimal rotor design for conventional and coaxial rotors in forward flight using conventional and higher harmonic control. Rather than determining the optimal rubber rotor result, the method solves for the specific design variables – including the blade geometry (radial blade twist and chord) and conventional and higher harmonic control of the blade pitch – that minimize the sum of induced and profile power losses while maintaining vehicle trim. Computed results show that for both conventional and counter-rotating coaxial rotors, using optimized twist and chord distributions substantially reduces total power compared to a zero-twist, constant-

chord blade. Additionally, higher harmonic blade pitch control substantially reduces required power, both with and without the use of optimized blade twist and chord distributions, particularly at high advance ratios. This work was also documented in more detail in the author's Master's thesis [41].

In the present work, we continue this line of research, focusing on four specific research topics, all broadly related to the optimal aerodynamic design and performance of conventional and coaxial helicopter rotors and compound vehicles. Specifically:

1. We investigate the optimal design of a compound vehicle in forward flight comprised of a coaxial rotor system, a propeller, and optionally, a fixed wing, and determine the optimal shaft angle, blade design, and division of propulsive and lifting forces. Additionally, we assess the performance benefits of higher harmonic control and the effects of a constrained lateral lift offset on optimal compound vehicle design and performance.

2. We investigate the optimal design and performance of a torque balanced coaxial rotor in hover or axial flight.

3. We develop a model of the axisymmetric trailing wake of single and coaxial actuator disks in axial flight or hover, allowing us to compute the mutual interference effects of coaxial actuator disks in hover. Additionally, we are able to confirm previous assertions about the nature of the terminating vortex sheet at the rim of an actuator disk, and visualize the flow field for single and coaxial actuator disks of various loadings and axial flight conditions.

4. We combine our forward flight and hover analysis to perform a multipoint optimization, capable of determining the conventional or coaxial rotor design that best balances performance between hover and a forward flight design point or two disparate forward flight design points.

Specifically, in Chapter 2, we extend the work on the optimal design of rotors in forward flight described by Hall and Giovanetti [40] to analyze the design and performance of the compound vehicle as a whole. We include in our model a propeller providing a propulsive force, and model a hypothetical fuselage drag using a propulsive force constraint. We investigate the minimum power requirements, optimal shaft angle, and optimal aerodynamic design of the compound helicopter as a system, including the rotor design, blade pitch inputs, shaft angle (rotor angle of attack), and division of propulsive and lifting forces among the components that minimize the total power for a given flight condition. We demonstrate the importance of both the propeller and rotor efficiencies in determining the optimal division of propulsive force between rotor and propeller, and the importance of shaft angle on high-speed performance and optimal rotor design. We show that higher harmonic control significantly reduces total vehicle power at high advance ratios. We also show that limiting the maximum lateral lift offset of the coaxial rotors to 30 percent of the rotor radius or less results in a substantial increase in power, and that the effectiveness of higher harmonic control to reduce these rotor power losses is dependent on shaft angle. This work was originally documented in [42, 43].

In Chapter 3 we present an approach for determining the optimal (minimum power) torque-balanced coaxial hovering rotor using Blade Element Momentum Theory including swirl. We quantify the effects of the swirl component of induced velocity on performance, optimal induced wash distribution, and optimal blade twist and chord. The optimization accounts for the presence of a finite number of blades using the Prandtl tip loss factor, the effect of profile drag using experimentally or computationally determined drag polars, and the mutual interference between the two rotors using an empirically determined influence coefficient method. We show that including the swirl component of induced wash decreases the optimal figure of merit and has a larger impact at higher disk loadings, as expected. However, at the

disk loadings typically found on helicopters, the effect of swirl is relatively small, particularly compared to other physical effects such as mutual interference or tip losses. This work was originally documented in [44].

In Chapter 4, we build a more refined model of the wake of a hovering conventional or coaxial rotor, in part to assess the validity of the simple mutual interference model used in the Chapter 3 hover optimization algorithm. We approximate the rotor or coaxial rotors as actuator disks (though not necessarily uniformly loaded) and the wake as contracting cylindrical vortex sheets that we represent as discrete vortex rings. We assume the system is axisymmetric and steady in time, requiring us to only analyze a single azimuthal slice of the flow field to determine the shape of the wake and the induced velocity throughout the flowfield. Using multiple vortex sheets allows us to analyze any piecewise constant bound circulation on the disk or disks. We solve for the positions of the vortex rings that result in no flow through the wake sheet via Newton iteration. Using this model, we confirm the findings of Spalart [45], who hypothesized that there exists a spiral wake structure near the edge of the actuator disk in which the vortex sheet itself passes through the disk multiple times. Additionally, we confirm several findings by previous authors, namely that the hovering or low axial velocity actuator disk has highly non-uniform induced inflow [45, 46, 47, 48], and includes a region of reversed flow near its edge [45, 46]. For coaxial actuator disks, we compute the mutual interference effects predicted by our vortex ring model and show that they are in reasonable agreement with the simple influence coefficient model of McAlister et al. [49] used in Chapter 3. This work is also documented in [50]

Finally, in Chapter 5, we present a variational approach to the multipoint aerodynamic design optimization of conventional and coaxial helicopter rotors. The compound vehicle optimization of Chapter 2 and the hover optimization of Chapter 3 determine the rotor geometry and pitch inputs that optimize performance at a single

design point. In Chapter 5, we minimize the weighted sum of induced and viscous power losses between two flight conditions for prescribed vehicle trim constraints at each flight condition. The resulting nonlinear constrained optimization problem may be used to map the Pareto frontier, i.e., the set of rotor designs (radial twist and chord distributions and harmonic blade pitch inputs) for which it is not possible to improve upon the performance in one flight condition without degrading performance in the other. The two flight conditions can represent different advance ratios (including hover), disk loadings, altitude, or other conditions of interest. For forward flight computations, the approach is the same as that described in Chapter 2. For hovering flight, the rotor performance is analyzed using Blade Element Momentum Theory without swirl, a slightly simplified version of the hover optimization described in Chapter 3. The use of the simpler model neglecting swirl is justified by the results of the Chapter 3 investigation. We map the Pareto frontier for both a cruise/cruise and hover/cruise multipoint optimization, and show that significant tradeoffs must be made in designing a rotor to balance performance between two flight conditions, particularly hover and high speed forward flight. We also show that higher harmonic control is capable of reducing rotor power and improving the Pareto frontier, particularly for coaxial rotors. This work was originally documented in [51].

2

Optimal Design of Compound Helicopters

In References [40, 41], Hall and Giovanetti developed a method for computing the blade geometry (radial blade twist and chord) and conventional and higher harmonic control of the blade pitch that minimize the sum of induced and profile power losses while maintaining vehicle trim. This analysis was applied to conventional rotors and coaxial rotors in forward flight, using conventional and higher harmonic control. The analysis included only the rotor system of a given vehicle, which was analyzed at a single representative shaft angle of $\alpha_{\text{shaft}} = -5°$. The rotor system was subject to trim constraints and a lift constraint; however, there was no requirement for the rotor to generate a propulsive force, which would be necessary in the actual operation of a helicopter to counteract fuselage drag and maintain steady, level flight.

For a helicopter without auxiliary propulsion, a propulsive force is generated by operating the rotor tilted in the direction of flight, i.e., at a negative shaft angle, thereby causing a component of the rotor's thrust vector to act in the horizontal direction. Within a compound vehicle using auxiliary propulsion, the propulsive force can be generated by some combination of forces generated by the rotor and

propeller. Interestingly, the rotor does not have to generate a positive force, but can be tilted aft and allowed to autorotate. This creates a force in the opposite direction of flight, but also requires less shaft power. The fact that in a compound vehicle there are redundant controls with which to achieve a given trimmed state allows for the required propulsive and lift forces to be generated at a variety of shaft angles and operating conditions.

In this chapter, we include a propeller in our helicopter model to provide a propulsive force, and include a propulsive force constraint to balance a hypothetical fuselage drag. We apply an updated version of our optimization algorithm to the entire compound helicopter, allowing us to investigate minimum power requirements, optimal shaft angle, and optimal aerodynamic design of the compound helicopter as a system.

A number of investigators have studied the performance of compound helicopters in high speed forward flight. Orchard and Newman [6] investigated fundamental design features of compound helicopters using a wing, a single rotor, and a propulsor. They noted that the efficiency of the propulsor will have a large effect on whether autorotating the rotor at high speeds is more efficient than powering the rotor. Bagai [12] described the aerodynamic design of the Sikorsky X2 Technology Demonstrator main rotor blades. Bagai noted that use of 2/rev harmonic control may prove beneficial in improving the aerodynamic efficiency of the coaxial rotors.

Ormiston [5], building on his previous work on the induced power of helicopter rotors [33, 34, 52], evaluated three configurations: a rotor using a wing, a rotor using auxiliary propulsion, and a rotor using both auxiliary propulsion and a wing. He determined that the case using both a wing and auxiliary propulsion had the best performance (i.e., the lowest required power). He also concluded that induced power losses significantly impact the aerodynamic efficiency of compound rotorcraft and are an important discriminator between high and low performance configurations. Johnson [16], Johnson, Moodie, and Yeo [23], Yeo and Johnson [22], and Russell

and Johnson [24] all analyzed the performance, sizing, and design of compound configurations to satisfy specific mission requirements using the comprehensive code CAMRAD II. Johnson [16] concluded that a lift offset of 0.25 of the rotor radius is effective in reducing rotor induced and profile power in high speed cruise.

Rand and Khromov [25] introduced a drag vs. power chart as a semi-analytic tool for understanding the effect of the rotor, propeller, wing, and fuselage contributions to propulsive force, drag, and the overall power required for compound configurations. The authors concluded that the optimal configuration is dependent on each component's efficiency, and that the optimal propulsive force balance occurs when the local rotor and propeller propulsive efficiencies, defined as the incremental change in propulsive force per unit change in required power, are equal.

Jacobellis et al. [53] used the comprehensive code RCAS to investigate the effect of varying controls such as rotor speed, auxiliary thrust, and differential lateral pitch on both required power and vibratory loads for the XH-59 Advancing Blade Concept demonstrator. The authors concluded that a reduction in power requirements of 17% was possible in the optimal trim state compared to the baseline trim state. This reduction in power was achieved by both slowing the rotor and increasing the lift offset to about 40%.

The results presented here demonstrate the importance of both the propeller and rotor efficiencies in determining the optimal division of propulsive force between rotor and propeller, and the importance of shaft angle on high-speed performance and optimal rotor design. We show that higher harmonic control significantly reduces total vehicle power at high advance ratios. We also show that limiting the maximum lateral lift offset of the coaxial rotors to 30 percent of the rotor radius or less results in a substantial increase in power, and that the effectiveness of higher harmonic control to reduce these rotor power losses is dependent on shaft angle. Lastly, we investigate the use of a lifting wing, as well as a propeller that provides some lift in addition

to thrust, and determine that each of these design features provide only marginal improvements in aerodynamic efficiency.

2.1 Technical Approach

The technical approach used in this paper follows References [40] closely and is briefly summarized in this section. We wish to determine the rotor, propeller, and wing design variables and control inputs that produce the minimum required power in forward flight. We assume light loading and/or high advance ratios, so a prescribed wake is appropriate. We assume high aspect ratio lifting surfaces, so the rotor blade, propeller, and wing geometries and control inputs can be related to the circulation in the wake using the rotorcraft equivalent of lifting line theory. Finally, we assume that the reduced frequency based on chord is small. Thus, the sectional lift and drag can be described using quasi-steady two-dimensional lift and drag curves found from experiment or using a computational fluid dynamic analysis. Alternatively, C-81 tables can be used to account accurately for the effect of Mach number on an airfoil's sectional lift and drag coefficients.

2.1.1 Forces, Moments, and Power

We calculate inviscid forces, moments, and induced power using a far-field approach. The forces and moments acting on the rotor/wing/propeller system are a result of apparent linear and angular momentum (i.e., Kelvin linear and angular impulses) deposited in the wake of each lifting component. The Trefftz volume bounds one period of the flow field in the far wake, bounded between two infinite parallel planes roughly transverse to the flight direction as shown in Fig. 2.1.

The far field flow is assumed to be inviscid, incompressible, and irrotational, except for the trailing and shed vorticity in the wake. Note that the assumption of incompressible flow requires only that the induced velocities in the wake be small

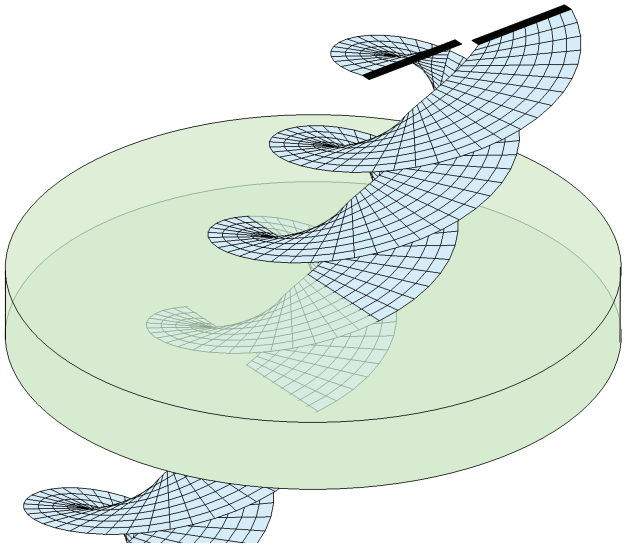

FIGURE 2.1: Schematic of prescribed wake showing one period of the far wake bounded by the Trefftz volume, from Reference [1].

compared to the speed of sound, an assumption consistent with the light loading model. (The flow *will* in general be compressible in the near field of the rotor.)

As discussed in References [1, 40], using these assumptions, the time-averaged force on the rotor is equal to

$$\mathbf{F} = -\frac{\boldsymbol{\xi}}{T} = \frac{\rho}{T} \iint_{\mathcal{W}} \Gamma \mathbf{n} \, dA \tag{2.1}$$

where the integral is taken over one side of the wake denoted by $\mathcal{W}$, Γ is the jump in potential (the circulation), $\mathbf{n}$ is the unit normal to the wake, and T is the temporal period of the wake, usually equal to $2\pi/\Omega B$ because only one B-th of a turn of the wake is required to achieve periodicity.

Likewise, the time-averaged moment acting on the system is equal to

$$\mathbf{M} = \frac{\rho}{T} \iint_{\mathcal{W}} \Gamma \, \mathbf{r} \times \mathbf{n} \, dA \tag{2.2}$$

where $\mathbf{r}$ is the moment arm extending from the center of the rotor system to the element of wake area at the time the wake is generated.

The induced power losses due to lift and thrust of a conventional helicopter rotor, or rotor/wing/propeller system for a compound helicopter, arise from the deposition of kinetic energy into the wake. The time-averaged induced power P_{i}, equal to the rate of kinetic energy production, is given by

$$P_{\mathrm{i}} = -\frac{\rho}{2T} \iint_{\mathcal{W}} \Gamma \mathbf{w} \cdot \mathbf{n} \, dA \tag{2.3}$$

where $\mathbf{w}$ is the induced velocity.

The profile power P_{v} may be expressed as the work per cycle divided by the period, so that

$$P_{\mathrm{v}} = \frac{1}{T} \iint_{\mathcal{W}} \frac{1}{2} \rho u^2 c c_d \, dA \tag{2.4}$$

where u is the relative velocity of a given airfoil section normal to the span of the rotor.

In discretized form, we represent the wake trace using a lattice of vortex rings, which can model both trailing and shed vorticity in the wake (see Figure 2.2). One period of the wake trace (the reference period) is divided into M quadrilateral elements. The ith element is a quadrilateral vortex ring with filament strength Γ_i. Thus, the potential jump across the ith element is just Γ_i, and the time-averaged force and moment on the helicopter may be approximated by

$$\mathbf{F} = \frac{\rho}{T} \sum_{i=1}^{M} \mathbf{n}_i \, \Delta A_i \Gamma_i = \sum_{i=1}^{M} \mathbf{b}_i \Gamma_i = \mathbf{B} \, \boldsymbol{\Gamma} \tag{2.5}$$

$$\mathbf{M} = \frac{\rho}{T} \sum_{i=1}^{M} \mathbf{r}_i \times \mathbf{n}_i \, \Delta A_i \Gamma_i = \sum_{i=1}^{M} \mathbf{d}_i \Gamma_i = \mathbf{D} \, \boldsymbol{\Gamma} \tag{2.6}$$

The induced power loss is approximated by

$$P_i = \frac{1}{2} \sum_{i=1}^{M} \sum_{j=1}^{M} K_{ij} \Gamma_i \Gamma_j = \frac{1}{2} \boldsymbol{\Gamma}^T \mathbf{K} \, \boldsymbol{\Gamma} \tag{2.7}$$

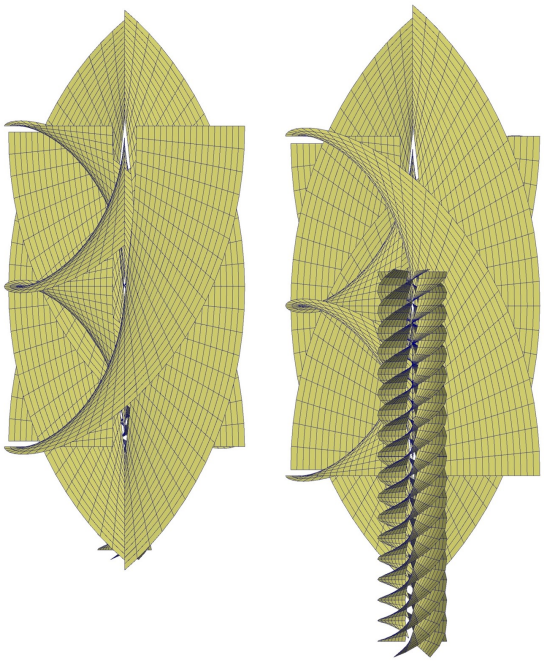

FIGURE 2.2: Left: top view of the vortex lattice grid of a coaxial rotor with propeller. Right: bottom view. Note that two periods of the wake are shown for clarity; only a single period is required in the analysis.

with

$$K_{ij} = -\frac{\rho}{T}\mathbf{w}_{ij} \cdot \mathbf{n}_i \, \Delta A_i \tag{2.8}$$

and the profile power loss is approximated by

$$P_v = \frac{\rho}{T} \sum_{i=1}^{M} \frac{u_i^2}{2} c_i c_{di} \Delta A_i \tag{2.9}$$

2.2 Optimal Rotor Performance

In the design of a rotor, one may select a fixed blade twist distribution $\theta_0(r)$ and implement some limited set of harmonic blade pitch control inputs. For such a configuration, the blade twist as a function of radius r and azimuth ψ can be described as

$$\theta(r, \psi) = \theta_0(r) + A_0 + \sum_{n=1}^{N} A_n \cos(n\psi) + \sum_{n=1}^{N} B_n \sin(n\psi) \tag{2.10}$$

where A_n and B_n are the Fourier coefficients of the blade pitch and N is the number of harmonics in the higher harmonic control system. A conventional helicopter, with collective and cyclic control corresponds to $N = 1$.

We denote the total vector of design variables and control inputs by $\boldsymbol{\theta}$. For a harmonic blade pitch control scheme as shown in Eq. (2.10), the vector $\boldsymbol{\theta}$ will be comprised of the Fourier coefficients of blade pitch A_0, A_n, and B_n, $\theta_0(r)$ at a discrete set of radii, and the chord distribution $c(r)$ at a discrete set of radii. Alternatively $\theta_0(r)$ and $c(r)$ can be represented by a summation of shape functions in the radial direction, in which case the coefficients of the shape functions would be members of $\boldsymbol{\theta}$. In this study, we represent the radial twist and chord as summations of Legendre polynomials.

To compute the forces, moments, and power resulting from a given rotor design, we must find the far field circulation in terms of the design variables and control inputs. Using our lightly loaded model, the induced wash is a linear function of the circulation. However, the resulting induced angles of attack on the rotor blade can be large, especially in and near the reverse flow region – large enough to require the use of a nonlinear lift curve – rendering the circulation a nonlinear function of the control inputs.

In this study, we relate the rotor design to the circulation using a nonlinear interative lifting-line method. We use a lifting-line approximation of the blade to compute the near field induced wash, which is then used, in combination with the geometric angle of attack due to the motion of the blade and the pitch angle of the blade at a given section, to calculate the effective angle of attack and the resulting lift and drag coefficients in an iterative process. We model the near field wake using a system of quadrilateral vortex elements consisting of both trailing and shed vorticity. The trailing vorticity is represented by vortex filaments parallel to the free stream flow u at the blade and is caused by changes in the bound circulation of the blade

in the radial direction, i.e., $\gamma_{\text{trailing}} = d\Gamma/dr$. The shed vorticity is represented by vortex segments perpendicular to the free stream flow u and represents changes in the bound circulation of the blade with time, or equivalently, with azimuthal position, i.e., $\gamma_{\text{shed}} = d\Gamma/d\psi$. For the work presented here, we use a uniform azimuthal spacing for the shed vortex filaments with the collocation point located on the bound vortex. As this azimuthal spacing is decreased and the grid is resolved, however, the nearest shed vortex filament will approach the collocation point, located on the lifting line, causing a weak logarithmic singularity in the computed near field induced wash. Consistent with the work of Miller [54, 55], we updated the near field wake model to place the first shed vortex one quarter chord behind the lifting line to avoid this singularity. This resulted in very small differences in the rotor design and computed performance, on the order of 1%, for several test cases.

2.2.1 Optimality Conditions for Rotor Design

In this section, we express the optimal design of a rotor/wing/propeller system with a finite number of design variables and control inputs as a variational statement. We seek to find the circulation distribution that minimizes the power loss subject to the constraints that the rotor generate a prescribed force $\mathbf{F}_{\text{R}}$, is trimmed in pitch and roll ($\mathbf{M}_{\text{R}} = 0$), and the circulation is realizable using our finite set of design variables and control inputs. Thus, we adjoin to the power these constraints using Lagrange multipliers to obtain the Lagrangian power

$$\Pi = \frac{1}{2}\boldsymbol{\Gamma}^T\mathbf{K}\boldsymbol{\Gamma} + P_{\text{v}} + \boldsymbol{\lambda}_F^T \cdot (\mathbf{B}\boldsymbol{\Gamma} - \mathbf{F}_{\text{R}}) + \boldsymbol{\lambda}_M^T \cdot (\mathbf{D}\boldsymbol{\Gamma} - \mathbf{M}_{\text{R}}) + \boldsymbol{\lambda}_R^T \cdot \mathbf{R}(\boldsymbol{\Gamma}, \boldsymbol{\theta}) \tag{2.11}$$

where the nonlinear lifting line equations are given by the vector function

$$\mathbf{R}(\boldsymbol{\Gamma}, \boldsymbol{\theta}) = 0 \tag{2.12}$$

In the present analysis, we use a nonlinear lifting line analysis, but $\mathbf{R}$ could also describe some other numerical method for computing the circulation in terms of the

design variables, e.g., a panel method.

Taking the variation of Eq. (2.11) and setting the result to zero for arbitrary variations in the circulation, control inputs, and Lagrange multipliers gives a set of linear equations for the circulation, controls, and Lagrange multipliers, together with Eq. (2.12). The linear equations are given by

$$\begin{bmatrix} \frac{1}{2}(\mathbf{K}+\mathbf{K}^T) & \mathbf{B}^T & \mathbf{D}^T & \mathbf{R}_\Gamma^T \\ \mathbf{0} & \mathbf{0} & \mathbf{0} & \mathbf{R}_\theta^T \\ \mathbf{B} & \mathbf{0} & \mathbf{0} & \mathbf{0} \\ \mathbf{D} & \mathbf{0} & \mathbf{0} & \mathbf{0} \end{bmatrix} \begin{Bmatrix} \boldsymbol{\Gamma} \\ \boldsymbol{\lambda}_F \\ \boldsymbol{\lambda}_M \\ \boldsymbol{\lambda}_R \end{Bmatrix} = \begin{Bmatrix} -\mathbf{P}_{V\Gamma} \\ -\mathbf{P}_{V\theta} \\ \mathbf{F}_R \\ \mathbf{M}_R \end{Bmatrix} \tag{2.13}$$

where $\mathbf{R}_\Gamma$ and $\mathbf{R}_\theta$ are the Jacobians of $\mathbf{R}$ with respect to $\boldsymbol{\Gamma}$ and $\boldsymbol{\theta}$ respectively, and $\mathbf{P}_\Gamma$ and $\mathbf{P}_{V\theta}$ are the gradients of P_v with respect to $\boldsymbol{\Gamma}$ and $\boldsymbol{\theta}$ respectively.

The nonlinear relationship between the circulation and the rotor design variables and control inputs complicates the solution process a bit. Starting with some initial guess at the design variables, we can calculate the circulation that satisfies Eq. (5.8). We will refer to this initial circulation as $\boldsymbol{\Gamma}^k$ (with $k = 0$). We then estimate the circulation due to a change in the control variables to first order as

$$\boldsymbol{\Gamma}^{k+1} = \boldsymbol{\Gamma}^k + \mathbf{A}\boldsymbol{\Delta\theta} \tag{2.14}$$

where the matrix $\mathbf{A}$ is defined as

$$\mathbf{A} = \frac{\partial \boldsymbol{\Gamma}}{\partial \boldsymbol{\theta}^T} \tag{2.15}$$

i.e., $\mathbf{A}$ is the first-order approximation of the change in circulation due to a change in the design variables.

Similarly for the viscous power loss term, we have

$$P_v \approx P_{v0} + \mathbf{K}_v^T \boldsymbol{\Delta\theta} \tag{2.16}$$

where the vector $\mathbf{K}_v$ is defined as

$$\mathbf{K}_v = \frac{\partial P_v}{\partial \boldsymbol{\theta}^T} \tag{2.17}$$

i.e., $\mathbf{K}_v$ relates a change in design variables to the first-order change in viscous power loss. The entries of the $\mathbf{A}$ matrix and the $\mathbf{K}_v$ vector are determined by Taylor expanding expressions for the circulation and viscous power loss in terms of the design variables and retaining first-order terms, giving closed form approximations for the circulation and viscous power loss derivatives. This derivation and the exact expressions for $\mathbf{A}$ and $\mathbf{K}_v$ are given in Appendix A. Substituting these first-order expansions into the Lagrangian power from Eq. (2.11) gives

$$\Pi = \frac{1}{2}(\boldsymbol{\Gamma} + \mathbf{A}\boldsymbol{\Delta\theta})^T\mathbf{K}(\boldsymbol{\Gamma} + \mathbf{A}\boldsymbol{\Delta\theta}) + P_{v0} + \mathbf{K}_v^T\boldsymbol{\Delta\theta} + \boldsymbol{\lambda}_F{}^T(\mathbf{B}(\boldsymbol{\Gamma} + \mathbf{A}\boldsymbol{\Delta\theta}) - \mathbf{F_R}) + \boldsymbol{\lambda}_\mathbf{M}{}^\mathbf{T}(\mathbf{D}(\boldsymbol{\Gamma} + \mathbf{A}\boldsymbol{\Delta\theta}) - \mathbf{M_R}) \quad (2.18)$$

Taking the variation of Eq. (2.18) and setting the result to zero for arbitrary variations in the change in control inputs $\boldsymbol{\Delta\theta}$ and Lagrange multipliers gives the linear equations

$$\begin{bmatrix} \frac{1}{2}\mathbf{A}^T(\mathbf{K}+\mathbf{K}^T)\mathbf{A} & \mathbf{A}^T\mathbf{B}^T & \mathbf{A}^T\mathbf{D}^T \\ \mathbf{BA} & \mathbf{0} & \mathbf{0} \\ \mathbf{DA} & \mathbf{0} & \mathbf{0} \end{bmatrix} \begin{Bmatrix} \boldsymbol{\Delta\theta} \\ \lambda_\mathbf{F} \\ \lambda_\mathbf{M} \end{Bmatrix} = \begin{Bmatrix} -\mathbf{A}^T\mathbf{K}\boldsymbol{\Gamma} - \mathbf{K}_v \\ \mathbf{F}_R - \mathbf{B}\boldsymbol{\Gamma} \\ \mathbf{M}_R - \mathbf{D}\boldsymbol{\Gamma} \end{Bmatrix} \quad (2.19)$$

At each iteration, this system of equations is solved, satisfying the equality constraints and minimizing the total power to first order. The vector of design variables is then updated,

$$\boldsymbol{\theta}^{k+1} = \boldsymbol{\theta}^k + \boldsymbol{\Delta\theta} \quad (2.20)$$

and the linearized approximation of circulation is computed by Eq. (2.14). Of course, since $\boldsymbol{\Gamma}^{k+1}$ is a first-order approximation, the residual $\mathbf{R}(\boldsymbol{\Gamma}^{k+1}, \boldsymbol{\theta}^{k+1})$ will be non-zero. It is necessary to calculate the accurate, nonlinear circulation at $\boldsymbol{\theta}^{k+1}$; in other words, to determine the $\boldsymbol{\Gamma}$ that makes $\mathbf{R}(\boldsymbol{\Gamma}, \boldsymbol{\theta}^{k+1}) = 0$. This updated, corrected value of $\boldsymbol{\Gamma}$ is then used in the following iteration. This process is repeated until convergence.

In addition to the equality constraints on forces and moments, we also implement inequality constraints on the chord of each lifting component using Mathematical

Programming via Augmented Lagrangians, in order to prevent the optimization from taking advantage of negative or infinitesimal chords. We also implement an equality constraint on the thrust-weighted solidity of the rotor. Because we are performing a single point optimization at very high flight speeds, and because of the high dynamic pressures present on the advancing side of each rotor and the natural roll trim of the coaxial system, the resulting optimal chord is often quite small – too small for the helicopter to hover. Constraining the thrust weighted solidity ensures that the design is capable of hover and low speed flight. However, because the thrust weighted solidity heavily weights solidity at the blade tip, and because the circulation goes to zero at the tip regardless of the chord, we constrain instead a modified thrust weighted solidity defined by

$$\sigma_{\text{TWM}} \equiv \frac{3}{R^3} \int_{R_{CO}}^{R} r^2 \sigma(r) \cdot \{1 - \exp[-(1 - r/R)/\epsilon]\} \, \mathrm{d}r \tag{2.21}$$

where ϵ is a constant taken to be 0.10 and R_{CO} is the root cutout of the rotor. The effect of the term in braces in the integrand is to remove the influence of the solidity of the tip. The shape of the tip is then more naturally selected to minimize power.

2.3 Results

We consider first a vehicle modeled roughly after the Sikorsky X2 Technology Demonstrator (TD), with two coaxial counter-rotating four-bladed rotors and a six-bladed pusher propeller to provide an auxiliary propulsive force. We analyze rotors similar in design intent to the X2 rotor system in high speed cruise as described by Bagai [12]. The parameters for the coaxial rotor system are listed in Table 2.1. The blade geometries of the upper and lower rotors are constrained to be equal, although each rotor has independent root pitch inputs. The propeller is roughly modeled after the X2 TD as well, with an RPM that is six times that of the rotors' and a radius

Table 2.1: Coaxial Rotor Full Vehicle Parameters.

Parameter	Value
Advance Ratio, μ	0.85
Relative tip Mach number	0.90
Coefficient of lift, C_L	0.02324
Thrust weighted solidity, σ_{TW}	0.1441
C_L/σ_{TW}	0.1613
Root cutout	10 percent of rotor radius
Vertical rotor separation	20 percent of rotor radius

equal to 25 percent of the rotor radius. Unlike the X2 TD, however, both the rotors and propeller use a NACA 0012 airfoil from root to tip.

To analyze a single advance ratio and shaft angle, we use a lattice of vortex rings containing 18 ring elements in the spanwise direction and 15 elements in the azimuthal direction for each rotor blade. Because of the 4/rev temporal periodicity of the problem, only one-quarter of a revolution of the wake is needed to achieve spatial periodicity of the wake. The spatially periodic lattice is replicated and extended 40 periods (10 complete turns of the rotor) downstream for the near field analysis, and 40 periods upstream and 40 periods downstream for the far wake induced power analysis. The propeller is modeled using 8 elements in the spanwise direction and 18 elements in the azimuthal direction for each full turn of the propeller. Because of its higher rotation rate, one and one-half turns of the propeller are modeled for each quarter turn of the wake.

2.3.1 Effect of Propulsive Force on Power

First, we will vary the propulsive force required by the vehicle in straight and level flight, which is equivalent to changing the value of the vehicle's fuselage drag. This allows us to study the effect that propulsive force requirements have on the optimal shaft angle and on optimal rotor design. We examine two cases for comparison:

a high propulsive force case, corresponding to a total propulsive force coefficient of $C_{\mathrm{Fx}} = F_{\mathrm{x}}/\rho A\Omega^2 R^2 = 0.0058$, and a low propulsive force case corresponding to $C_{\mathrm{Fx}} = 0.0031$. The cases analyzed here each use conventional $N = 1$ control.

For each case, we evaluate the performance and rotor design over a range of rotor shaft angles. All rotor and propeller design variables are optimized at each individual shaft angle. Thus, each data point represents a unique rotor design that provides the best possible performance at that flight condition. Note that only the rotor system is operating at the given shaft angle. Unless otherwise noted, the propeller axis is aligned with the direction of flight.

2.3.2 Effect of Propulsive Force on Optimal Shaft Angle.

Figure 2.3 shows the vehicle total power loss (i.e., total power minus useful thrust power) for the high and low propulsive force cases across a range of shaft angles, normalized by the square of the coefficient of lift of the vehicle. Note that the total power loss referenced here is the same total power loss defined by Ormiston in Reference [56] and used in previous papers [1, 40], and represents the net power loss of the system, that is, the sum of the induced and profile losses of the rotor and propeller. The power loss is divided into two components: the propeller power loss and the rotor power loss. The total power loss of the vehicle is the sum of these two components. A negative shaft angle indicates that the rotor system is tipped forward into the flow, providing a positive propulsive force in the flight direction. Though not shown in the figure, the normalized useful power (thrust power coefficient divided by the coefficient of lift squared) $C_{\mathrm{Puseful}}/C_{\mathrm{L}}^2$ is 9.13 for the high propulsive force case and 4.88 for the low propulsive force case. Thus, the power loss is a significant fraction of the total power.

As expected, the high propulsive force case has a higher overall power loss than the low propulsive force case across all shaft angles. The two cases, however, have

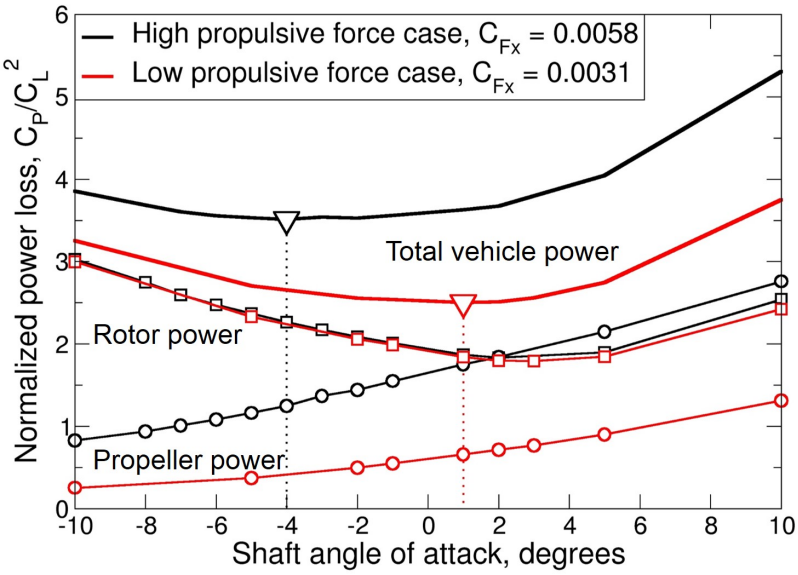

FIGURE 2.3: Power loss of a coaxial rotor with pusher propeller with varying levels of propulsive force.

significantly different optimal shaft angles. The low propulsive force case has a minimum total power at a shaft angle of $\alpha_{\text{shaft}} = 1°$, compared to $\alpha_{\text{shaft}} = -4°$ for the high propulsive force case.

To investigate the reason for this difference in optimal shaft angle, we examine a slightly simplified form of the variational statement. We seek to minimize the total power subject to the constraint that the required propulsive force (thrust) and the required lift are generated by the rotor/propeller system. Thus we form the Lagrangian Π given by

$$\Pi = P_{\text{rotor}} + P_{\text{prop}} - \lambda_T \left(T_{\text{rotor}} + T_{\text{prop}} - T_{\text{R}}\right) - \lambda_L \left(L_{\text{rotor}} + L_{\text{prop}} - L_{\text{R}}\right) \qquad (2.22)$$

where P is the power, T is the thrust and L is the lift of either the rotor or propeller as denoted by subscripts. T_{R} and L_{R} are the required thrust and lift of the vehicle, respectively. Taking the variation of Eq. (2.22), making the assumption that the power and thrust of each component is independent of the other component, and

setting the result to zero gives

$$\begin{aligned}\delta\Pi = 0 = &\left(\frac{\partial P_{\text{rotor}}}{\partial T_{\text{rotor}}} - \lambda_T\right)\delta T_{\text{rotor}} - \left(\frac{\partial P_{\text{prop}}}{\partial T_{\text{prop}}} - \lambda_T\right)\delta T_{\text{prop}} \\ &- \left(T_{\text{rotor}} + T_{\text{prop}} - T_{\text{R}}\right)\delta\lambda_T - \left(L_{\text{rotor}} + L_{\text{prop}} - L_{\text{R}}\right)\delta\lambda_L\end{aligned} \tag{2.23}$$

Equation 2.23 must be true for arbitrary variations in the rotor thrust, propeller thrust, and the Lagrange multipliers. Therefore, each of the four terms in parentheses must equal zero independently. For the first two terms in parentheses to satisfy this condition, we must have

$$\lambda_T = \frac{\partial P_{\text{rotor}}}{\partial T_{\text{rotor}}} = \frac{\partial P_{\text{prop}}}{\partial T_{\text{prop}}} \tag{2.24}$$

Equation (2.24) states that the minimum total vehicle power occurs when the change in power due to an incremental change in thrust is equal between the rotor and the propeller. This optimality condition was also derived graphically by Rand and Khromov [25].

Figure 2.4 shows the power loss as a function of the coefficient of propulsive force for the rotor and propeller for both the high and low propulsive force cases. The optimality condition, Eq. (2.24), is satisfied at the shaft angle where the rotor and propeller power curves have the same slope. Note that the rotor power curves for the high and low propulsive force cases are very similar; the power depends primarily on shaft angle and is only very weakly dependent on the propulsive force. The propeller power curves for the two cases are virtually identical; the propeller power is almost entirely dependent on the thrust it produces. For a given combined coefficient of thrust, the system will be optimal when the slope of the the power curves are equal. We see that for the low total propulsive force case, it is more efficient to tilt the rotor aft so that the rotor generates almost no thrust. For the higher total propulsive force case, the optimum occurs when both the rotor and propeller generate significant thrust. In any event, we see that in both cases, the largest share of thrust is generated

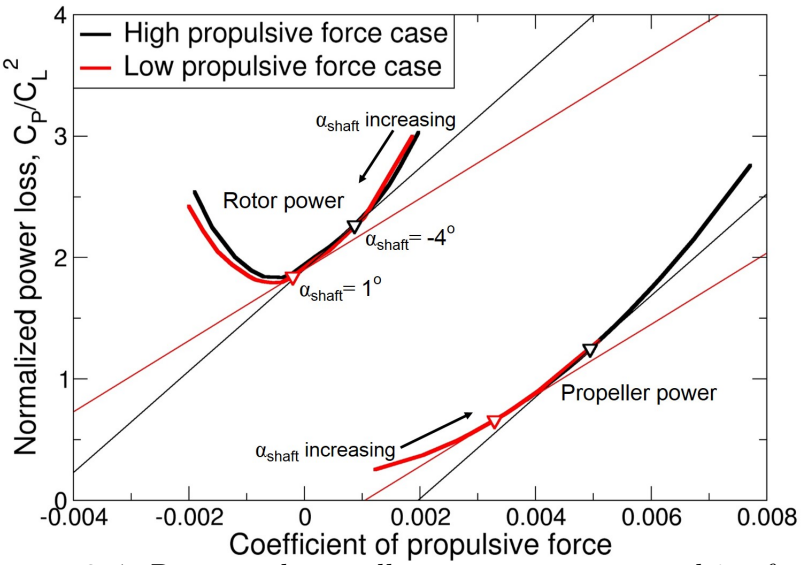

FIGURE 2.4: Rotor and propeller power versus propulsive force.

by the propeller.

Figure 2.3 also reinforces an important conclusion reached by Rand and Khromov [25]. At high speed, the minimum total vehicle power is not necessarily achieved by operating at the minimum rotor power, which occurs in this case at $\alpha_{\text{shaft}} = 3.5°$, or by placing the rotor system in an autorotative state, which occurs at roughly $\alpha_{\text{shaft}} = 7.5°$. Rather, the minimum total power depends on the design and efficiency of both the propeller and rotor.

2.3.3 Effect of Propulsive Force on Optimal Rotor Design.

Each of the above design points represents a rotor and propeller optimized for one specific shaft angle. For each value of total propulsive force there is an optimal shaft angle and corresponding rotor design. In Fig. 2.5, we illustrate how optimal rotor design varies with total propulsive force. Figure 2.5 shows the optimal radial twist distribution and optimal planform for the high and low propulsive force cases, corresponding to an optimum shaft angle of $\alpha_{\text{shaft}} = -4°$ and $1°$, respectively. Note that the optimal planform and twist distributions for these two cases differ significantly,

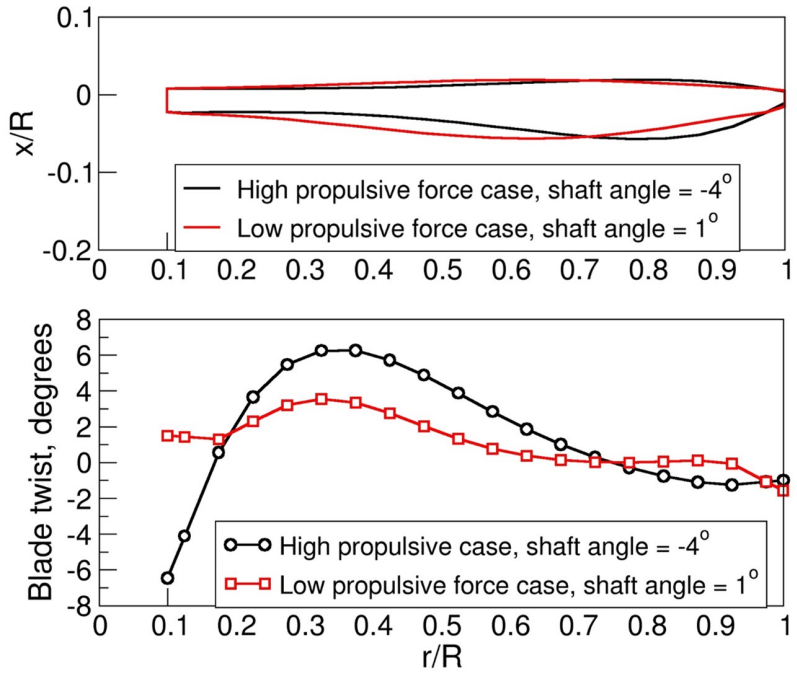

FIGURE 2.5: Optimal rotor blade planform and twist at $\alpha_{\text{shaft}} = -4°$ and $\alpha_{\text{shaft}} = 1°$.

showing that shaft angle and rotor geometry of an optimized vehicle are strongly influenced by the flight conditions (at least for a single point design).

2.3.4 Higher Harmonic Control

As demonstrated by Hall and Giovanetti [40], higher harmonic control is effective in reducing total power loss in an isolated coaxial rotor system, particularly at high advance ratios. Here we consider the effect of higher harmonic control on power and rotor design for a complete compound vehicle, including a propulsive force constraint.

Figure 2.6 shows the total vehicle power loss for the high propulsive force case using $N = 1$ control (conventional cyclic control), and $N = 3$ control (higher harmonic control). Using $N = 3$ control reduces the rotor power loss significantly, particularly at negative shaft angles, and results in an optimal shaft angle of $\alpha_{\text{shaft}} = -9°$. This decrease in optimal shaft angle allows the rotors to provide a much larger fraction of the vehicle's overall propulsive force - approximately 33 percent, compared to 15 per-

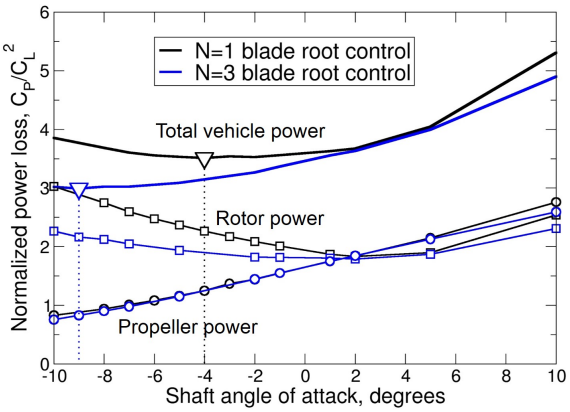

FIGURE 2.6: Power loss of a coaxial rotor with pusher propeller using $N = 1$ and $N = 3$ blade root control divided into propeller and rotor components.

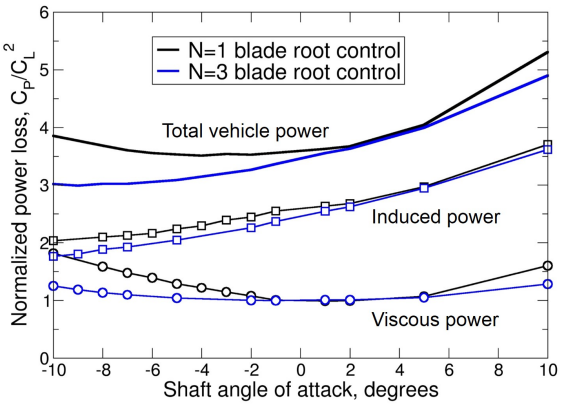

FIGURE 2.7: Power loss of a coaxial rotor with pusher propeller using $N = 1$ and $N = 3$ blade root control divided into induced and viscous components .

cent for the $N = 1$ control case at its optimal shaft angle of $\alpha_{\text{shaft}} = -4°$. Overall, $N = 3$ control reduces total vehicle power loss by 15 percent over $N = 1$ control at each case's optimal shaft angle. While not shown in Fig. 2.6, $N = 2$ control results in an optimal shaft angle of $\alpha_{\text{shaft}} = -7°$ and reduces power loss by 7.5 percent compared to $N = 1$ control. Harmonic control above $N = 3$ produces little additional power reduction.

Figure 2.7 shows the induced and viscous contributions to the total power loss for the $N = 1$ and $N = 3$ control cases. Higher harmonic control results in a lower total power loss by reducing both the induced and viscous components of power. Note that for shaft angles ranging from $\alpha_{\text{shaft}} = 1°$ to $\alpha_{\text{shaft}} = 5°$, higher harmonic control provides almost no advantage over conventional control, although these shaft angles are far from optimal in this configuration.

Figure 2.8 shows the optimal circulation distribution for the $N = 1$ and $N = 3$ cases. Also plotted is the circulation distribution for the optimal rubber rotor solution, which represents the absolute minimum power solution without regard to the rotor geometry or control inputs required to achieve this circulation. The $N = 1$

case generates a large positive circulation on the advancing side of each rotor, in addition to a moderate positive circulation on the retreating side of each rotor. The $N = 3$ case has multiple regions of concentrated circulation on the advancing side – one at $\psi = 90°$, similar to the $N = 1$ case, but also smaller areas of concentrated circulation at $\psi = 0°$ and $\psi = 180°$. Additionally, the $N = 3$ case does not have the moderate positive circulation on the retreating side seen in the $N = 1$ case, instead having a region of low circulation that closely resembles the rubber rotor result.

Both cases have regions of high circulation, and therefore high lift, in a region just past the blade midspan on the advancing side. Thus, each rotor carries a large rolling moment and a lateral lift offset. The moment carried by each rotor is transmitted through the hub, resulting in a net vehicle rolling moment of zero.

Figure 2.9 shows the blade pitch inputs as a function of azimuth for the two cases. The $N = 1$ azimuthal pitch input varies between 6° and 10°, while the $N = 3$ pitch input has a dramatic decrease in pitch around $\psi = 270°$, corresponding to the region of near-zero circulation on the retreating side of each rotor. This decrease in pitch reduces circulation on the retreating side of the rotor, making the circulation distribution closer to the rubber rotor optimum, thereby reducing power.

Figure 2.10 shows the optimal radial twist and planform distribution for the $N = 1$ and $N = 3$ cases. Figure 2.11 shows an overhead view of the coaxial rotor system using the $N = 3$ optimal blade planform. The $N = 3$ blade has a wider chord near midspan, while the $N = 1$ blade has a wider chord in the outboard region. The radial twist distributions are fairly similar between the two cases, with the exception of the inner 20 percent of the blade, where the $N = 1$ blade has a large positive twist gradient.

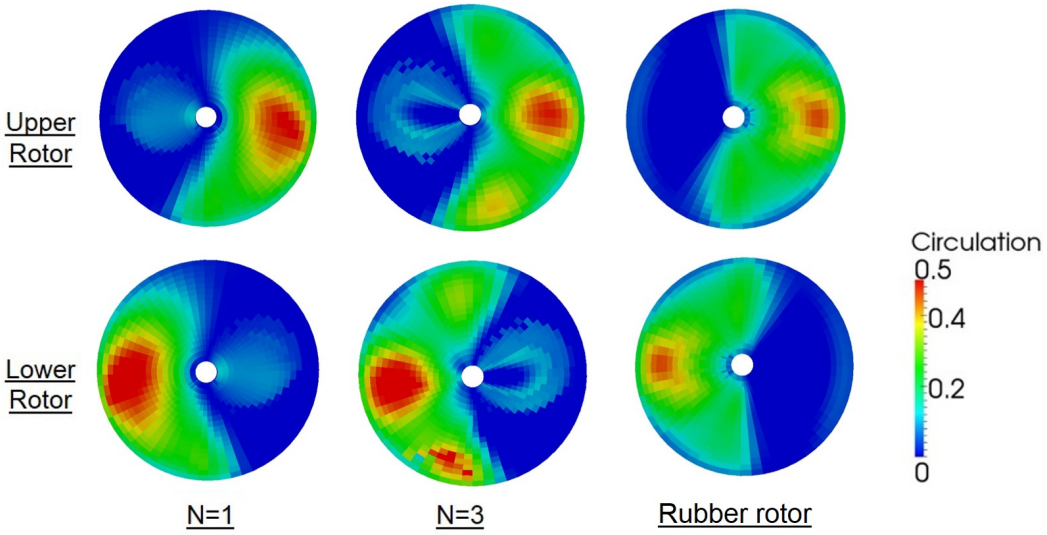

FIGURE 2.8: Optimal normalized circulation distribution for $N = 1$ control, $N = 3$ control, and the rubber rotor solution. The upper rotor is spinning counter-clockwise, and the lower rotor is spinning clockwise.

2.3.5 Effect of Lift Offset

Lift offset is defined as the lateral distance from the centerline of the aircraft to the center of lift on a rotor. In nondimensional form, the lift offset is defined as $\Delta M_x/LR$, where ΔM_x is the difference in rolling moment between the two rotors, R is rotor radius, and L is total lift. The $N = 1$ and $N = 3$ minimum power solutions from the previous section have nondimensional lift offsets of 0.54 and 0.49, respectively, indicating that the optimal solution offloads lift on the retreating side and generates the majority of the lift on the advancing side. In the design of an actual rotor, it may be necessary to constrain the rotor's lift offset to limit blade root and shaft bending moments for structural considerations. For example, according to Bagai [12], in the design of the X2 technology demonstrator the lift offset was limited to 0.3 for structural and hub weight considerations. In this section, we constrain the lift offset to a maximum value of 0.3 to determine the effect that reduced lift offset has on rotor performance and design.

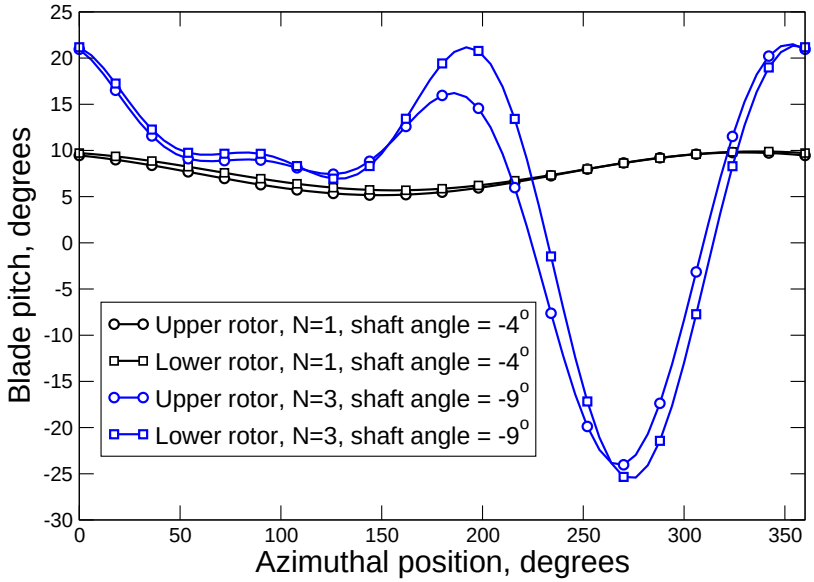

FIGURE 2.9: Azimuthal pitch inputs using $N = 1$ and $N = 3$ blade root control.

Figure 2.12 shows the normalized total power loss for $N = 1$ and $N = 3$ blade root harmonic control with the rotor system's lift offset constrained to a maximum value of 0.3. Also shown is is the $N = 1$ total power loss for the case unconstrained in lift offset from Figure 2.6. We observe that for both levels of harmonic control, the lift offset constrained solution has significantly higher total power loss than the unconstrained result. At the optimal shaft angle for each case, the $N = 1$ lift offset constrained case has a 40 percent higher total power loss than the unconstrained result, while the $N = 3$ lift offset constrained case has a 49 percent higher total power loss than the unconstrained result. This increase in power is due almost entirely to an increase in the rotor system's power. The propeller power, as expected, is essentially unaffected by the changes in rotor design.

The decreased efficiency of the rotor system with the lift offset constraint shifts the optimal shaft angle to be more positive, i.e., to tilt the rotor system aft. The optimal shaft angle for the $N = 1$ case has shifted from $\alpha_{\text{shaft}} = -4°$ with lift offset unconstrained to $\alpha_{\text{shaft}} = 6°$ with the lift offset constrained. For the $N = 3$ case, the optimal shaft angle has shifted from $\alpha_{\text{shaft}} = -9°$ unconstrained to $\alpha_{\text{shaft}} = -4°$ with

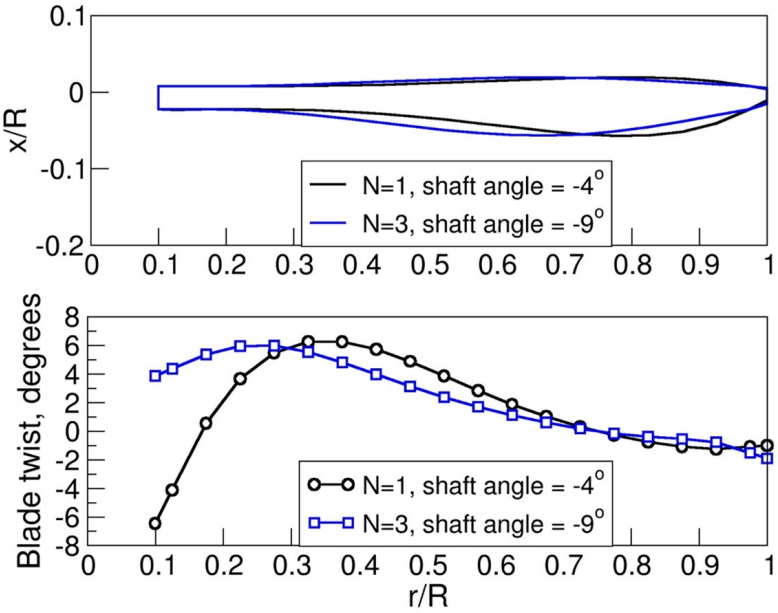

FIGURE 2.10: Optimal rotor blade planform and twist for $N = 1$ and $N = 3$ blade root control.

the lift offset constrained.

The amount of power reduction achieved with higher harmonic control and the lift offset constrained to 0.3 is highly dependent on the shaft angle. At negative shaft angles, the $N = 1$ rotor has very high power losses, and use of $N = 3$ control reduces these power losses significantly. For example, at $\alpha_{\text{shaft}} = -4°$, the $N = 3$ case reduces rotor system power loss by 43 percent, leading to a 34 percent reduction in total vehicle power loss compared to the $N = 1$ case. However, as the shaft angle increases, the rotor system is tilted aft and enters an increasingly auto-rotative state in which the benefits of higher harmonic control decrease. In fact, at $\alpha_{\text{shaft}} = 8°$, $N = 3$ control reduces total vehicle power loss by less than 1 percent.

At the optimal shaft angle for each lift offset constrained case, $N = 3$ control reduces total power loss by 11 percent compared to $N = 1$ control. Because the two cases have minimum powers at such disparate shaft angles, the optimal blade designs for the two cases, shown in Fig. 2.13, differ significantly. The $N = 1$ planform locates

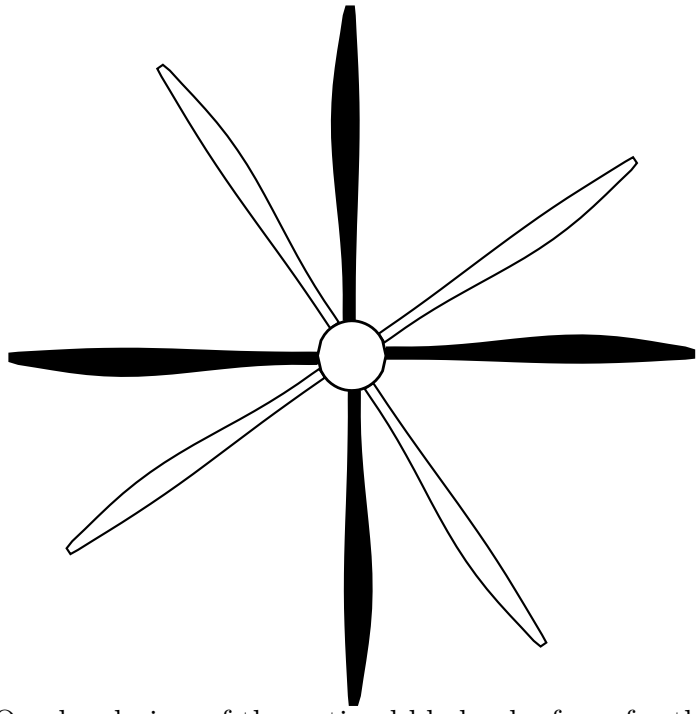

FIGURE 2.11: Overhead view of the optimal blade planform for the $N = 3$ design.

much of the blade area on the inboard 50 percent of the blade, while for the $N = 3$ case, the chord distribution is nearly centered about the midspan point.

Finally, we investigate how higher harmonic control achieves such large power reductions at negative shaft angles. Figure 2.14 shows the optimal normalized lift distribution for $N = 1$ and $N = 3$ control for the cases with the lift offset constrained to 0.3. Also shown are the rubber rotor results with and without the offset constraint, along with the unconstrained $N = 1$ case, all at a shaft angle of $\alpha_{\text{shaft}} = -4°$. We see that the constrained higher harmonic control ($N = 3$) case comes much closer to reproducing the ideal constrained rubber rotor solution than does the conventional control ($N = 1$) case.

Figure 2.15 shows the optimal azimuthal pitch inputs for the $N = 1$ and $N = 3$ constrained lift offset cases, as well as the $N = 1$ unconstrained case, again at a shaft angle of $\alpha_{\text{shaft}} = -4°$. Note that for the unconstrained case, the cyclic variation in pitch is modest, about 4°. For the constrained conventional control, however, the

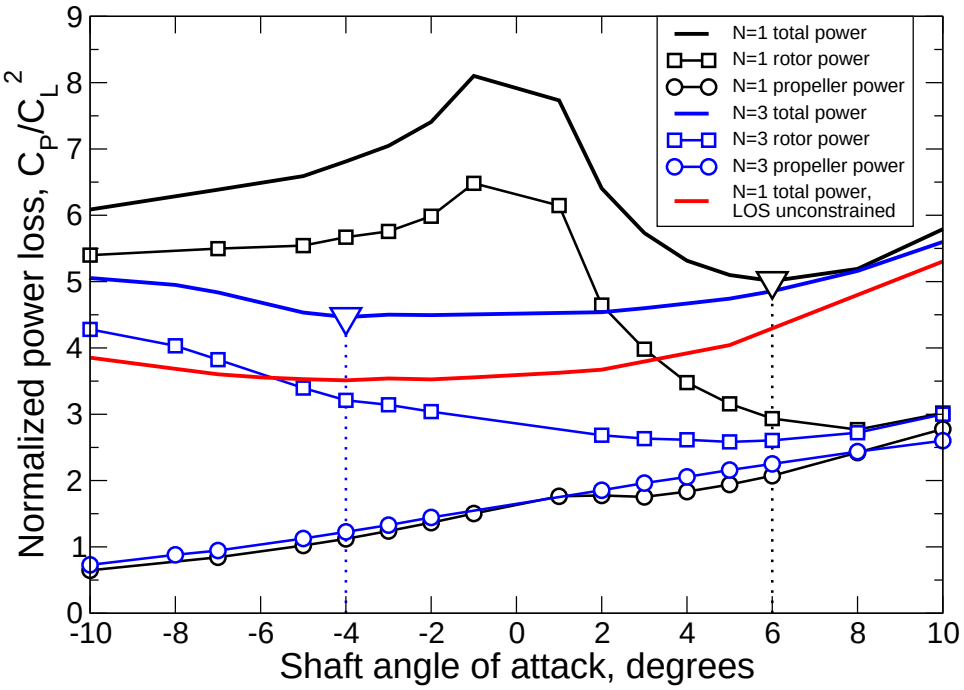

FIGURE 2.12: Normalized power loss from the baseline compound constrained to a lateral lift offset of 0.3 using $N = 1$ and $N = 3$ control. Also included is the total power loss from the $N = 1$ unconstrained LOS rotor.

cyclic control is quite large, varying more than 40° (of course the blade planform and twist distributions are also different). For the higher harmonic control case, the pitch control is similar to the conventional cyclic control case, except for the very large negative pitch on the retreating side of the rotor. Together with the blade geometry, this higher harmonic control drives the circulation – and hence the force distribution – closer to the constrained rubber rotor optimum.

These results show that constraining the maximum lift offset greatly increases the rotor and vehicle power losses and has a large influence on the optimal shaft angle and rotor design. Higher harmonic control significantly reduces power loss, and as we have seen, this drives the optimal shaft angle to be more negative, i.e., the rotor generates a more significant share of the propulsive force. Because lift offset constrained rotors using conventional rotor control have higher losses, the optimal

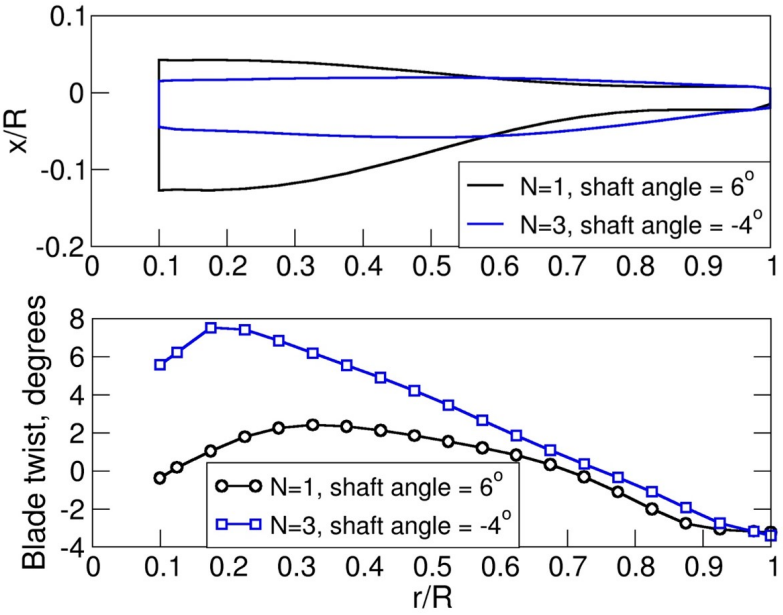

FIGURE 2.13: Optimal rotor blade planform and twist for $N = 1$ and $N = 3$ blade root control with lateral lift offset constrained to be 0.3.

shaft angles tend to be positive (towards autorotation) with the propeller producing the majority of the propulsive force. As a result of the difference in optimal shaft angles, the optimal conventional ($N = 1$) and higher harmonic ($N = 3$) rotor designs differ quite substantially.

2.3.6 Use of a Wing to Supplement Lift

We now add a lifting wing to our vehicle model, to determine its effect on total power requirements. The wing has a span equal to one rotor radius and is located one half of a rotor radius below the lower rotor of the coaxial system. To ensure the optimization does not make use of excessively small chord values, the chord is constrained to be no smaller than 8 percent of the wing span. The optimization finds the fixed radial twist and chord distributions of the wing. Note also that in this analysis, the power loss associated with the wing must be added to the fuselage drag to compute the total propulsive force required for the vehicle. The wing wake

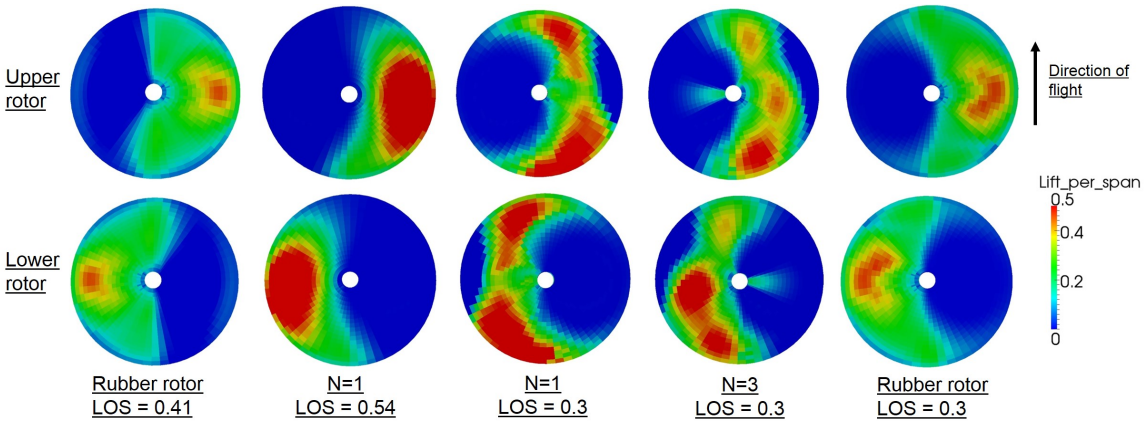

FIGURE 2.14: Optimal normalized lift distribution for $N = 1$ and $N = 3$ control with lateral lift offset constrained to a value of 0.3.

is modeled using 20 vortex-lattice ring elements in the spanwise direction and 15 elements in the flight direction per quarter period of revolution of the rotors.

Figure 2.16 shows the total power for the winged coaxial configuration over a range of shaft angles, along with the baseline configuration that does not include a wing. The use of a wing reduces the total vehicle power loss by less than 1 percent, and slightly increases the optimal shaft angle to $\alpha_{\text{shaft}} = -3°$. While the presence of a wing decreases the rotor system's power by supplementing its lift, the additional wing power is almost equal to the power saved, resulting in a very similar but very slightly lower total vehicle power. This result is due to the high efficiency of the coaxial rotor, and is in contrast to what a similar analysis shows for a single rotor with a wing (e.g., the Cheyenne helicopter), in which the use of a wing significantly reduces power at high advance ratios [1]. Though not plotted, the optimal wing lift share varies nearly linearly between 22 percent of the vehicle lift at a shaft angle of $\alpha_{\text{shaft}} = -10°$ to a value of approximately 43 percent at a shaft angle of $\alpha_{\text{shaft}} = 10°$. As the rotor tilts aft towards auto-rotation, the wing provides an increasing proportion of the vehicle's lift.

Figure 2.17 shows the wing twist distribution at the optimal shaft angle of $\alpha_{\text{shaft}} =$

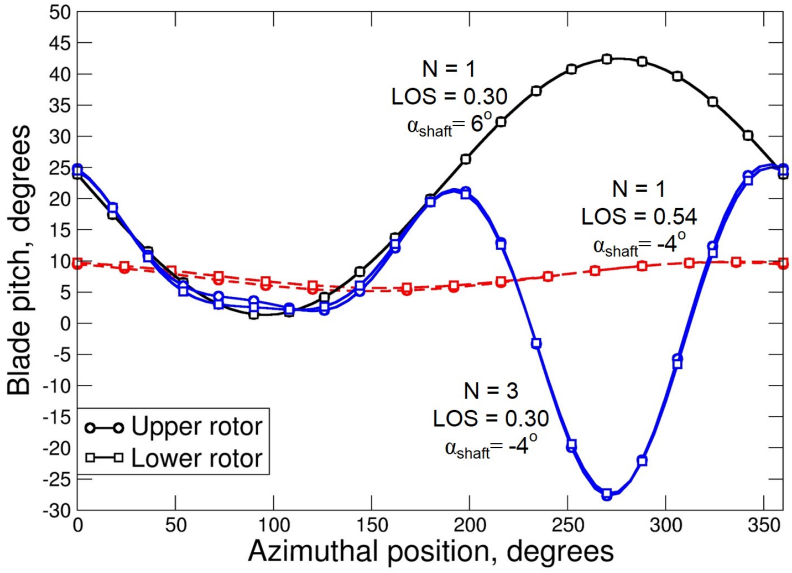

FIGURE 2.15: Azimuthal pitch inputs for the baseline compound constrained to a lateral lift offset of 0.3 using $N = 1$ and $N = 3$ control and the baseline compound unconstrained in lateral lift offset using $N = 1$ control.

$-3°$. While not plotted, the optimum wing chord is equal to the minimum chord constraint at all radial stations, resulting in a rectangular planform. Because the wing is so lightly loaded in all cases, it is advantageous to minimize the wing's surface area and viscous drag. Also note that the twist distribution is approximately symmetric, resulting in nearly zero rolling moment on the wing. For a similar analysis using a single rotor in combination with a wing [41], the optimal wing is asymmetric, with increased values of twist and chord on the retreating side of the rotor to generate more lift in this region and balance the rolling moment of the rotor. Because the coaxial rotor system is naturally in roll trim, the wing no longer has the primary function of providing roll trim. Rather, the wing simply supplements the rotor's lift, and does not provide the dramatic power reductions present when used within a single rotor Cheyenne-style compound.

For the case considered here, the coaxial rotors are unconstrained in lift offset. If a wing were used in a case that also included a lift offset constraint, we might expect

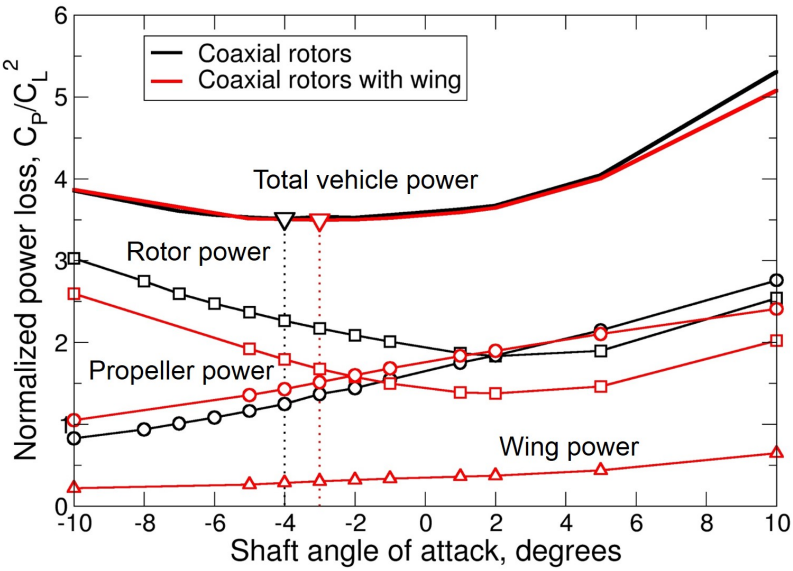

FIGURE 2.16: Power loss of a coaxial rotor with pusher propeller compared to a coaxial rotor with pusher propeller and wing.

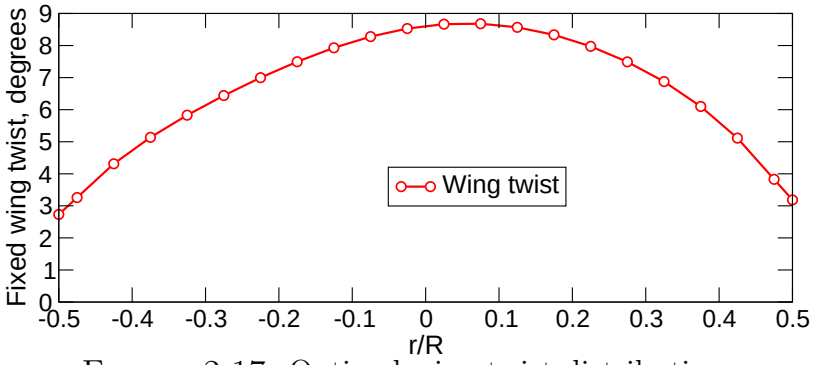

FIGURE 2.17: Optimal wing twist distribution.

higher power savings, as the rotors are significantly less efficient, leading to potential power reductions by using the wing to offload the rotors.

2.3.7 Using the Propeller to Supplement Lift

Another design feature available to compound helicopters is the ability to use the propeller's thrust to supplement the lift of the vehicle. A similar feature is sometimes used on the tail rotors of conventional helicopters, which can be inclined slightly downwards to provide additional lift. There are two ways to allow the propeller to

provide lift: inclining the propeller downwards by some angle, allowing a component of its thrust to act in the vertical direction, or providing the propeller $N = 1$ cyclic control, allowing it to preferentially generate more or less force on the upstroke or downstroke producing a small vertical force.

Figure 2.18 shows the total power versus rotor shaft angle for three cases: a coaxial configuration with the propeller tilted 5° downward from horizontal, a coaxial configuration using $N = 1$ pitch control on the propeller, and the baseline coaxial configuration using $N = 0$ pitch control on the propeller and the propeller aligned with the free stream flow. A tilt angle of 5° is plotted because it provides the largest power reduction of the various tilt angles considered. Although all three cases have very similar overall power loss, the 5° tilted propeller reduces vehicle power loss by 1.5 percent compared to the baseline, while providing approximately 6 percent of the total vehicle lift. The $N = 1$ propeller reduces vehicle power loss by approximately 1 percent and provides approximately 3 percent of the total vehicle lift. In both cases, the propeller offloads the rotor system, decreasing rotor power while increasing propeller power by a smaller amount.

2.4 Conclusions

In this chapter, we have presented results for the optimal aerodynamic design and performance of the rotors and propeller (and optionally a lifting wing) of a compound helicopter using counter-rotating coaxial rotors. We analyzed each configuration at an advance ratio of $\mu = 0.85$ over a range of rotor shaft angles. At each shaft angle, all design variables were optimized to determine the minimum power design for a given flight condition. We reached the following conclusions:

1. Varying the prescribed propulsive force of the vehicle has a large effect on the optimal shaft angle. In turn, the shaft angle has an effect on the optimal

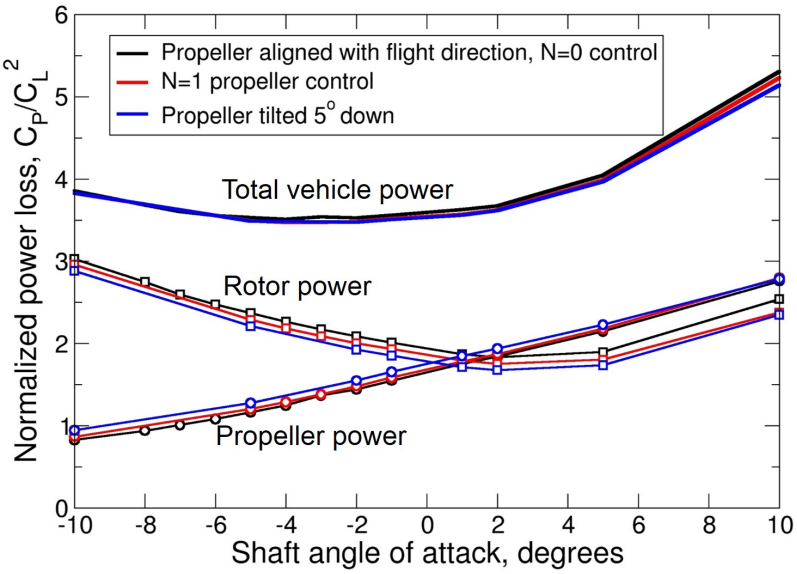

FIGURE 2.18: Normalized power from the baseline compound, a compound using $N = 1$ control on the propeller, and a compound with the propeller angled 5° downwards.

rotor design. Additionally, the optimal shaft angle is highly dependent on the propeller design and efficiency.

2. For the cases considered, higher harmonic control reduces total vehicle power loss by as much as 15 percent compared to conventional control at each configuration's optimal shaft angle. Higher harmonic control results in a more efficient rotor system, leading to an increasingly negative optimal shaft angle. This allows the rotors to provide a larger fraction of the vehicle's propulsive force. The use of higher harmonic control reduces both induced and viscous components of power in part by decreasing the circulation generated on the retreating side of each rotor.

3. Both the conventional and higher harmonic control cases achieve efficient forward flight by operating with a high lateral lift offset equal to about one-half the rotor radius.

4. Constraining the maximum lateral lift offset of a coaxial rotor system to a smaller value, as may be required in the design of an actual rotor, significantly increases the rotor and vehicle power losses. For example, when the maximum lateral lift offset is limited to 30 percent of the rotor radius, total vehicle power loss increases by over 40 percent for both conventional and higher harmonic control.

5. Higher harmonic control dramatically reduces rotor power losses at negative shaft angles when the maximum lateral lift offset is constrained. At high positive shaft angles, the benefit of higher harmonic control is greatly diminished.

6. Higher harmonic control results in a dramatically different optimal shaft angle from conventional control when the maximum lateral lift offset is constrained: $\alpha_{\text{shaft}} = -4°$ for higher harmonic control versus $\alpha_{\text{shaft}} = 6°$ for conventional control. For a constrained maximum lift offset of 0.3, higher harmonic control reduces total vehicle power loss by 11 percent compared to conventional control at each configuration's optimal shaft angle.

7. The use of a lifting wing to supplement rotor lift has a very modest effect on aircraft efficiency, decreasing overall vehicle power loss by less than 1 percent. The optimal wing lift share varies between 22 percent and 43 percent depending on shaft angle. A wing may be more effective at reducing power if the rotor system is also constrained in lift offset, a case that was not analyzed in this paper.

8. Tilting the propeller downwards by 5° to supplement the rotor system's lift reduces total vehicle power loss by 1.5 percent. Using conventional cyclic control on the propeller also allows the propeller to generate a small lift component, reducing vehicle power loss by 1.0 percent.

3

Optimal Coaxial Rotor in Hover

A number of researchers have studied coaxial rotor performance in hover experimentally and using aerodynamic modeling. Coleman [17] provided a comprehensive summary of coaxial rotor research. Nagashima and Nakanishi [18] used a generalized momentum theory and free wake analysis to determine the optimal performance of a coaxial rotor in hover. The authors concluded that hover performance is largely dependent on axial spacing and blade pitch differences between the rotors, and that certain mutual interference effects can be beneficial to performance.

More recently, Leishman and Ananthan [19] formulated the combined Blade Element Momentum Theory (BEMT) for coaxial rotors in hover and axial flight, accounting for axial induced velocities only. Results from that analysis were compared to experimental data from Harrington [57] and showed good agreement. In addition, the authors – building upon the single rotor work of Gessow [58] – asserted that the optimal coaxial hovering rotor is that which produces a uniform disk loading and linear thrust per unit span for each rotor. To achieve torque balance, the slope (in the radial direction) of the thrust distributions will be different, with the upper rotor generating a larger share of the overall system thrust than the less efficient lower

rotor. Juhasz et al. [59] used BEMT to predict the performance of a model-scale coaxial rotor with highly twisted blades, and compared results to a free vortex wake model and a computational fluid dynamics analysis. The authors concluded that BEMT could accurately predict the thrust and torque on the model coaxial rotor. Additionally, although it may miss some fine details of the inflow distributions, its averaged inflow predictions were accurate globally.

Rand and Khromov [20] used the calculus of variations and a BEMT analysis (also neglecting swirl velocities in the wake) to determine the optimal hovering coaxial rotor. Their results demonstrated that a linear thrust distribution on the lower rotor is *not* optimal, a result that differs from Leishman and Ananthan [19] even when using identical assumptions about mutual rotor interference. Rand and Khromov [20] also explore several empirical approximations for determining the mutual interference effects of the two rotors.

Syal and Leishman [21] used both BEMT and a Free Vortex Method (FVM) to formulate a generic optimization technique for a coaxial rotor system in hover using the method of feasible directions. The authors note, however, that the nonconvexity of the problem may limit the usefulness of formal optimization methods, and that extensive parametric studies may still be required.

In this chapter, we build upon the work of Leishman and Ananthan [19] – who formally laid out the coaxial BEMT theory without swirl, and Rand and Khromov [20], who formally optimized the inflow and rotor design of coaxial rotors – to develop a variational approach for determining the optimal torque-balanced coaxial hovering rotor including swirl. We are able to quantify the effects of the swirl component of induced velocity on performance (figure of merit), optimal induced wash distributions, and optimal blade twist and chord distributions.

We will divide the chapter into two sections:

- A section describing the optimization approach *neglecting* the swirl component, and presenting results for this analysis. This methodology is similar to the approach described by Rand and Khromov [20], and provides a good background for the swirl case explored in the second section. Additionally, we will make direct comparisons between the optimal rotor found using this approach and that asserted by Leishman and Ananthan [19]. We show that far better inviscid performance can be achieved by using a negative or small positive loading on the inner portion of the lower rotor, and by generating significantly higher thrust on the outer portion of the lower rotor. In fact, at a thrust coefficient of $C_T = 0.008$, the optimal rotor has a figure of merit that is 12% higher than the Leishman and Ananthan [19] linear thrust distribution rotor.

- A section describing the optimization approach including the swirl component of induced wash, viscous losses, an improved approximation of the mutual interference between the rotors, and tip losses. We present results for this analysis that quantify the effect that the swirl component of induced velocity has on coaxial rotor performance, optimal coaxial rotor design, and optimal induced wash distributions.

3.1 Technical Approach to the Inviscid Optimization without Swirl

As a starting point, we will use the formulation of BEMT described by Leishman and Ananthan [19]. This approach assumes that swirl losses in the flow are small and can therefore be ignored. The flow geometry for the no-swirl configuration at a given blade section is shown in Figure 3.1. V represents the total velocity at the blade, w the induced wash, U_z the axial velocity of the rotor (or any component of inflow not due to the induced velocity of the rotor itself - for example, an induced inflow caused by the second rotor of a coaxial system), Ω is the rotational rate of

the rotor, r the radial position, θ the blade pitch angle, ϕ the inflow angle, and α_{eff} the effective angle of attack. For simplicity, we define an additional variable λ, such

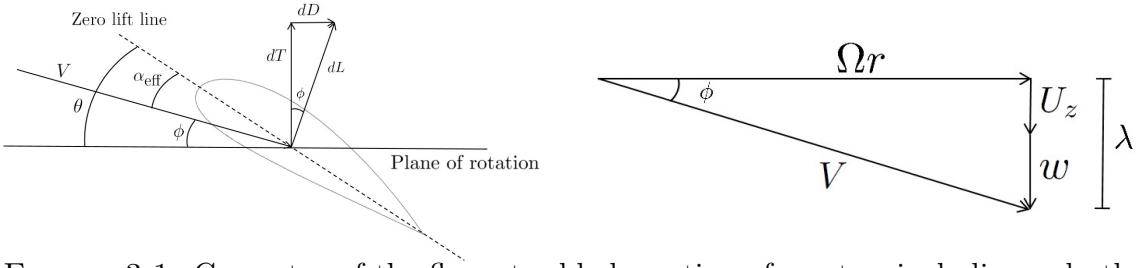

FIGURE 3.1: Geometry of the flow at a blade section of a rotor, including only the axial component of velocity in both the inflow and induced wash.

that $\lambda = w + U_z$, which represents the total inflow velocity at the rotor. We define the following normalized variables:

$$\bar{r} = \frac{r}{R} \quad \bar{U}_z = \frac{U_z}{\Omega R} \quad \bar{w} = \frac{w}{\Omega R} \quad \bar{V} = \frac{V}{\Omega R} \quad \bar{\lambda} = \frac{\lambda}{\Omega R} \tag{3.1}$$

Additionally, the induced flow angle is assumed to be small, allowing us to make the small angle assumption for the related geometry, i.e., $\cos\phi \approx 1$, making $V \approx \Omega R$.

For a single rotor, we define the differential thrust coefficient, dC_T, and differential torque dC_Q, as follows:

$$dC_T = 4F\bar{\lambda}\bar{w}\bar{r}d\bar{r} \tag{3.2}$$

$$dC_Q = 4F\bar{\lambda}^2\bar{w}\bar{r}d\bar{r} \tag{3.3}$$

where F is the Prandtl correction factor, which can be set to values less than one to account for the tip losses inherent in a real, finite bladed rotor. We also know, from Blade Element Theory, that the differential thrust can be described as

$$dC_T = \frac{1}{2}\sigma c_{l\alpha}\left(\theta\bar{r}^2 - \bar{\lambda}\bar{r}\right)d\bar{r} \tag{3.4}$$

where $\sigma = \frac{NB}{\pi R}$ is the rotor solidity and $c_{l\alpha}$ the lift curve slope. Note also that we have made use of the small angle assumption for ϕ in determining the effective angle

of attack, making $\tan\phi \approx \phi = \frac{\bar{\lambda}}{\bar{r}}$. Equation (3.4) also assumes that the differential drag is small relative to the differential lift. For a single rotor, or the upper rotor of a coaxial system, we can equate the two expressions for differential thrust, Eqs. (3.2) and (3.4), giving a quadratic expression for the total inflow, $\bar{\lambda}$, which we can then solve to get the inflow distribution resulting from any twist distribution θ, chord distribution (locally varying σ), and axial advance ratio (or inflow due to a second rotor), $\bar{U}$:

$$\bar{\lambda}(\bar{r}, \bar{U}_z) = \sqrt{\left(\frac{\sigma c_{l\alpha}}{16F} - \frac{\bar{U}_z}{2}\right)^2 + \frac{\sigma c_{l\alpha}}{8F}\theta\bar{r}} - \left(\frac{\sigma c_{l\alpha}}{16F} - \frac{\bar{U}_z}{2}\right) \tag{3.5}$$

Following the Reference [19] approach, in order to extend this analysis to the lower rotor of a coaxial system, we must account for the presence of the contracted wake of the upper rotor in the lower rotor's inflow, $\bar{\lambda}$. We divide the two rotors into three separate components: the upper rotor, designated with the subscript u, the portion of the lower rotor operating in the upper rotor's wake, denoted by the subscript $\ell 1$, and the portion of the lower rotor operating outside of the upper rotor's wake, $\ell 2$, as shown conceptually in Figure 3.2. The portion of the lower rotor operating in

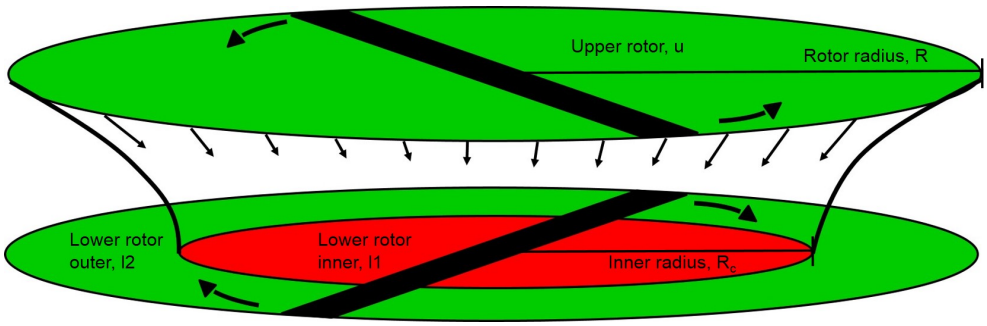

FIGURE 3.2: Illustration of the upper rotor's contracted wake acting on the inner portion of the lower rotor within a coaxial configuration.

the upper rotor's contracted wake has radius r_c, giving it a total area of A_c. We assume the inflow is contracted and then mapped onto this lower portion of the rotor, giving it a final inflow velocity of $\left(\frac{A}{A_c}\right)\bar{\lambda}_u$. The influence of the lower rotor on

the upper rotor is not considered in this analysis. Finally, the contraction ratio of the upper rotor's wake $\frac{A_c}{A}$ must be assumed *a priori* from either momentum theory or experimental results.

Similar to the upper rotor, we can equate the different expressions for differential thrust and solve for the lower rotor's inflow distribution λ_l, giving

$$\bar{\lambda}_\ell(r) = \sqrt{\left(\frac{\sigma c_{l\alpha}}{16F} - \frac{\frac{A}{A_c}\bar{\lambda}_u}{2}\right)^2 + \frac{\sigma c_{l\alpha}}{8F}\theta_l \bar{r}} - \left(\frac{\sigma c_{l\alpha}}{16F} - \frac{\frac{A}{A_c}\bar{\lambda}_u}{2}\right) \tag{3.6}$$

for $r \leq r_c$. Equation 3.5 can be used for values of $r > r_c$, i.e., areas on the lower rotor outside of the upper rotor's wake, denoted as $l2$.

Once the inflow distribution for each rotor is known, we can compute the overall thrust coefficient of each rotor, C_T, by integrating the differential thrust over the span of the blade as follows

$$C_T = \int_{\bar{r}=0}^{\bar{r}=1} dC_T = \int_{\bar{r}=0}^{\bar{r}=1} 4F\bar{\lambda}\bar{w}\bar{r}d\bar{r} \tag{3.7}$$

Similarly, the power coefficient of each rotor can be computed using

$$C_P = \int_{\bar{r}=0}^{\bar{r}=1} \bar{\lambda} dC_T + \frac{1}{2}\int_{\bar{r}=0}^{\bar{r}=1} \sigma C_D r^3 dr \tag{3.8}$$

where the first integral represents the induced component of power and the second integral represents the viscous component of power. For the analysis described in this section, we will focus on minimizing the induced component of power only.

3.1.1 Optimization Approach

To determine the optimal rotor design, we solve a constrained optimization problem using the calculus of variations. We seek to minimize the induced power subject to the following two constraints:

- The rotor system must generate a specified coefficient of thrust.
- The torque on the rotors must be equal and opposite, i.e., the coaxial system is in torque balance.

To solve this constrained optimization problem, we adjoin to the power to be minimized the two equality constraints using Lagrange multipliers ν_T and ν_Q, forming the Lagrangian power Π,

$$\Pi = C_{Pu} + C_{P\ell 1} + C_{P\ell 2} - \nu_T(C_{Tu} + C_{T\ell 1} + C_{T\ell 2} - T_{\text{req}}) - \nu_Q(C_{Pu} - C_{P\ell 1} - C_{P\ell 2}) \quad (3.9)$$

Note that in Eq. (3.9) we segregate the contributions to the thrust and power from each of the three distinct regions of the coaxial rotor system shown in Figure 3.2.

We perform the optimization using one of two sets of design variables we wish to optimize. We can use momentum theory only to solve for the optimal induced wash distribution, w, or we can use combined Blade Element Momentum Theory to solve for the optimal blade twist distribution θ. When setting the Prandtl tip correction factor to a value of 1, the optimal performance computed by the two methods is identical, as the correct twist distribution can be chosen to generate any induced wash distribution.

For simplicity, we will first consider optimizing only the induced wash on each rotor, w. We can apply the Euler-Lagrange equations to find the stationary point of the Lagrangian, Π, with respect to the induced wash distribution w and the Lagrange multipliers, ν:

$$\frac{\partial \Pi}{\partial q} - \frac{d}{dr}\left(\frac{\partial \Pi}{\partial q'}\right) = 0 \quad (3.10)$$

where $q = (w, \nu_T, \nu_Q)$ and the prime denotes a derivative with respect to the radial coordinate r. Because the Lagrangian power does not contain derivatives of the

independent variable r, the Euler-Lagrange equations are simply

$$\frac{\partial \Pi}{\partial w} = 0 \tag{3.11}$$

$$\frac{\partial \Pi}{\partial \nu_T} = 0 \tag{3.12}$$

$$\frac{\partial \Pi}{\partial \nu_Q} = 0 \tag{3.13}$$

In practice, solving the problem is complicated slightly by a couple of factors. First, the inflow on the inner portion of the lower rotor is a function of the inflow on the upper rotor. Second, finding a closed form expression that satisfies Eqs. (3.11), (3.12), and (3.13) is difficult if not impossible. As a result, we make use of an iterative technique to arrive at the solution.

To start, we assume an initial required thrust for the upper and lower rotor, setting $C_{T\mathrm{req}U} = C_{T\mathrm{req}L} = \frac{1}{2}C_{T\mathrm{req}}$. We can then form a statement of Lagrangian power for each individual rotor. For simplicity, we will write this equation using variables for the upper rotor. Note, however, that these equations are equally valid for the lower rotor. The Lagrangian power for a single rotor is

$$\Pi_u = C_{Pu} - \nu_{Tu}(C_{Tu} - C_{T\mathrm{req}U}) \tag{3.14}$$

which, when substituting in the expressions for differential thrust and power given in Eqs. (3.2) and (3.3), becomes

$$\Pi_u = \int_{\bar{r}=0}^{\bar{r}=1} \left[4\bar{\lambda}_u^2 \bar{w}_u \bar{r} - \nu_{Tu}(4\bar{\lambda}_u \bar{w}_u \bar{r} - C_{T\mathrm{req}U})\right] d\bar{r} \tag{3.15}$$

Equation (3.11) states that at the stationary point of the Lagrangian, the derivative of the integrand with respect to the upper rotor's wash will be equal to zero. Splitting the total inflow into its component parts ($\bar{\lambda} = \bar{U}_z + \bar{w}_u$) and performing this differentiation gives:

$$\frac{\partial \Pi}{\partial w_u} = 0 = 3\bar{w}_u^2 + 4\bar{w}_u \bar{U}_z + \bar{U}_z^2 - \nu_{Tu}(2\bar{w}_u + \bar{U}_z) \tag{3.16}$$

We can then find the following expression for the induced wash distribution w_u that satisfies Eq. (3.16)

$$\bar{w}_u = \frac{1}{3}\left(-2\bar{U}_z + \nu_{Tu} - \sqrt{\bar{U}_z^2 - \bar{U}_z\nu_{Tu} + \nu_{Tu}^2}\right) \tag{3.17}$$

Equation 3.17 will yield the optimal induced wash distribution (when considering axial induced wash only) for any rotor with axial inflow distribution $\bar{U}_z$. By changing the value of the Lagrange multiplier ν_{Tu}, we can vary the thrust generated by the rotor. Note that the induced wash distribution $\bar{w}_u$ and inflow $\bar{U}_z$ are continous functions that can vary with radial position $\bar{r}$.

To apply Eq. (3.17) to the inner portion of the lower rotor, we set $\bar{U}_{zl1} = \frac{A}{A_c}\bar{\lambda}_u$. By treating the rotors separately, we can ensure that they both generate a given thrust with minimum induced power loss. In order to satisfy the overall system constraint on torque balance, we perform the following iteration:

1. Assume an initial required thrust for the upper and lower rotor by setting $C_{T\text{req}U} = C_{T\text{req}L} = \frac{1}{2}C_{T\text{req}}$.

2. Compute the optimal induced wash distribution for the upper rotor that achieves this thrust using Eq. (3.17) and iteratively updating the Lagrange multiplier ν_{Tu}.

3. Use the known upper rotor inflow distribution $\bar{\lambda}_u$ to compute the optimal induced wash distribution of the lower rotor that provides the required thrust, again by using Eq. (3.17) and iteratively updating the value of ν_{Tl} until the lower rotor thrust constraint is satisfied.

4. Compute the torque of each rotor (which in this non-dimensionalized, inviscid case is simply the induced power loss), and adjust the required thrust of each

rotor by computing a torque correction factor using

$$Q^{k+1}_{\text{correction}} = C^{k}_{Q\text{correction}} - \frac{1}{2}\frac{C_{Pu} - C_{P\ell}}{C_{P\text{tot}}} \tag{3.18}$$

assuming $Q^{0}_{correction} = \frac{1}{2}$. Update the required thrust on the upper and lower rotor using this factor as follows

$$C^{k+1}_{T\text{req}U} = C^{k}_{T\text{req}U} Q_{\text{correction}} \tag{3.19}$$

$$C^{k+1}_{T\text{req}L} = C_{T\text{req}} - C^{k+1}_{T\text{req}U} \tag{3.20}$$

and return to step 2 until the rotor induced power losses are equal.

This algorithm solves for the induced wash distributions on the three rotor components that yield minimum induced power while satisfying constraints on total system thrust and maintaining torque balance between the two rotors. To determine the optimal blade twist, we apply a very similar approach, making use of Eqs. (3.5) and (3.33) to express the total inflow distributions $\bar{\lambda}_u$ and $\bar{\lambda}_l$ as functions of the blade twists, θ_u and θ_l. We can also incorporate the tip loss F into the iteration with minimal further complication.

3.1.2 Inviscid Results, Without Swirl

We applied the previously described optimization methodology to a coaxial rotor in order to determine the minimum induced loss coaxial rotor in hover. Because we are only optimizing for induced losses, for plots in which we display twist distributions, we assume rectangular blades and do not vary the chord distribution, as the inflow can be controlled through the blade twist alone, and chord distribution would be a significant factor in a viscous optimization only. Additionally, because we are performing an inviscid analysis, we consider only the induced power associated with each rotor design, as this was the only component minimized in the optimization. The torque balance is also achieved in terms of induced losses only, *i.e.*, the induced

power loss from the two rotors is equal. We constrain the rotor system to generate a total coefficient of thrust equal to $C_T = 0.008$. For the purposes of the comparison, we assume an ideal wake contraction ratio based on momentum theory of $r_c = \frac{1}{\sqrt{2}}$, and neglecte tip losses in the optimization and performance evaluation. We compare the optimal rotor to a coaxial rotor using a linear thrust distribution on each rotor, which is the deduced optimum from Reference [19].

Figures 3.3 shows the induced Figure of Merit (FOM) versus the thrust coefficient for the two rotors. Note that for the inviscid analysis performed in this section, we have defined the figure of merit based on the weighted thrust definition of Reference [60], accounting for the thrust difference between the rotors required to maintain torque balance:

$$FOM = \frac{P_{\text{ideal}}}{P_{\text{actual}}} \tag{3.21}$$

where

$$P_{\text{ideal}} = \frac{C_{Tu}^{3/2}}{\sqrt{2}} + \frac{C_{T\ell}^{3/2}}{\sqrt{2}} \tag{3.22}$$

We use the Eq. (3.22) definition of ideal power in this section, rather than the conventional definition for a single rotor ($P_{\text{ideal}} = \frac{C_{\text{Tot}}^{3/2}}{\sqrt{2}}$), because without viscous losses and with the added effective area of a second rotor, we obtain Figure of Merits based on the classical definition for the coaxial rotors greater than unity. Of course, the choice of a reference value is arbitrary for the comparisons we perform here, as all rotors being compared have the same total area and are over the same range of thrust coefficients. For convenience, in the following section where we do include viscous losses, we revert back to the conventional Figure of Merit definition.

The optimal coaxial rotor has a higher FOM at all thrust coefficients, and most importantly, has a 12% higher FOM at the design point of $C_T = 0.008$. Figure 3.4 is a plot of the thrust coefficient versus the induced power coefficient for the two

rotors. Note that the optimal rotor produces a higher thrust coefficient for a given induced power coefficient over the entire domain, including once again at the design point. These results indicate that using a linear thrust distribution on the two rotors of a coaxial system is not optimal, at least in terms of achieving minimum induced power.

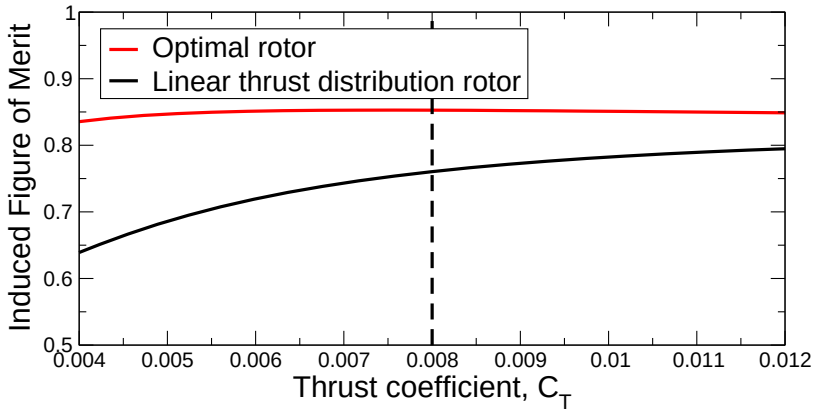

FIGURE 3.3: Figure of merit versus the thrust coefficient for the optimal coaxial rotor and the linear thrust distribution rotor, each designed for a thrust coefficient of $C_T = 0.008$.

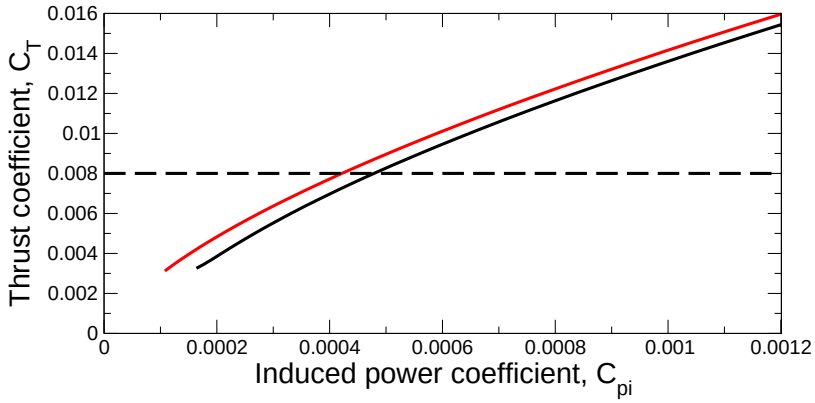

FIGURE 3.4: Thrust coefficient versus the induced power coefficient for the optimal coaxial rotor and the linear thrust distribution rotor, each designed for a thrust coefficient of $C_T = 0.008$.

Figure 3.5 shows the optimal spanwise distribution of non-dimensional induced wash on the upper and lower rotors for the optimal coaxial rotor compared to the linear thrust distribution rotor. Figure 3.6 shows the spanwise non-dimensional thrust

distribution, torque distribution, blade twist, and coefficient of lift for the optimal rotor compared to the linear thrust distribution rotor. The inner portion of the optimal lower rotor, operating in the contracted wake of the upper rotor, is nearly entirely off-loaded, and in fact has a *negative* induced wash in this region, generating a slightly negative total thrust and negative induced torque. In fact, this portion of the rotor is actually being driven by the wash from the upper rotor. The outer portion of the lower rotor, able to operate with a lower inflow because of the assumption that it is not influenced by the upper rotor's wash, then generates a much larger thrust more efficiently, resulting in a lower overall induced power for the system. The upper rotor in both cases has a uniform induced inflow as expected, resulting in the minimum induced loss performance. The only difference between the upper rotor's design between the two cases is that to achieve torque balance, the upper rotor of the linear thrust distribution case provides more of the total system thrust, causing the upper rotor to have the same power loss as the lower rotor and ensure torque balance. In the optimal case, the lower rotor provides a given thrust for less total power, meaning that in the torque balanced condition, the lower rotor is providing more of the total system thrust, although still significantly less than the upper rotor.

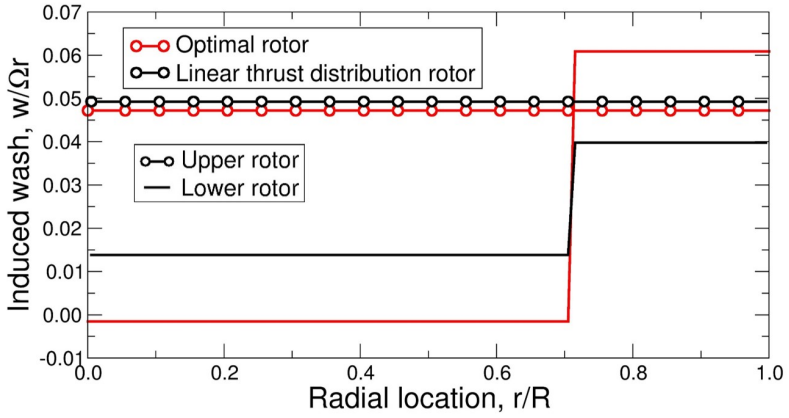

FIGURE 3.5: Radial distribution of induced wash for the optimal coaxial rotor compared to the linear thrust distribution rotor.

The lower rotor of the optimal coaxial rotor has a drastically different lift coefficient distribution than the linear thrust distribution rotor. The lower rotor's blade twist is also very different between the two cases; the optimal rotor uses a smaller twist on the inner portion of the blade, to maintain a negative overall thrust, and then a much larger positive twist on the outer portion.

The non-swirl optimal coaxial rotor shown here is in agreement with the optimization methodology of Reference [20] if applied using the same assumptions about mutual rotor interference, which was not done in Reference [20].

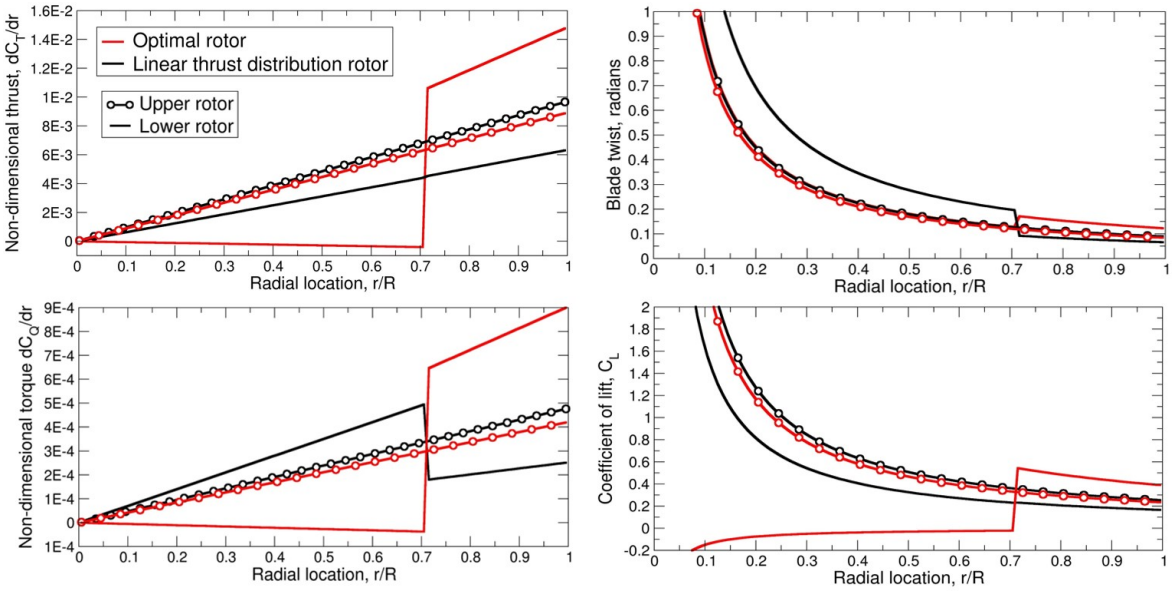

FIGURE 3.6: Radial distribution of thrust, torque, twist, and lift coefficient for the optimal coaxial rotor compared to the linear thrust distribution rotor.

As a further check that the optimal rotor as determined by our optimization analysis has in fact achieved the minimum induced power condition, we vary the share of the lower rotor's total thrust generated by the inner portion of the rotor and evaluate the resulting induced power at the design point, shown in Figure 3.7. For the ideal wake contraction ratio assumed here, a value of $C_{T\ell 1}/C_{T\ell} = 0.5$ is equivalent to a linear thrust distribution. A negative value of $C_{T\ell 1}/C_{T\ell}$ indicates that the inner portion is generating a negative thrust, as is the case with the optimal

rotor, which has a value of $C_{T\ell 1}/C_{T\ell} = -0.0407$. As the plot shows, the optimization methodology described here results in the thrust sharing between the inner and outer portions of the lower rotor that yields the minimum induced power.

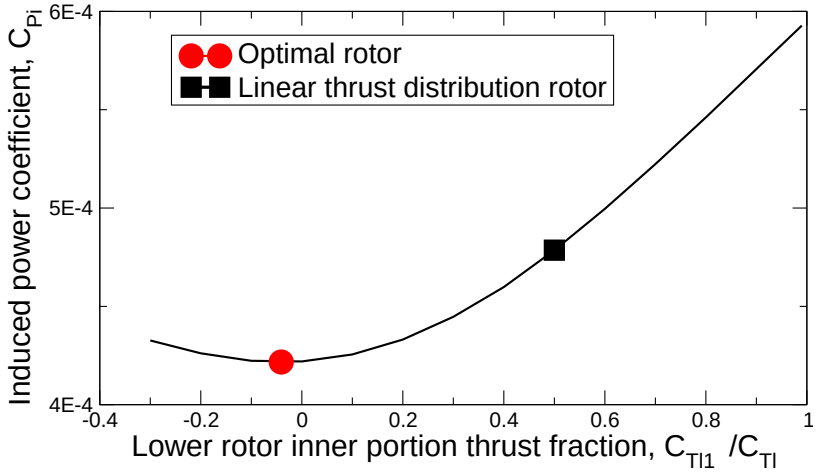

FIGURE 3.7: Induced power coefficient versus the fraction of total lower rotor thrust generated by the inner portion operating in the upper rotor's contracted wake.

These results indicate that previously held beliefs about the design and limits of performance for a coaxial hovering rotor, at least within the simple framework of an inviscid BEMT analysis, may be incorrect. A linear thrust distribution and uniform disk loading does not result in the minimum induced losses. Rather, by using a variational approach to the problem, similar to that outlined by Rand and Khromov in Reference [20], we find that the minimum induced loss coaxial rotor generates a negative thrust on the inboard portion of the lower rotor, and a large, positive thrust on the outer portion of the lower rotor, achieving a 12% improvement in the inviscid Figure of Merit at $C_T = 0.008$. While the approach to aerodynamic modeling used in this analysis involves many simplifications, it may be important to recognize and understand the fundamental limits of induced power performance and the rotor design that achieves this performance. As we will see in the following section, even when improving the realism of our model by including viscous losses, tip

losses, the swirl component of induced velocity, and an improved mutual interference model, the optimal rotor still retains many of the features of the inviscid optimum, particularly using a lower rotor that is very lightly loaded on its inner portion and very highly loaded towards the tip.

3.2 Technical Approach to the Viscous Optimization Including Swirl

3.2.1 Combined Blade Element Momentum Theory Including Swirl

To incorporate losses due to swirl, and the effect on blade design of these losses, we make use of the momentum theory including swirl described by Modarres and Peters [61].

Consider a single rotor with rotational speed Ω operating with some inflow U, which can include axial and swirl components U_z and U_θ. Figure 3.8 shows the resultant relative velocity vector including the effects of induced wash w and blade rotation Ωr. The sine and cosine of the relative flow angle ϕ at a radial station r are

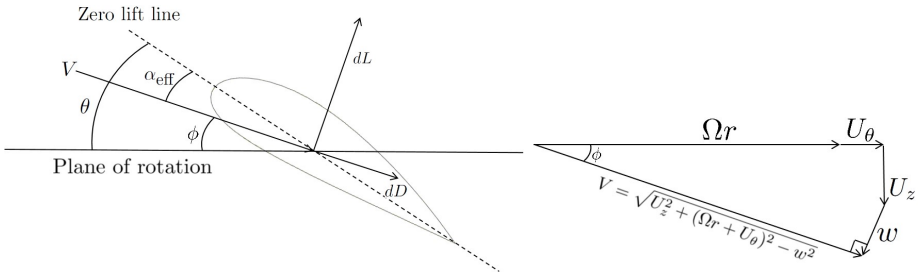

FIGURE 3.8: Geometry of the flow at a blade section of a rotor, including the swirl component of velocity in both the inflow and induced wash.

given by

$$\sin\phi = \frac{U_z\sqrt{U_z^2 + (\Omega r + U_\theta)^2 - w^2} + w(\Omega r + U_\theta)}{U_z^2 + (\Omega r + U_\theta)^2} \tag{3.23}$$

$$\cos\phi = \frac{(\Omega r + U_\theta)\sqrt{U_z^2 + (\Omega r + U_\theta)^2 - w^2} - wU_z}{U_z^2 + (\Omega r + U_\theta)^2} \tag{3.24}$$

where V is the total local airspeed relative to the airfoil given by

$$V = \sqrt{U_z^2 + (\Omega r + U_\theta)^2 - w^2} \tag{3.25}$$

Following [61], we can perform a momentum balance to obtain expressions for the differential thrust and power that account for both axial and swirl components of induced velocity. The differential lift, dL, acting perpendicular to the relative velocity is given by

$$dL = 4\pi\rho F \left[U_z + w\cos\phi\right](w) r dr \tag{3.26}$$

where ρ is the density and F is the Prandtl tip loss factor. This force can then be resolved into the axial and circumferential directions using Eqs. (3.23) and (3.24). From this expression for the differential lift, we find the following equations for the thrust, T, and induced power, P_i, i.e.,

$$T = \int_{R_{CO}}^{R} 4\pi\rho \left[U_z + w\cos\phi\right](w\cos\phi) r dr \tag{3.27}$$

$$P_i = \int_{R_{CO}}^{R} 4\pi\rho \left[U_z + w\cos\phi\right](w\sin\phi)\Omega(r + U_\theta) r dr \tag{3.28}$$

where R is the rotor radius and R_{CO} is the radius of the root cutout. We can see from Figure 3.8 that the profile drag of the blade also contributes to the thrust and in-plane drag of the rotor. We express the total profile drag of the blade as

$$dD_{\text{prof}} = \frac{1}{2}\rho N(U_z^2 + (\Omega r + U_\theta)^2 - w^2) c c_d dr \tag{3.29}$$

where N is the number of blades and c_d is the sectional coefficient of drag. We can resolve the profile drag force into its axial and circumferential directions again using Eqs. (3.23) and (3.24).

Including the profile drag's contribution to the total thrust and power, and nondi-

mensionalizing gives

$$C_T = \int_{\bar{r}_{CO}}^{1} \Big[4(\bar{U}_z + \bar{w}\cos\phi)\bar{w}\cos\phi\bar{r} - \sin\phi\frac{N\bar{c}c_d}{2\pi}\left(\bar{U}_z^2 + (\bar{r}+\bar{U}_\theta)^2 - \bar{w}^2\right)\Big] d\bar{r} \tag{3.30}$$

$$C_P = \int_{\bar{r}_{CO}}^{1} \Big[4\left(\bar{U}_z + \bar{w}\cos\phi\right)\bar{w}\sin\phi\bar{r}(\bar{r}+\bar{U}_\theta) + \cos\phi\frac{N\bar{c}c_d}{2\pi}\left(\bar{U}_z^2 + (\bar{r}+\bar{U}_\theta)^2 - \bar{w}^2\right)(\bar{r}+\bar{U}_\theta)\Big] d\bar{r} \tag{3.31}$$

where we have normalized all velocities by ΩR and all lengths by R, and have expressed normalized quantities with an overbar, i.e., $w/\Omega R = \bar{w}$.

To extend this analysis to a coaxial rotor system, we must account for the mutual interaction of the two rotors. We assume the upper rotor's inflow is contracted and mapped onto the inner portion of the lower rotor, as illustrated in Figure 3.2. The contracted wake at the lower rotor has a total area of A_c, giving the inner portion of the lower rotor an inflow velocity of

$$\bar{U}_{\ell 1 z} = \left(\frac{A}{A_c}\right)\bar{w}_{uz} \tag{3.32}$$

$$\bar{U}_{\ell 1 \theta} = \left(\frac{A}{A_c}\right)^{3/2}\bar{w}_{u\theta} \tag{3.33}$$

where the subscripts u and $\ell 1$ denote variables associated with the upper rotor and inner portion of the lower rotor, respectively, and the subscript c denotes a wake contracted quantity.

We account for the influence of the lower rotor on the upper rotor by including a uniform axial downwash acting on the upper rotor that is induced by the lower rotor. To determine the magnitude of this downwash, we use the influence coefficient model developed by McAlister et al. [49] and used in the evalution of BEMT predictions

by Juhasz et al. [59]. Using the Biot-Savart law and an empirical parameter k, the induced velocity due to a helical vortex filament trailing from the tip of a rotor in hover, measured at radial position $r = 0$ and axial position $\bar{z}$ (normalized by rotor radius) is given by

$$\frac{\bar{U}_z}{\bar{U}_z|_{\bar{z}=0}} = 1 + \left(\frac{|\bar{z}|}{\sqrt{1+\bar{z}^2}}\right)^k \text{sign}(\bar{z}) \tag{3.34}$$

The exponent k is set to a value of $0.3 - 0.5$ when analyzing points above the rotor and a value of 0.6 when analyzing points below the rotor. We set $U_z|_{\bar{z}=0}$ equal to the average induced axial velocity on the lower rotor. There are no swirl velocities induced on the upper rotor due to the lower rotor. We also use Eq. (3.34) to approximate the radial contraction r_c of the upper rotor's wake as a function of vertical separation. However, for the influence of the upper rotor on the lower rotor, we map the induced velocity as a function of radius from the upper rotor to the contracted portion of the lower rotor.

3.2.2 Optimization Approach

To determine the optimal induced velocity distribution, $\bar{w}$, on each rotor, we formulate and solve a constrained optimization problem using the calculus of variations. We seek to minimize the total power subject to two constraints, i.e., (1) that the rotor system generates a specified coefficient of lift, and (2) that the torque on the rotors is equal and opposite (the rotors are in torque balance).

To solve this constrained optimization problem, we use a similar approach to that described in Section 3.1.1, defining our Lagrangian power with Eq. (3.9) and applying the Euler-Lagrange equations given in Eqs (3.11), (3.12), and (3.13). Once again, application of the Euler-Lagrange equations results in a set of coupled integro-algebraic equations for the unknown induced wash distribution (and the resulting load and torque distributions). Similar to the no swirl case, solving the optimization

problem is complicated by the fact that the inflow on the inner portion of the lower rotor is a function of the the induced wash on the upper rotor, and the inflow on the upper rotor is a function of the induced wash on the lower rotor. Thus, we solve for the optimal solution numerically.

To start, we assume an initial required thrust for the upper and lower rotor, setting $C_{T\text{req}U} = C_{T\text{req}L} = \frac{1}{2}C_{T\text{req}}$. We then form a statement of Lagrangian power for each individual rotor. For simplicity, we will write this equation using variables for the upper rotor. (Note, however, that these equations are equally valid for the lower rotor.) The Lagrangian power for a single rotor is

$$\Pi_u = C_{Pu} - \nu_{Tu}(C_{Tu} - C_{TreqU}) \tag{3.35}$$

which, when substituting in the expressions for differential thrust and power given in Eqs. (3.30) and (3.31), becomes

$$\begin{aligned}\Pi = \int_{\bar{r}_{CO}}^{1} \Bigg[& 4\left(\bar{U}_z + \bar{w}\cos\phi\right)\bar{w}\sin\phi\bar{r}(\bar{r}+\bar{U}_\theta) \\ & + \cos\phi\frac{N\bar{c}c_d}{2\pi}\left(\bar{U}_z^2 + (\bar{r}+\bar{U}_\theta)^2 - \bar{w}^2\right)(\bar{r}+\bar{U}_\theta) \\ & - \nu_{Tu}\Bigg(4(\bar{U}_z + \bar{w}\cos\phi)\bar{w}\cos\phi\bar{r} \\ & - \sin\phi\frac{N\bar{c}c_d}{2\pi}\left(\bar{U}_z^2 + (\bar{r}+\bar{U}_\theta)^2 - \bar{w}^2\right) - C_{Treq}\Bigg)\Bigg]\, d\bar{r}\end{aligned} \tag{3.36}$$

To put the Lagrangian solely in terms of the induced wash distribution $\bar{w}$, we make use of Eqs. (3.23) and (3.24), which describe $\cos\phi$ and $\sin\phi$ in terms of the induced wash, inflow, and radial position. Substituting these expressions into Eq. (3.36) yields an expression for the Lagrangian power in terms of $\bar{w}$. Note however, that because of the profile power terms, the Lagrangian power is still a function of the sectional drag coefficient c_d and the chord $\bar{c}$, which are not necessarily known a priori.

As a result, we must perform the optimization about some initial values of $\bar{c}$ and c_d and perform the process iteratively, updating $\bar{c}$ and c_d until convergence.

Equation (3.11) states that at the stationary point of the Lagrangian, the derivative of the Eq. (3.36) integrand with respect to the upper rotor's wash will be equal to zero. However, finding an analytical solution for the radial wash $\bar{w}$ that satisfies Eq. (3.11) is intractable. Instead, we discretize Eq. (3.11) and use Newton iteration to arrive at the optimal induced wash distribution at each station i, that is, we find $\bar{w}_i$ such that $\partial\Pi/\partial\bar{w}_i = 0$. Using Newton iteration gives

$$\bar{w}_i^{k+1} = \bar{w}_i^k - \frac{\partial\Pi/\partial\bar{w}_i}{\partial^2\Pi/\partial\bar{w}_i^2} \tag{3.37}$$

Solving Eq. (3.11) using the iterative scheme given in Eq. (3.37) gives the optimal induced wash distribution for both axial and swirl induced washes for any rotor with axial inflow distribution $\bar{U}_z$, swirl inflow distribution $\bar{U}_\theta$, chord distribution $\bar{c}$ and sectional coefficient of drag distribution c_d. By changing the value of the Lagrange multiplier ν_{Tu}, we can vary the thrust generated by the rotor.

Once the optimal induced wash distribution is known, we determine the radial blade twist and chord distribution that generates the minimum induced loss wash distribution with minimum profile losses. The differential lift on a section of the rotor is given by Blade Element Theory as

$$d\bar{L} = \left(\frac{N\rho\bar{c}c_l}{2}\right)\left(\bar{r}^2 + \bar{U}_z^2 - \bar{w}^2\right) \tag{3.38}$$

We set the sectional lift coefficient c_l equal to the value that corresponds with the airfoil section's maximum c_l/c_d. We assume a linear lift curve, $c_l = c_{l\alpha}\,(\theta - \phi)$, which allows us to solve for the optimal blade twist using

$$\theta_{\text{opt}} = \phi + \frac{c_l}{c_{l\alpha}} \tag{3.39}$$

We equate the BET statement of differential lift with the momentum balance statement from Eq. (3.26), which yields the optimal chord value,

$$\bar{c}_{opt} = \frac{8F\pi \left(\bar{U}_z + \bar{w}\cos\phi\right)\bar{w}\bar{r}}{Nc_l\left((\bar{r}+\bar{U}_\theta)^2 + \bar{U}_z^2 - \bar{w}^2\right)} \tag{3.40}$$

In Eqs. (3.39) and (3.40), we have incorporated the Prandtl tip loss factor F into the optimal twist and chord equations. F is only a function of the number of blades, radial position, and induced wash, all of which are already known. The rotor geometry computed using this process will generate the optimal induced wash distributions accouting for tip effects for rotors with a finite number of blades.

Note that this process does not necessarily produce a true total power minimum solution. Rather, we are determining the twist and chord distribution that minimize profile power losses *while also generating the minimum induced loss wash distribution.* In other words, this method assumes that the minimum induced loss wash distribution will result in the minimum total power, an assumption that is not necessarily true. However, this method does provide a very close approximation to the total power optimum and has been used by several other authors, for example Modarres and Peters [61] and Rand and Khromov [20].

The numerical approach for finding optimal rotors consists of four nested loops. We first use an inner loop to determine the correct mutual interference of the two rotors. A second loop is used to adjust the Lagrange multipliers on each rotor to ensure each rotor is generating the required thrust coefficient. A third loop is used to adjust the required thrusts of each rotor to satisfy the torque balance constraint. Finally, an outer loop is used to recompute the optimal torque balanced rotor given the new optimal chord distribution. This alorithm is demonstrated graphically in Figure 3.9.

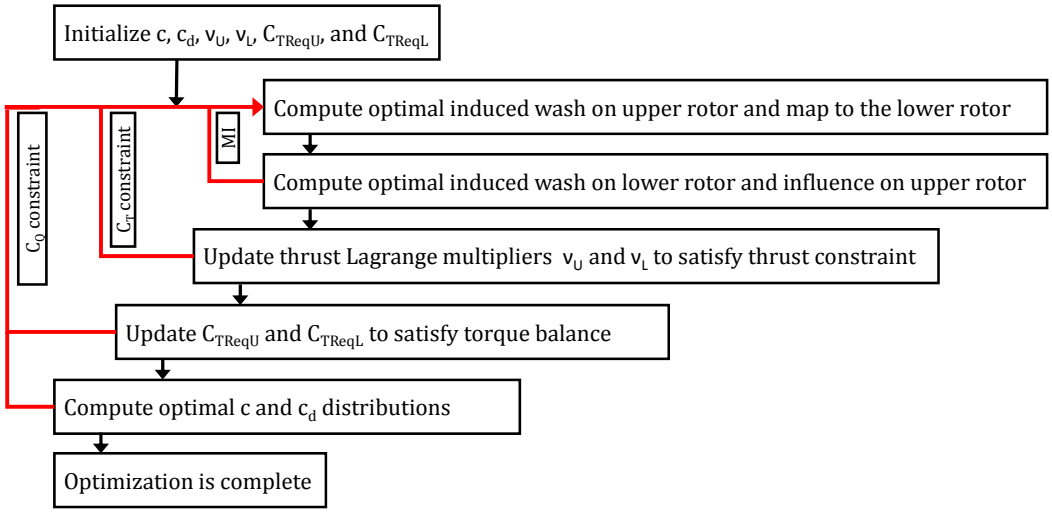

FIGURE 3.9: Algorithm used to determine the optimal torque balanced hovering rotor with swirl and mutual interference.

3.3 Computational Results

3.3.1 Comparison of BEMT Method with and without Swirl to Experimental Results

We first compare results of the coaxial BEMT analysis method, both with and without swirl, to the experimental results from Harrington [57], to both determine the accuracy of the combined BEMT formulation and to illustrate the effect of including swirl on the BEMT analysis of a given coaxial rotor. We compare results to Harrington's rotor 2, which is comprised of coaxial two bladed rotors rigidly restrained in flapping and in the plane of rotation. The rotors have a vertical separation of $\bar{z} = 0.16$ and the blades are untwisted with a uniform chord distribution of $\bar{c} = 0.12$.

We assume a linear lift curve with slope $c_{l_\alpha} = 5.7$ and a quadratic drag polar $c_d = c_{d0} + c_{d1}c_l + c_{d2}c_l^2$ with coefficients $c_{d0} = 0.011$, $c_{d1} = 0.0$, and $c_{d2} = 0.028$. In the influence coefficient model, Eq. (3.34), we use a value of $k = 0.6$ below the rotor, resulting in a wake contraction of $r_c/R = 0.866$. We model the influence of the upper rotor on the lower rotor operating within the upper rotor's contracted wake, and approximate the influence of the lower rotor as a uniform downwash on

the upper rotor, as described in the Approach section. We include the Prandtl tip loss factor to approximate the induced downwash near the tip of each rotor as a result of the finite number of rotor blades. We do not include a root cutout in this analysis.

For the analysis conducted here, we measure coaxial rotor performance using the conventional figure of merit (FM) given by

$$FM = \frac{C_T^{3/2}}{\sqrt{2}C_P} \tag{3.41}$$

which is consistent with the figure of merit definition used by Coleman [17]. Note that this conventional figure of merit can be converted to the alternative coaxial definition 1 given by Leishman and Syal [60] by multiplying it by a factor of $1/\sqrt{2}$.

Figure 3.10 shows the figure of merit versus the coefficient of thrust for the Harrington rotor 2 experimental results and the present combined BEMT analysis both with and without swirl. For each of the BEMT results, the total power loss from the two rotors is equal, i.e., the coaxial system is in torque balance, consistent with the Harrington experimental results. We see that, at least in terms of global performance predictions, the BEMT analysis is in good agreement with experimental results, consistent with the findings of Juhasz et al. [59], and Leishman and Ananthan [19]. We also see that including swirl in the analysis results in a decrease in figure of merit (for this particular rotor) of about half a percent at a thrust coefficient of $C_T = 0.01$, a relatively small effect, and that the difference between the computed figure of merit with and without swirl increases with increasing thrust coefficient.

3.3.2 Optimized Rotor Results – Single Rotor

First, we apply an inviscid version of our optimization methodology to a single rotor including swirl and compare our results to two other known results – the Betz inflow distribution [62] and the optimal inflow distribution described by Glauert [63]. For

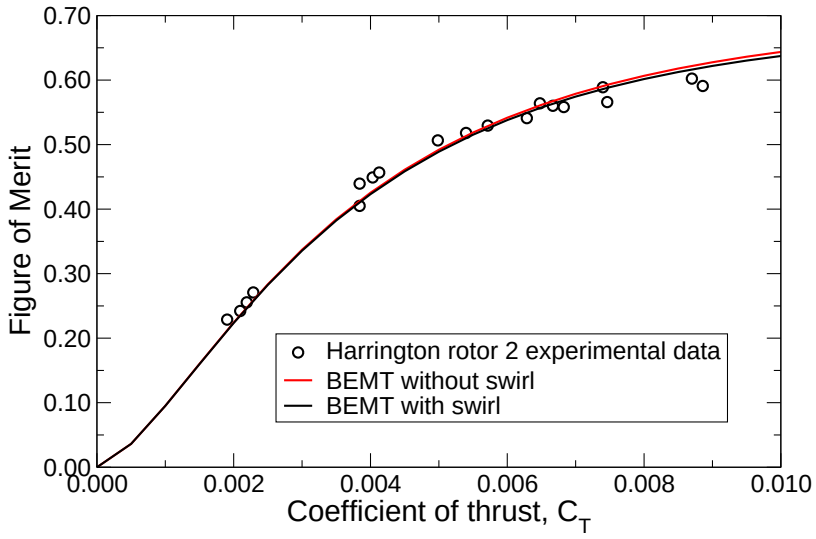

FIGURE 3.10: Figure of merit versus coefficient of thrust for experimental results of the Harrington Rotor 2 [57] compared to BEMT results, both with and without swirl.

a single rotor, the optimization process is significantly simplified, as there is no need for a mutual interference model or a constraint on torque balance. Additionally, because this is an inviscid optimization, we don't include profile losses and their effect on thrust and torque. Finally, to compare our optimal solution to these results, we neglect tip losses, setting $F = 1$.

The Betz propeller inflow distribution [62] has the parametric form

$$w(r) = w_0 \cos\phi \tag{3.42}$$

such that the induced flow remains along a helix as it leaves the rotor disk. However, as described by Glauert [63], this induced wash distribution is close, but not equal to the optimal solution. In fact, slightly better performance can be achieved through a more complex induced wash distribution found by setting the ratio of the increments of thrust and torque to be independent of the radial coordinate. When we apply our optimization methodology to a single rotor including swirl, we recover the more complex (and higher performing) optimal solution mentioned by Glauert [63].

Figure 3.11 shows the axial and swirl components of induced wash for the op-

timum single rotor compared to the Betz induced wash distributions at a thrust coefficient of $C_T = 0.004$. Note that the two solutions differ mostly near the blade root, with the largest differences seen in the swirl components of the induced wash.

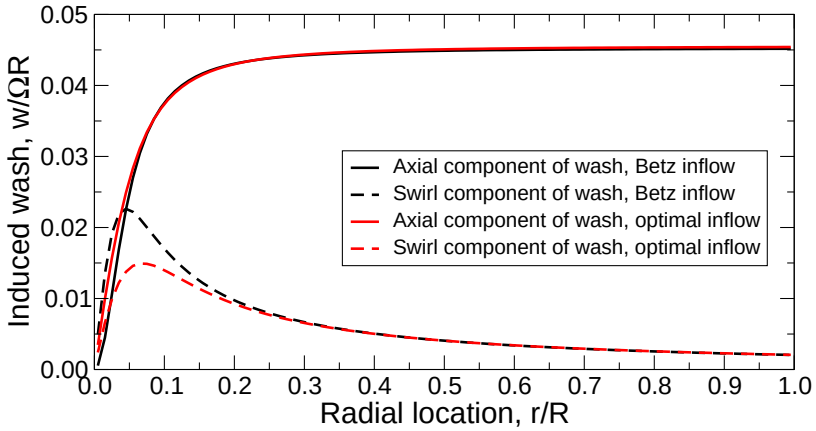

FIGURE 3.11: Axial and swirl components of the induced wash for the Betz inflow distribution compared to the optimal inflow distribution.

Figure 3.12 shows the induced figure of merit versus the coefficient of thrust for the optimal inflow distribution and the nearly optimal Betz inflow distribution. Note that Glauert presents a similar figure (Figure 88 of [63]), and that we are able to replicate these results with the optimization methodology presented here. The optimal inflow distribution has a slightly higher induced figure of merit than the Betz inflow with an improvement of only 0.6% in induced figure of merit at the very large thrust coefficient of $C_T = 0.05$.

In summary, when applied to a single rotor with swirl, the optimization method presented here recovers the optimal single rotor induced wash distribution including swirl described by Glauert [63]. This is a promising result, indicating that as we extend this analysis to a coaxial rotor system, our underlying treatment of the swirl velocities and resulting optimization for the two individual rotors are correct.

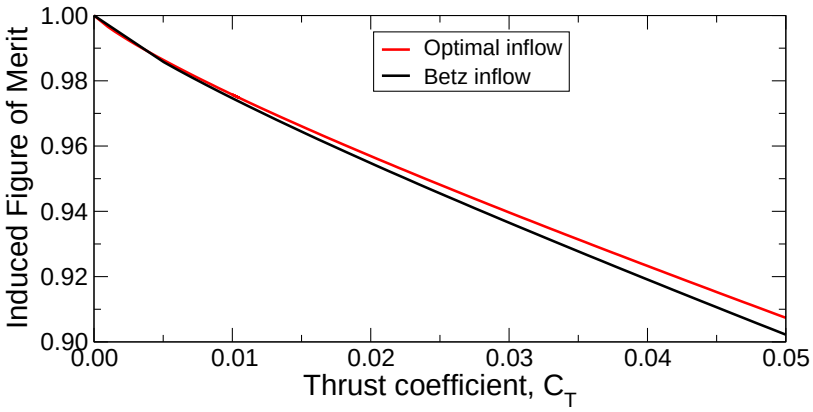

FIGURE 3.12: Figure of merit versus the coefficient of thrust for the Betz inflow distribution compared to the optimal inflow distribution.

3.3.3 Optimized Rotor Results – Coaxial Rotor

We now apply the optimization methodology to a coaxial rotor to determine the minimum loss coaxial rotor in hover. To quantify the effect of swirl on performance and on the optimal induced wash distribution and rotor design, we analyzed cases both with and without the swirl component of induced wash. In each instance, the total power loss from the two rotors is equal, i.e., the coaxial system is in torque balance. We include the Prandtl tip loss factor for each case and use the same mutual interference assumptions described in the previous section comparing BEMT results to Harrington's experimental results. For ease of comparison, we use the same airfoil characteristics, number of blades (two for each rotor), and vertical separation as the Harrington rotor 2.

Figure 3.13 shows the axial and swirl components of induced wash for the optimal coaxial rotor at a thrust coefficient of $C_T = 0.008$. For both the upper and lower rotors, the swirl case is very similar to the non-swirl case, with the exception of radial stations near the blade root, where the axial induced wash goes to zero at a value of $r/R = 0$. As expected, for the upper rotor, the non-swirl case has a uniform induced wash distribution, leading to the optimal performance, as originally stated

by Gessow [58].

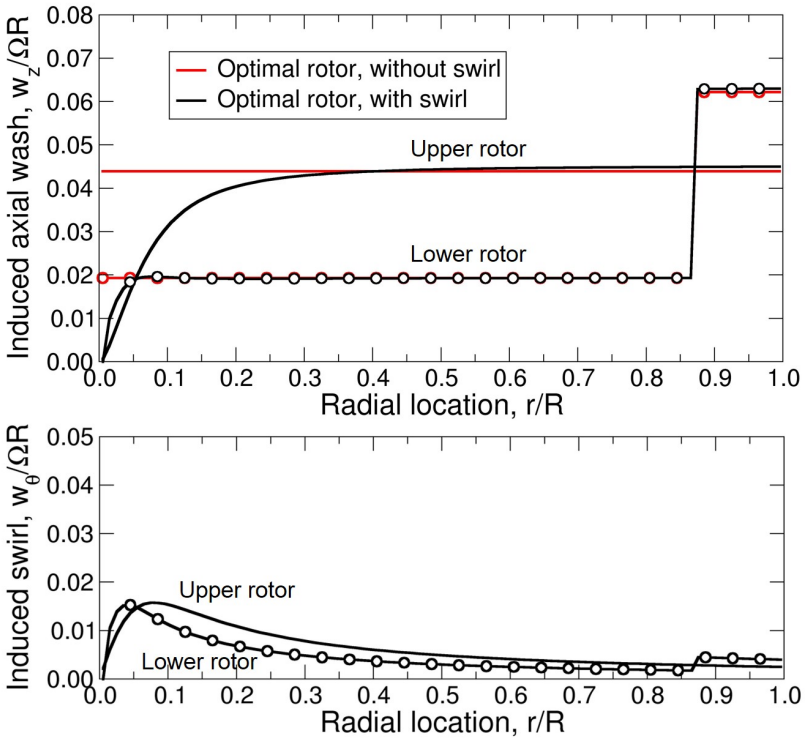

FIGURE 3.13: Top: Optimal radial distribution of axial induced wash on the upper and lower rotor at a thrust coefficient of $C_T = 0.008$, based on combined BEMT both with and without swirl. Bottom: Optimal distribution of the swirl component of induced wash for the swirl case.

Figure 3.14 shows the spanwise distributions of thrust, induced power loss, and profile power loss for the optimal rotors with and without swirl. The non-swirl optimal coaxial rotor generated using our approach is in agreement with the optimization methodology of Rand and Khromov [20] if applied using the same assumptions about mutual rotor interference and with tip losses neglected. Additionally, this rotor gives better performance than the Leishman and Ananthan [19] optimal hovering coaxial rotor, which uses a linear thrust distribution on each rotor.

For both the swirl and non-swirl cases, the inner portion of the lower rotor, which is operating in the contracted wake of the upper rotor, is significantly off-loaded, generating only a small fraction of the lower rotor's total thrust. The outer portion

of the lower rotor, which is not influenced by the upper rotor's wash (based on the mutual interference model used here), generates a much larger thrust and torque.

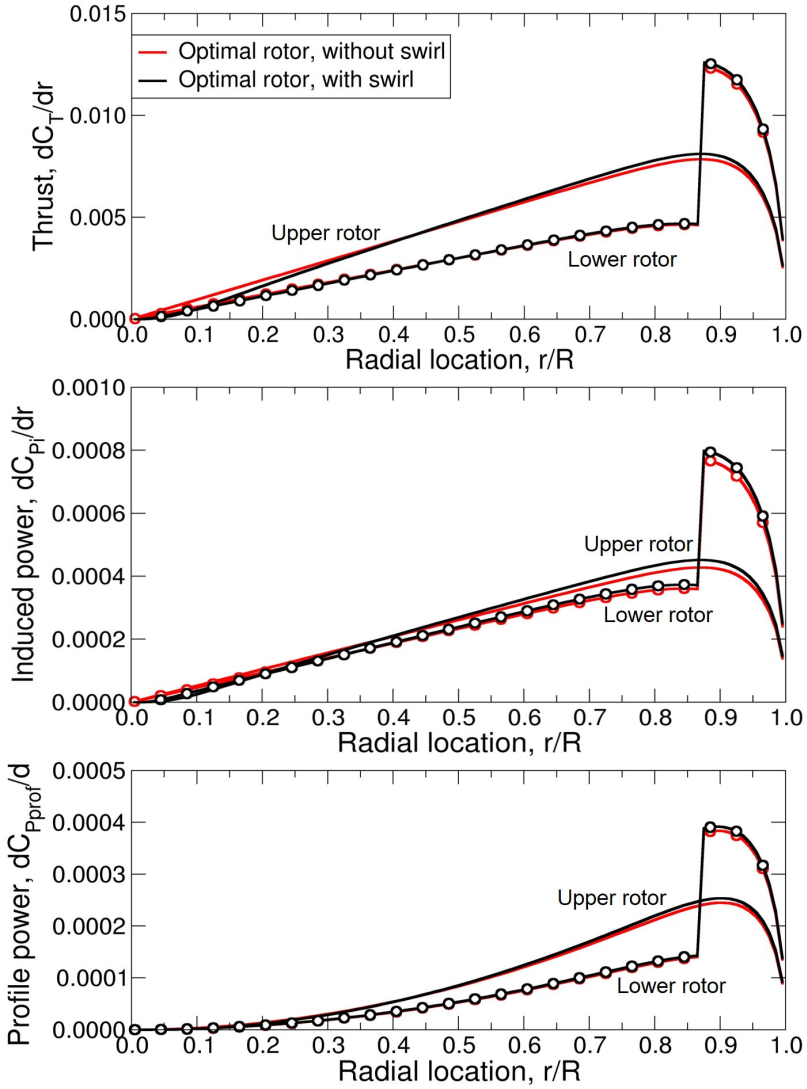

FIGURE 3.14: Top: Optimal radial thrust distribution for the swirl and non-swirl cases at a thrust coefficient of $C_T = 0.008$. Middle and bottom: Optimal induced and profile power distributions for the swirl and non-swirl rotors.

Figure 3.15 shows the radial twist and chord distributions for both the swirl and non-swirl optimal rotors. For the upper rotor, the non-swirl case shows the characteristic hyperbolic twist and chord distributions required to generate a uniform induced wash distribution, as modified by the presence of tip losses. The lower rotor

has a similar hyperbolic twist distribution with a breakpoint at $r_c/R \approx 0.87$, the radius outside of the contracted wake. The swirl case is nearly indistinguishable from the non-swirl case outboard of a radial position of $r/R = 0.3$. However, for values of $r/R < 0.3$, there are noticeable differences, as the chord of the swirl case upper and lower rotors go to zero at $r/R = 0$ while the chord of the non-swirl case upper and lower rotors continue to increase with decreasing r/R.

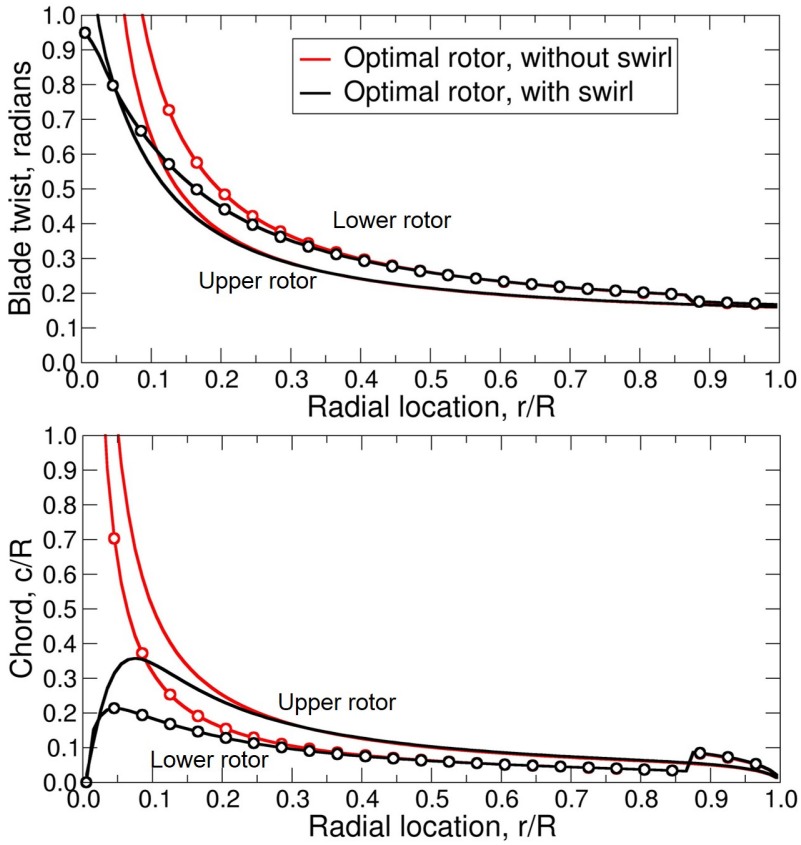

FIGURE 3.15: Top: Optimal twist distribution on the upper and lower rotor cases at a thrust coefficient of $C_T = 0.008$. Bottom: Optimal chord distribution for the swirl and non-swirl rotors.

Figure 3.16 shows an overhead view of the upper and lower rotor planforms for the optimal coaxial rotor including the swirl component of induced wash at $C_T = 0.008$. Along with Figure 3.15, we notice that the optimal coaxial rotor uses very different blade planforms and twist distributions on the upper and lower rotors, a

fact that is perhaps not surprising when considering the significantly different inflow distributions of the two rotors. The difference in inflows between the upper and lower rotor also results in the upper rotor generating 56% of the total system thrust to maintain a torque balanced condition.

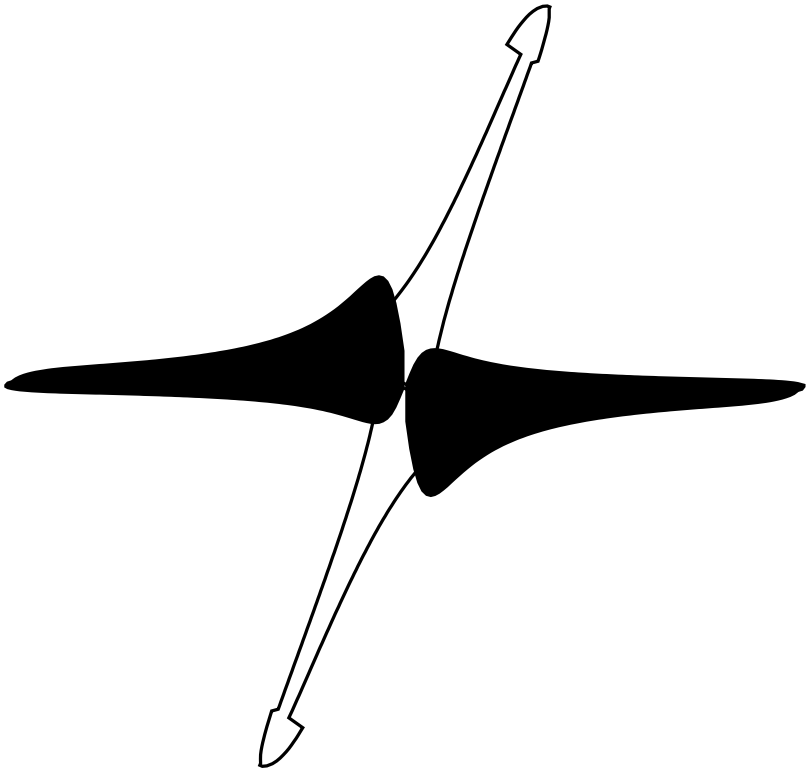

FIGURE 3.16: Overhead view of the optimal blade planform for a hovering coaxial rotor at $C_T = 0.008$, based on combined BEMT including swirl. The upper rotor planform is in solid black, the lower rotor is in white.

Figure 3.17 shows the figure of merit versus the thrust coefficient for the optimal coaxial rotor system (optimized at each thrust coefficient), both with and without the swirl component of induced wash. The swirl case has a lower figure of merit across all thrust coefficients. As expected, the difference in the non-swirl and swirl case figure of merit increases with increasing thrust coefficient, i.e., the presence of swirl has a larger impact at higher loadings. At the very high thrust coeffient of $C_T = 0.02$, the case accounting for swirl has a total figure of merit that is $\approx 3.5\%$

lower than the non-swirl case.

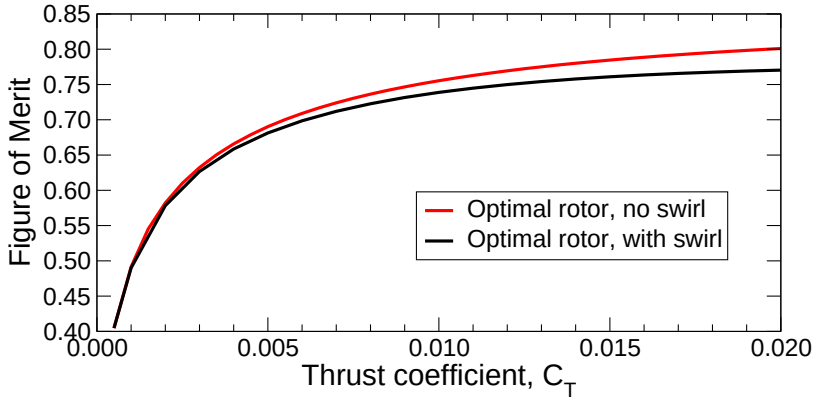

FIGURE 3.17: Figure of merit versus the coefficient of thrust for the optimal coaxial rotor using BEMT, both with and without swirl.

We now analyze the optimal rotors at off design points to determine how they perform over a range of thrust coefficients that may be encountered in an actual helicopter operation due to changes in vehicle weight, density, and altitude. We perform this analysis for two cases: the minimum induced power case, with only the twist optimized; and the minimum total power case, with the twist and chord optimized.

Figure 3.18 shows the computed figure of merit versus thrust coefficient for a coaxial rotor with the twist distribution optimized and a uniform chord at $C_T = 0.008$ and $C_T = 0.012$. Also shown for comparison is the performance with the twist distribution optimized at every thrust coefficient and the performance of the untwisted Harrington rotor 2. All optimized cases shown are optimized using BEMT with swirl. We see that the $C_T = 0.008$ and $C_T = 0.012$ rotors have a figure of merit very close to the rotors optimized anew at each thrust coefficient, even at off-design points. Additionally, these optimized rotors far outpeform the untwisted Harrington 2 rotor, with a figure of merit 9% higher than the baseline Harrington rotor 2 at $C_T = 0.008$.

Figure 3.19 shows the figure of merit versus thrust coefficient for a coaxial rotor

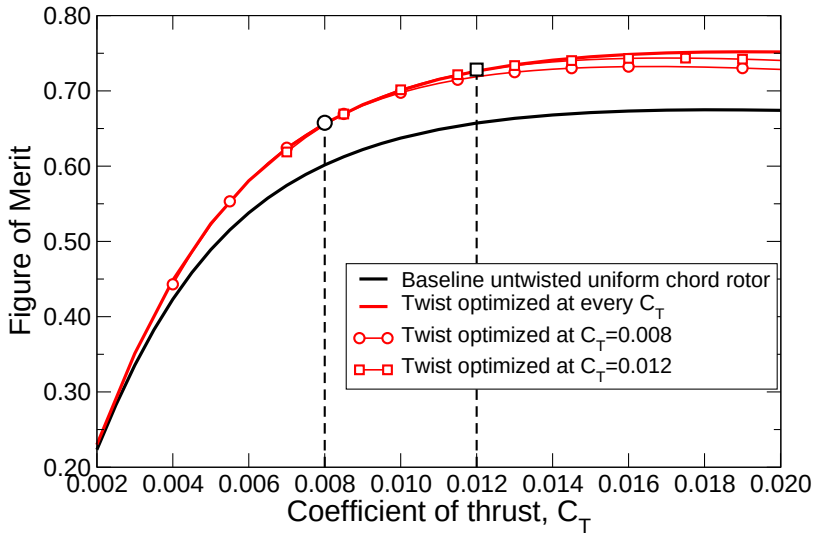

FIGURE 3.18: Figure of merit versus the coefficient of thrust for the optimal $C_T = 0.008$ and $C_T = 0.012$ hovering coaxial rotors including swirl. Only the twist has been optimized in each case i.e., only induced powers are minimized.

with twist and chord distribution (minimum total power) optimized at $C_T = 0.008$ and $C_T = 0.012$. Also shown is the figure of merit with the twist and chord distribution minimized at every thrust coefficient, and the figure of merit of the untwisted Harrington rotor 2 baseline. Also plotted is the twist optimized case at every thrust coefficient, to show the performance improvement available using a non-uniform chord distribution. At off design points, the optimized twist and chord rotors have significantly degraded performance, in contrast to the twist only optimization. However, at their respective design points, the optimized twist and chord rotors far outperform the twist only optimization and the baseline untwisted Harrington rotor, with a figure of merit 20% higher than the baseline Harrington rotor 2 at $C_T = 0.008$.

As previously observed, the optimal hovering coaxial rotor system has significantly different chord and twist distributions on the upper and lower rotors. Such a design, while optimal in hover, may not perform as well in forward flight. To quantify the benefit of using different blade designs on the upper and lower rotors, we

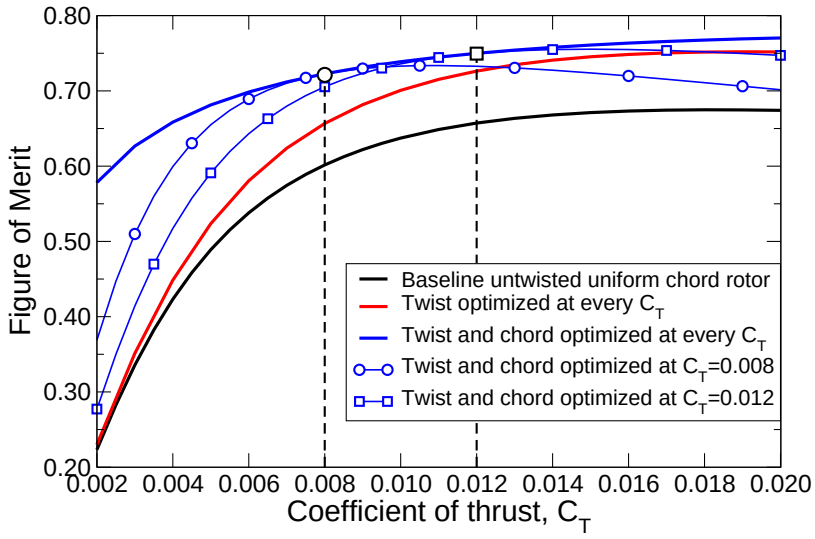

FIGURE 3.19: Figure of merit versus the coefficient of thrust for optimal $C_T = 0.008$ and $C_T = 0.012$ hovering coaxial rotors including swirl. Both the chord and twist have been optimized, i.e., the sum of induced and profile power losses are minimized.

compared the performance of the optimal twist and chord rotor to a rotor using the optimal upper blade design on both rotors (i.e., a rotor designed without accounting for the effect of the upper rotor's wake on the lower rotor's inflow). Figure 3.20 shows the figure of merit versus the thrust coefficient for these two cases. We see that using different blade designs on the upper and lower rotors provides a larger benefit in terms of figure of merit at higher thrust coefficients. While at $C_T = 0.002$, there is a very small difference in performance between the rotor with equal blades and the rotor with different (optimal) upper and lower blades, at $C_T = 0.016$ the optimal rotor provides a figure of merit 1% higher than the rotor with equal blades, a noticable but relatively small improvement. Therefore, while using different blade twist and chord distributions on the upper and lower rotors is optimal, using the upper rotor twist and chord distributions on both rotors does not dramatically reduce hovering performance.

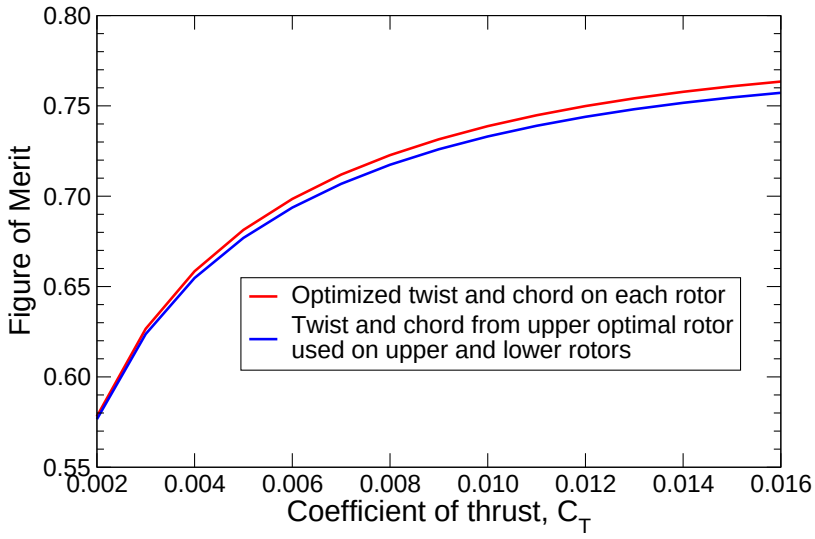

FIGURE 3.20: Figure of merit versus the coefficient of thrust for the optimal hovering coaxial rotor including swirl at each thrust coefficient, compared to the performance of a coaxial rotor using the optimal upper rotor blade and twist for both the upper and lower rotor.

3.4 Conclusions

In this chapter, we have presented a method for computing the optimal coaxial rotor design in hover using Blade Element Momentum Theory including the effect of the swirl component of induced wash. The method determines the induced wash distribution that will minimize induced power, and the twist and chord distributions that minimize profile power losses. The method models the effect of the contracted axial and swirl washes acting on the inner portion of the lower rotor, and approximates the lower rotor's effect on the upper rotor as a uniform axial downwash dependent on the average induced wash of the lower rotor and the vertical separation of the rotors. Tip effects accounting for a finite number of blades are included using the Prandtl tip correction factor. Profile losses and their effects on power and thrust are included using airfoil drag polars. We applied this optimization approach to a coaxial rotor similar in design to the Harrington rotor 2. Based on the work presented in this paper, we make the following conclusions.

1. Contrary to prior assertions in the literature (References [19] and [21]) and in agreement with a similar analysis performed in [20], the minimum induced loss coaxial hovering rotor (as determined by BEMT) does not have a uniform disk loading, i.e., linear thrust distribution, on both the upper and lower rotors. Rather, the minimum induced loss coaxial rotor uses a significantly lower, and in some cases negative, disk loading on the inner portion of the lower rotor. The outer portion of the lower rotor, operating outside of the contracted wake of the upper rotor, then generates a much larger thrust then the uniform disk loading case.

2. The optimization methodology including swirl recovers the Glauert optimal induced wash distribution for a single rotor, achieving a higher induced figure of merit than the Betz inflow distribution.

3. The optimal coaxial rotors with and without swirl are nearly identical at radial stations outboard of $r/R = 0.3$. At values of $r/R < 0.3$, the rotors optimized accounting for swirl have signficantly different optimal twist and chord distributions than the non-swirl case.

4. As expected, accounting for the effects of swirl has a larger effect on performance at higher thrust coefficients. The swirl case has an optimal figure of merit 3.5% lower than the no swirl case at the very high thrust coefficient of $C_T = 0.02$.

5. At the typical disk loadings seen on helicopters, the effect of swirl on rotor design and performance predictions within the framework of combined Blade Element Momentum Theory is relatively small. Other model refinements, such as more detailed wake modeling and improved mutual interference models, may have a larger impact on optimal rotor design and performance predictions than

the inclusion of the swirl component of induced velocity.

6. Optimizing the twist alone to minimize the induced power of the coaxial rotor studied here increases the figure of merit by 9% compared to a baseline untwisted rotor at a thrust coefficient of $C_T = 0.008$. Optimizing both the twist and chord increases the figure of merit by 20% over the baseline rotor at $C_T = 0.008$.

7. The optimal coaxial hovering rotor has a significantly different twist and chord distribution on the upper and lower rotors, resulting from the different inflow distributions acting on each rotor. However, using the optimal upper rotor blade design on both rotors leads to a relatively small decrease in performance, indicating that near optimal hover performance can be achieved with upper and lower rotors using the same blade design.

4

Axisymmetric Potential Flow Model of the Actuator Disk

In Chapter 3, we developed a method to determine the optimal coaxial rotor design in hover. This optimization computed the induced wash distribution and radial twist and chord distributions that yield the optimal induced inflow while minimizing profile losses. To model the mutual interference of the two rotors within this optimization, we used a simple influence coefficient model originally developed by McAlister et al. [49]. To approximate the influence of the upper rotor on the lower rotor, we used this model to determine the contraction of the upper rotor's wake when it reaches the lower rotor. We then scaled and mapped the induced axial and swirl velocities of the upper rotor onto the portion of the lower rotor operating in this contracted slipstream. In accordance with the same model, we approximated the effect of the lower rotor on the upper rotor as a uniform downwash that is a function of the vertical separation of the rotors and the average induced inflow of the lower rotor. For the optimization, we assumed that the portion of the lower rotor operating outside of the upper rotor's contracted slipstream has no inflow.

While this simple model compares well to experimental data (cf. Juhasz et al. [59]

and Figure 3.10), in this chapter we seek to build a more refined model of the wake of a conventional or coaxial rotor in hover or axial flight. We approximate the rotor (or rotors) as actuator disks and the wake as contracting cylindrical vortex sheets modeled using discrete vortex rings. We assume the system is steady in time and axisymmetric, requiring us to only look at a single azimuthal slice of the flow field to determine the shape of the wake and the induced velocity throughout the entire flowfield. We apply this axisymmetric potential flow model to the following cases:

- A uniformly loaded actuator disk in hover, climb, and descent, in order to gain insight into the geometry of the wake and the resulting induced inflow at the disk.
- An actuator disk with piecewise linear circulation distributions, to determine the effect of changes in bound circulation on the disk on the wake geometry.
- Coaxial actuator disks in hover of varying vertical separation, to quantify the mutual interference effects of the two disk system and to validate the predictions used in the Chapter 3 optimization. We investigate both torque-balanced and non torque-balanced cases.

4.1 Background on Actuator Disk Wake Modeling

Momentum theory provides a simple but powerful tool for predicting the performance of propellers, windmills, or rotors. First developed by Rankine [64] and extended by Froude [65], momentum theory models the rotor as a circular surface of zero thickness, referred to as an actuator disk, through which a pressure difference exists. By performing an axial momentum balance on the resulting system, Froude derived a simple expression stating that the velocity at the actuator disk is the average of the flow velocities far upstream and far downstream of the rotor. Figure 4.1 shows the notional actuator disk in climb, with V_c denoting climb velocity and V_i denoting the

induced velocity at the actuator disk. The thrust done by the actuator disk is simply the product of the mass flow through the disk and this induced velocity ($T = \dot{m}V_i$). Additionally, there is an induced power loss as a result of a kinetic energy increase in the wake, which is equal to the product of the thrust of the disk and the induced velocity at the disk ($P_i = TV_i$) .

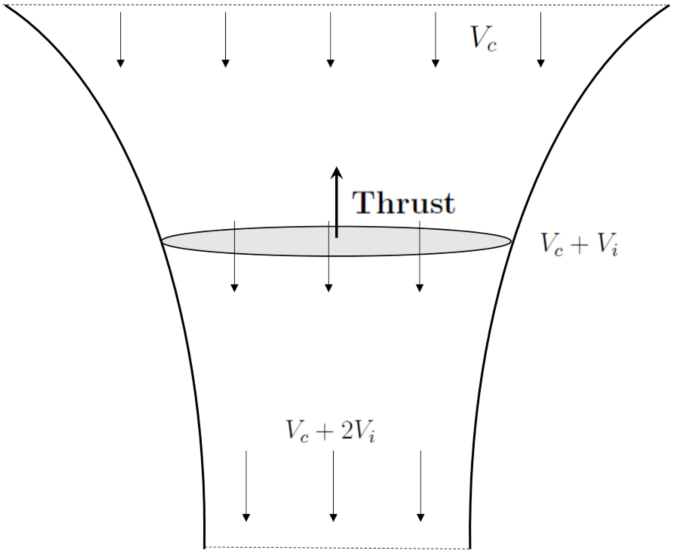

FIGURE 4.1: The flow through an actuator disk, as depicted in most discussions of the topic.

Due to its simplicity and relative accuracy, momentum theory is an initial building block in many complex models of rotary wing devices. However, momentum theory itself gives no detailed description of the induced velocity field; rather, in its most basic form it assumes the induced velocity only varies in the axial direction, i.e., the induced velocity is constant at the disk and at any axial slice in the downstream wake. Additionally, while momentum theory predicts the final wake contraction via conservation of mass as

$$\frac{A}{A_c} = \frac{V_c + V_i}{V_c + 2V_i} \tag{4.1}$$

it gives no information about the axial distance required to achieve this final contraction, or about the level of wake contraction reached at some given axial distance. Knowledge of the axial rate of contraction is of particular interest when analyzing closely spaced coaxial rotors, where it is possible that the upper rotor's wake has not contracted to its final far field value before impinging upon the lower rotor. As a result, developing a model that can predict the rate of this contraction, as well as a more detailed knowledge of the induced velocity distributions at the disk and elsewhere in the wake, is of great interest.

Many researchers have investigated the flow field induced by an actuator disk. Betz and Prandtl [62] used vortex theory to compute the optimal induced velocity profile at the disk for a propeller with an infinite number of blades in axial flight. They assumed the rotor was lightly loaded, and thus assumed that the trailing vortices formed regular helices, an assumption that is equivalent to neglecting the contraction of the wake. Goldstein [39] extended this work to determine the optimal induced velocity of a lightly loaded finite bladed propeller. Hough and Ordway [66] used a vortex representation of the helical trailing wake of a lightly loaded propeller similar to that of Goldstein, and computed the induced velocities at any point in the field using the Biot-Savart law. The authors Fourier analyzed these velocity fields in the circumferential direction, and then considered the zeroth harmonic, i.e., the mean component. Using this approach, the authors derived integral expressions that could be solved to determine the mean axial and radial velocities induced by a lightly loaded propeller with an arbitrary circulation distribution and blade number. The authors also proved that the steady component of the induced velocities for a finite bladed propeller are equivalent to the actuator disk (infinite blade) result.

Similarly, Conway [67] used an analytical approach to solve for the induced velocities of a propeller actuator disk of arbitrary radial loading. Conway was able to compute the wake contraction as a function of the axial coordinate for a "lin-

earized" actuator disk, meaning the induced flow field is linearized about the free stream velocity. Conway noted that as a result of this linearization, the theory is more accurate for lower thrust coefficients, i.e., flight conditions where the ratio of climb velocity to induced wash at the disk V_c/V_i is large. Conway [68] extended this approach to develop a semi-analytical model that accurately analyzes a nonlinear actuator disk of arbitrary loading while taking the slipstream contraction fully into account. Conway's [68] results give wake contraction and velocity profiles for a variety of heavily loaded propellers as well as energy extracting windmills; Conway does not, however, extend his model to the zero free stream (i.e., hover) case. Greenberg and Powers [48] developed an iterative approach to determining the wake geometry and vorticity distribution on an actuator disk, and applied the model to the hovering actuator disk with both uniform and radially varying loading. Cox [69] used a discrete vortex ring model of the wake sheet to model the wake of a propeller in axial flight in order to investigate the effect of a nonuniform free stream and the influence of a wind tunnel wall on the flow field.

One problem with the seemingly simple actuator disk model is the way in which the vortex sheet is terminated at the edge of the disk. In the simplest vortex models, the wake is represented as a contracting circular vortex sheet located at the boundary of the slipstream, as described by Johnson [4]. However, the sudden termination of this vortex sheet at the rim of disk can lead to problems or inconsistencies in the wake and its resulting flow field. In a 1915 paper, Lanchester [70] observed that momentum theory was inconsistent at the edges of the disk, as the infinitely thin actuator disk cannot maintain a pressure jump at the edge without a singularity. Lanchester predicted that as a result of the neglect of this singularity, the classical momentum theory would underestimate the induced velocity at the disk. Van Kuik [71] attempts to rectify this inconsistency by postulating that there exists a discrete vortex at the edge of the actuator disk. This vortex is bound to the edge of the disk, acting as

the leading edge of the vortex sheet. Because of the presence of this vortex, the streamlines near the edge of the disk are spirals centered around the edge of the disk. Additionally, in Van Kuik's formulation of the actuator disk, the bound edge vortex creates an edge force that generates thrust that is not accounted for in the axial momentum balance.

Pullin [72] considered the problem of the roll up of an initially flat vortex sheet, which is somewhat analagous to the situation present at the edge of the actuator disk. A singularity exists at the edge of this sheet, which is resolved through an unsteady, spiral-like roll up. Pullin was able to numerically compute the large scale structure of this unsteady roll up, which forms a time-varying spiral like structure.

In his work on determining the velocities induced by an actuator disk, Conway [68] addresses this apparent inconsistency with a terminating vortex sheet and the resulting roll up and/or passing of streamlines through the disk. The author observes that while a numerical scheme could be constructed to compute the details of the roll up, doing so would undermine the simplicity of the actuator disk model. Additionally, Conway notes that models that use multiple vortex tubes, such as that of Greenberg and Powers [48], also encounter the same problem, as each of the individual tubes would roll up at its intersection with the disk.

Schmidt and Sparenberg [46] compute a numerical solution for an actuator disk of infinite radius (essentially an actuator strip) and zero axial velocity. The authors found that the vortex sheet exhibits a spiraling behavior near the edge of the disk, and were able to apply this spiral structure to a uniformly loaded actuator disk of finite radius. They found that streamlines pass through the disk more than once at the disk's edge as a result of the spiraling vortex sheet.

In 2005, Spalart [45] revisited the actuator disk, making several interesting observations. As Conway, Lanchester, Van Kuik and others had previously observed, in the classical model a vortex sheet ends abruptly at the disk, which would result

in an infinite velocity; Spalart therefore rules out an abrupt termination of the sheet as a viable solution. Instead, he postulates that in hover "it is most likely that the exact shape [of the vortex sheet], for the infinitely thin sharp-edged disk, is a volute wound around the disk's edge. The two dimensional Euler equations admit an exact solution with a vortex sheet of uniform density placed on a 45 degree spiral." He notes, however, that such a solution, either analytical or numerical, does not exist in the literature (although such a solution was in fact found previously by Schmidt and Sparenberg [46]). In axial flight, Spalart states that the spiral wake structure would hold, although the extent of the spiral would shrink. The author supports this hypothesis by showing the streamlines and vorticity contours of an actuator disk in hover computed via a numerical solution to the incompressible Navier-Stokes equation. These plots demonstrate both the upflow through the disk near its edge and a smeared spiral shape in the vorticity contours. Additionally, Splart observes that the induced velocity at the actuator disk is far from uniform (and is completely reversed at the edge), an observation that he notes conflicts with both common beliefs and one-dimensional arguments. As a result, the conventional momentum balance schematic shown in Figure 4.1 is in fact inaccurate, particularly in hover, as flow enters the actuator disk not just from above but also from all sides, and because the uniform flow shown at the disk is far from uniform and is in some cases even reversed. Despite the apparent contradiction and inconsistencies due to this non-uniform and sometimes reversed flow at the disk, Spalart performs a more rigorous control volume analysis that reinforces the classical result for induced power without making use of the assumption of uniform induced velocity at the disk. As a result, the classical momentum theory results are unchanged, despite the inaccurate assumptions (e.g., uniform flow at the disk) that some authors use in their derivation.

In this chapter, we construct a steady axisymmetric potential flow model of the trailing wake of an actuator disk. To determine the geometry of the vortex sheet, we

impose a boundary condition that the vortex sheet must be aligned with streamlines of the flow field at all points, i.e., that there is no flow through the sheet. We use Newton iteration to determine the shape of the vortex sheet that satisfies this boundary condition. We represent the continuous cylindrical vortex sheet as a system of discrete vortex rings. For a uniformly loaded actuator disk in hover, we find that the wake at the edge of the actuator disk assumes the shape of a 45 degree logarithmic spiral, as hypothesized by Spalart [45]. Also in accordance with the findings of Spalart and the analyis of Schmidt and Sparenberg [46], we find that the induced flow distribution is far from uniform over the disk, and is in fact reversed near the edge of the disk. As other researchers including Spalart have noted, the notional actuator disk model shown in Figure 4.1, is inaccurate, particularly at low velocities, where the actuator disk draws in flow not just from above the disk but also from areas outside of the streamtube and below the disk. We examine the shape of the wake, including its spiral edge structure, at a range of axial velocities, including negative axial velocities with the rotor acting as a windmill. We also investigate the effect on wake shape and induced velocities of non-uniform circulation distributions by using multiple vortex sheets to model piecewise constant circulation distributions. We use the same wake modeling approach to investigate coaxial actuator disks, and examine the effect of vertical separation on the resulting flow field and rotor performance. Finally, we compare the mutual interference of the coaxial rotor predicted in our wake model to that computed using the simple influence coefficient model described in McAlister et al. [49] and used in the Chapter 3 optimization, and find that despite the large discrepancy in complexity, the two models produce reasonably similar results.

4.2 Technical Approach to Wake Modeling

We seek to model the vortex system of an actuator disk, thereby allowing us to compute the velocities induced by this vortex system at any point in the flow field. As

described by Conway in Reference [67], for a uniformly loaded actuator disk, there are four vortex distributions that induce perturbations to the mean flow. The first is a contracting vortex tube consisting of discretized ring vortices, shown in Figure 4.2. These ring vortices are trailed from the edge of the actuator disk and extend to downstream infinity. This distribution is itself a vorticity conserving system and is solely responsible for all axial and radial induced velocities and for the contraction of the wake itself. In addition to the ring vortex system, there are three other vortex systems that combine to form their own vorticity conserving system: a constant strength hub vortex at the center of the disk extending to downstream infinity, a distribution of vorticity on the actuator disk itself, extending radially, and a distribution of vorticity on the streamtube's surface that is normal to the ring vortices and equal in strength to the hub vortex. The only non-zero component of velocity they induce is in the circumferential direction, i.e., the swirl component of induced velocity. As we demonstrated in Chapter 3, the swirl component of induced velocity has a relatively small effect on rotor performance and design. As a result, we model only the axial and radial induced velocity fields and wake contraction, which can be accomplished by modeling exclusively the ring vortex system.

4.2.1 Modeling the Ring Vortices

We compute the velocity field induced at a point in space P by a vortex line of differential length $\mathbf{dl}$ using the Biot-Savart law

$$\mathbf{V} = \frac{\Gamma}{-4\pi} \int_l \frac{\mathbf{r} \times \mathbf{dl}}{\|\mathbf{D}\|^3} \tag{4.2}$$

where $\mathbf{D}$ is a vector extending from P to the line segment $\mathbf{dl}$. Because of the axial symmetry of the problem, the induced flow field will include only axial and radial velocities. Following the approach of Cox in Reference [69], we can integrate Eq. (4.2) around the circumference of a unit strength vortex ring to yield expressions for the

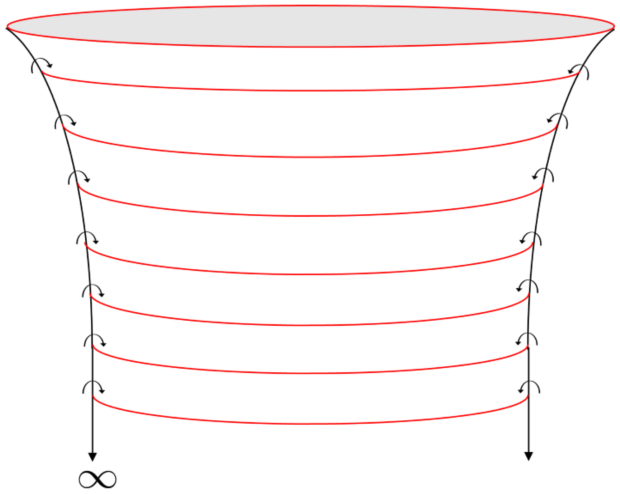

FIGURE 4.2: The vortex ring system of a uniformly loaded actuator disk.

axial and radial velocities induced at some P, with coordinates denoted x_P, z_P. We denote the x and y positions of the vortex ring's intersection with the meridional plane as x_R, z_R, and denote the circumferential coordinate of the ring as ϕ_R, giving

$$u(x_P, z_P) = \int_{\phi=0}^{\phi=2\pi} \frac{(z_P - z_R)\cos(\phi_R) x_R d\phi_R}{4\pi \|\mathbf{D}\|^3} \tag{4.3}$$

$$w(x_P, z_P) = \int_{\phi=0}^{\phi=2\pi} \frac{[x_R - x_P \cos(\phi_R)] x_R d\phi_R}{4\pi \|\mathbf{D}\|^3} \tag{4.4}$$

where $u(x_P, z_P)$ and $w(x_P, z_P)$ are the induced radial and axial velocities, respectively, due to a unit strength vortex ring.

4.2.2 Determining the Contraction of the Wake

In our steady state wake model, we impose a boundary condition that the vortex sheet, as represented by discrete vortex rings, is aligned with the streamlines at all points. This no-through-flow boundary condition allows us to define the position of the vortex sheet. Of course, the problem can be challenging to solve, as the flow field is not known *a priori*, but is rather a function of the mean flow and the velocity induced by the vortex sheet itself, which in turn is a function of its position.

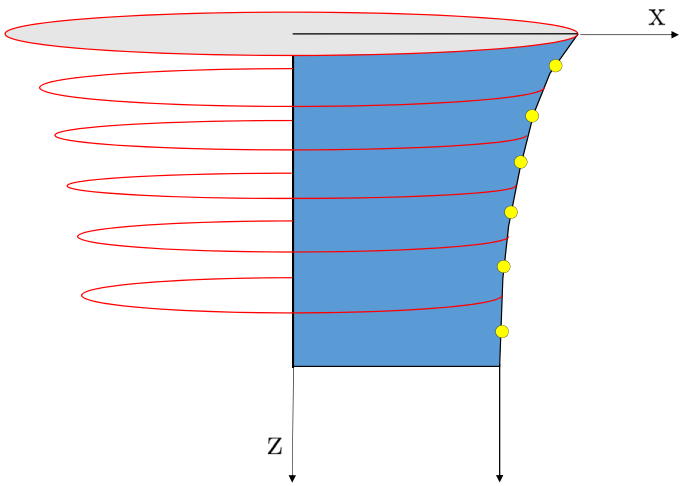

FIGURE 4.3: An azimuthal cut of the axisymmetric vortex ring model, with collocation points shown as yellow circles.

Because the problem is axisymmetric, we need only to satisfy the no through flow boundary condition at a single azimuthal slice of the disk. By defining the radial and axial position of each vortex ring at this single azimuthal location, we can fully define the wake. Within this azimuthal slice, we place collocation points equidistant between each successive vortex ring. Figure 4.3 shows a azimuthal cut of the vortex ring model with the collocation points shown in yellow.

We compute the induced velocity at a given point in space by summing the influence of every vortex ring in the model on that point. To efficiently model the semi-infinite wake, which extends indefinitely in the positive z direction, we compute the sending influence of vortex rings until their influence on the contracting portion of the wake is sufficiently small. At every spatial location, the total flow velocity is then comprised of the sum of this induced velocity and the mean flow due to axial motion of the disk. In hover, the mean flow is of course zero. In axial flight, however, the flow can be in the positive z direction (ascending flight) or the negative z direction (descending flight). To determine if the no-through-flow

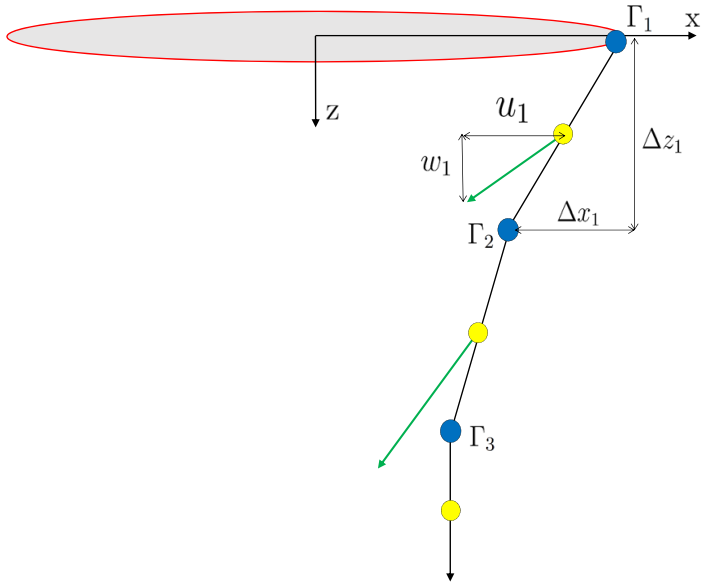

FIGURE 4.4: An azimuthal cut of the axisymmetric vortex ring model, with collocation points shown as yellow circles, velocity vectors acting at the collocation points as green arrows, and the intersection of the vortex rings with the selected azimuthal plane as blue circles.

boundary condition is satisfied, we compute the induced and total flow velocity at each collocation point. We denote the x and z components of flow velocity at a given collocation point i as u_i and w_i, respectively. Because the ring vortex system does not induce any circumferential velocities, in a given azimuthal plane, the y component of velocity is always zero.

We then need to define the slope of the sheet at each collocation point to assess the flow tangency boundary condition. To illustrate this process, Figure 4.4 shows a simplified schematic of a wake model consisting of only 3 vortex rings. Note that the first ring is placed at the edge of the disk. The first collocation point is then located midway between the first and second vortex rings. The straight line segment connecting the two neighboring ring vortices then defines the slope of the vortex sheet on which a given collocation point lies. As illustrated here, the first segment of the vortex sheet has slope $\Delta z_1/\Delta x_1$.

We can express the boundary condition at the i^{th} collocation point as

$$\frac{\Delta z_i}{\Delta x_i} = \frac{w_i}{u_i} \tag{4.5}$$

where w_i is the sum of the axial induced and climb velocity, u_i is the component of induced velocity in the radial direction. Δx_i and Δz_i are defined by

$$\Delta x_i = x_{i+1} - x_i \tag{4.6}$$

$$\Delta z_i = z_{i+1} - z_i \tag{4.7}$$

4.2.3 Newton Iteration to Determine Wake Position

Satisfying the no through flow condition is complicated slightly by the fact that the induced flow field changes with a change in any vortex ring's position, making the no-through-flow condition nonlinear. We use an iterative approach based on Newton iteration to determine the correct vortex ring positioning.

We use the no-through-flow boundary condition in Eq. (4.5) to construct a vector of residuals $\mathbf{R}$ that we wish to set to zero. The i^{th} entry of $\mathbf{R}$ is defined by

$$R_i(x_i, z_i) = \Delta x_i w_i - \Delta z_i u_i \tag{4.8}$$

We have reached a wake shape that satisfies the no through flow boundary condition when all of the entries of $\mathbf{R}$ are equal to zero, i.e., when

$$\mathbf{R}(\mathbf{x}, \mathbf{z}) = 0 \tag{4.9}$$

In practice, we can parametrize the positions of the vortex rings in a variety of ways. One way is to define the x and z positions of each vortex ring, with the first vortex ring fixed at the rim of the actuator disk. A more efficient and robust approach is to define an angle θ_i that represents the angle between the i^{th} segment of the vortex sheet and the positive x axis. We then define ds_i as the distance between vortex ring i and ring $i+1$, as illustrated in Figure 4.5. Note that this value does not have to

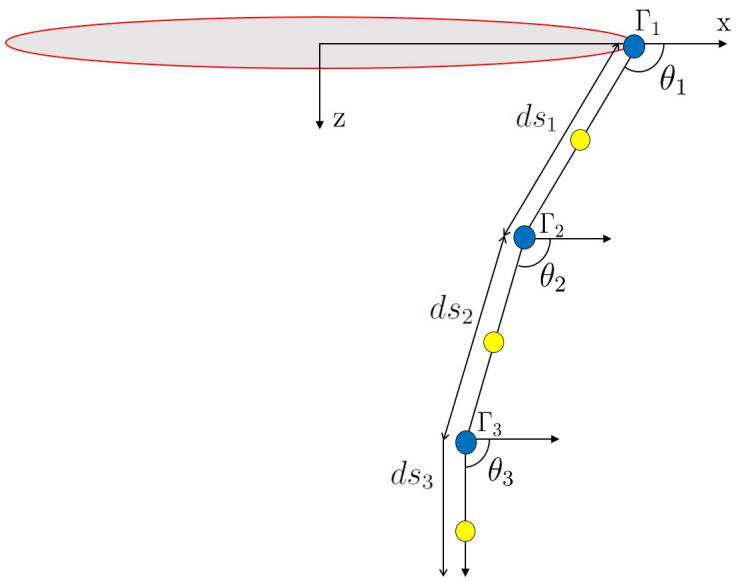

FIGURE 4.5: Schematic showing the definition of the angle θ_i and length ds_i that fully define the position of each vortex ring.

be uniform along the wake (i.e., the vortex rings can be non-uniformly spaced), but it is fixed from iteration to iteration. Therefore, we can fully define the shape of the wake using the angle θ_i at each vortex ring.

We use Newton iteration to determine the entries of the vector $\boldsymbol{\theta}$ such that

$$\mathbf{R}(\boldsymbol{\theta}) = 0 \tag{4.10}$$

At each iteration k, we update the vector of angles $\boldsymbol{\theta}$ using

$$\boldsymbol{\theta}^{k+1} = \boldsymbol{\theta}^k - \mathbf{R}(\boldsymbol{\theta}^k)_\theta^{-1}\mathbf{R}(\boldsymbol{\theta}^k) \tag{4.11}$$

where $\mathbf{R}(\boldsymbol{\theta}_k)_\theta$ is the Jacobian of the vector function $\mathbf{R}$ with respect to $\boldsymbol{\theta}$. It is difficult to compute the Jacobian of $\mathbf{R}(\boldsymbol{\theta})$ analytically. Instead, we use automatic differentiated code generated by the compiler Tapenade [73] to compute the entries of the Jacobian $\mathbf{R}(\boldsymbol{\theta}^k)_\theta$.

4.2.4 Scaling of the Circulation

To conserve the vorticity of the system, we must scale the circulation strength of the discrete vortex rings as they change size (diameter) and position throughout the iteration. First, it is often advantageous to use a non-uniform spacing of the vortex rings, meaning that the value of ds between each successive vortex ring is not constant. Typically, a more dense ring spacing near the disk is necessary to capture the details of the wake structure, while in the far field, a larger spacing is sufficient. Of course, the discrete vortex rings actually represent some section of the continuous vortex sheet along its length; therefore having a larger spacing means a given vortex ring is representing a larger portion of the tube and thus needs to have a larger magnitude circulation. To account for this, we we scale the ring's circulation strengths by their spacing ds relative to some arbitrary reference length ds_{ref} with a known circulation Γ_{ref}, i.e.,

$$\Gamma_i = \Gamma_{\text{ref}} \frac{ds_i}{ds_{\text{ref}}} \tag{4.12}$$

In addition to scaling by the length of the wake each ring represents, we must consider the change in vortex density within this region. Each vortex ring represents a continuous sheet of vorticity that is convecting along the streamtube at the wake transport velocity. The vortex density of the sheet will change with the transport velocity of the sheet itself - as the ring speeds up, a discrete section enclosing a set amount of vorticity will grow in length, with a resulting decrease in its vortex density. As a result, we must scale the strength of each vortex ring to account for this varying vortex density such that the quantity $\gamma_i V_i$ is constant throughout the sheet, where V_i is the component of total velocity parallel to a vortex segment ds_i. To account for this, we define the circulation for some reference ring with a known

velocity V_{ref} and scale the circulation of each vortex ring using

$$\Gamma_i = \Gamma_{\text{ref}} \frac{V_{\text{ref}}}{V_i} \tag{4.13}$$

An equivalent way to perform the convective velocity scaling is to define some arbitrary time step and stretch or compress the vortex filaments as they traverse the sheet in order to conserve vorticity. Said another way, we can set our vortex ring spacing **ds** to enclose some given amount of vorticity, and then increase or decrease the spacing as needed to ensure our length ds is always capturing this same amount of vorticity. This method was also used and was shown to be equivalent to a fixed wake spacing that instead scales by velocity. However, it is numerically advantageous to define a fixed ring spacing that does not change throughout the iteration, so we instead scale by both this initial spacing (Eq. (4.12) and the convective velocity of each segment (Eq. (4.13).

In total, we scale the circulation strength of each vortex ring by these two ratios, all relative to some reference ring. In practice, we often fix the circulation strength of a ring in the far wake and use this value as Γ_{ref}. The total scaling for each ring is then

$$\Gamma_i = \Gamma_{\text{ref}} \frac{ds_i}{ds_{\text{ref}}} \frac{V_{\text{ref}}}{V_i} \tag{4.14}$$

4.2.5 Total Iteration Algorithm

We update the circulation strength of each vortex ring using Eq. (4.14) after each Newton iteration step. The Jacobian $\mathbf{R}(\boldsymbol{\theta})_\theta$ does not account for the change in circulation that will occur with a change in wake shape and convection velocity. While we could formulate a computation of the Jacobian that accounts for these secondary effects, it is sufficient to simply update the circulation after each Newton step. Although this leads to a decrease in the accuracy of the Jacobian and the resulting

Newton step, the changes in circulation from one iteration to the next are generally small and become progressively smaller as the iteration reaches convergence, i.e., as $\mathbf{R}(\boldsymbol{\theta}) \to 0$. Therefore, neglecting the change in circulation in the computation of the Jacobian has a negligible impact on the ability of the Newton iteration to locate a solution.

4.2.6 Multiple Vortex Sheets

Analyzing a system with multiple vortex sheets, such as in the case of coaxial actuator disks or a single actuator disk that does not have a uniform bound circulation and trails additional vortex sheets at locations inboard of the edge of the disk, uses fundamentally the same algorithm and wake definition described previously. Multiple vortex sheets are discretized into rings, and the positions of each of these rings that satisfy the no-through-flow boundary condition are still determined using Newton iteration. The induced velocity at a given collocation point is dependent on all vortex sheets. Additional care must be taken to ensure that the separate vortex sheets do not cross, which results in large induced velocities, poorly conditioned Jacobians, and chaotic behavior leading to divergence. In cases such as these (e.g., a very close radial spacing), a significant under-relaxation factor is used to prevent crossing of the vortex sheets. Additionally, certain changes can be made to the iterative process to help ensure convergence, such as allowing one of the disk's vortex sheets to achieve convergence without considering the influence of the second sheet, thereby placing it in a more stable state before introducing the influence of the second sheet and determining the total stable position of both sheets.

Figure 4.6 shows the same vortex ring model for coaxial disks. Points associated with the upper disk's vortex sheet are labeled as $(1, x)$, while those associated with the lower are labeled as $(2, x)$. Note that in the coaxial case, the upper disk's vortex sheet passes through the lower actuator disk. We have the option of maintaining the

same circulation strength for rings that have passed through the lower disk (subject to the correct circulation scaling of Eq. 4.14) or of changing the strength of these ring vortices to reflect a change in the bound circulation of the lower disk. This allows us to model a non-uniform circulation distribution on the lower disk without introducing a third vortex sheet. We use this method to more easily approximate the minimum power thrust distributions shown in Chapter 3, where the lower rotor generates a much larger thrust at points outside of the upper rotor's contracted wake.

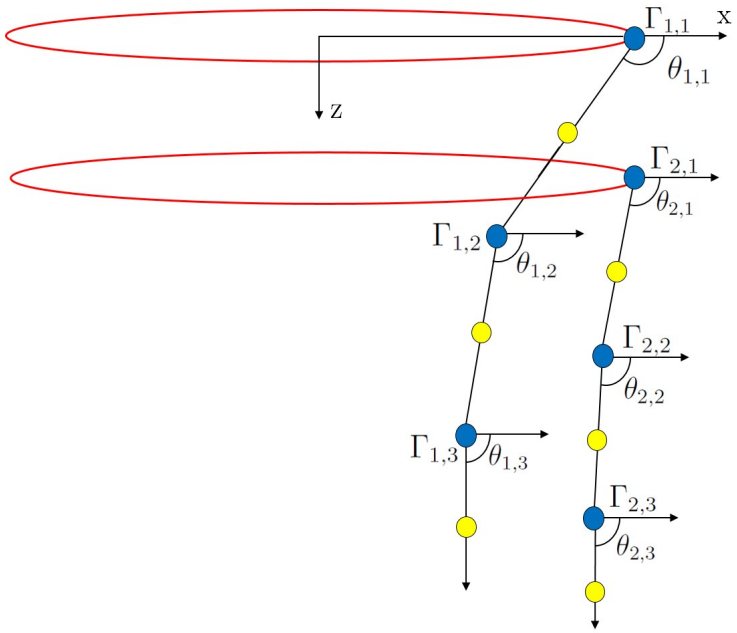

FIGURE 4.6: Schematic of the vortex ring structure of coaxial actuator disks. Yellow circles represent collocation points. Blue circles represent the location of the vortex rings within this azimuthal plane.

4.3 Results

4.3.1 Single Actuator Disk in Hover or Axial Ascent

We first apply our vortex ring model of the wake to a single actuator disk at varying rates of axial ascent, i.e., climb. In axial ascent, the free stream flow has a positive

value and acts in the same direction as the induced flow (like a propeller). In this section, we investigate the structure of the wake, particularly near the edge of the disk, and see how this structure evolves with different rates of axial ascent. We express the rate of climb as the ratio of the climb velocity V_c to the induced velocity at the center of the actuator disk, $V_i(0,0)$. A value of $V_c/V_i = 0$ corresponds to the hover case. For the cases shown here, we use a logarithmic spacing of the ring vortices to allow for small spacing near the edge of the disk where finer detail is needed, and larger spacing downstream where the wake has a slower rate of contraction and a larger spacing is sufficient. We set the entries of the vector of ring spacings **ds** using

$$ds_i = \ln(1.0 + \frac{i}{\mathrm{m}}) \tag{4.15}$$

where the index i starts at a value of 1 at the rim of the actuator disk and the variable m is a constant that can be varied to increase or decrease the spacing for a given case. For the single actuator disk hover case shown here, we set $m = 10,000$ and use 250 rings in the model, while for the axial flight cases, we set $m = 2,000$ and use 115 rings.

Figure 4.7 shows the computed shape of the wake in the vicinity of the rim of the disk for several different climb velocities, including hover. Figure 4.8 shows the same result for a larger domain, allowing us to observe the final contraction of each case. Note that because our model is axisymmetric, we need only look at a given azimuthal slice to visualize the wake. Our results appear to directly support the hypothesis of Spalart [45] that the exact shape of the vortex sheet near the edge of the actuator disk in hover is a 45° logarithmic spiral. Figure 4.9 shows a close up of the hovering case near the edge of the disk. The pitch of a logarithmic spiral is the angle that any tangent to the spiral makes with a tangent to a circle centered on the spiral at the same radius. Drawn on the graph are lines tangent to the wake sheet at the radial coordinate $x = 1$, the x location of the center of the spiral. These tangent lines have

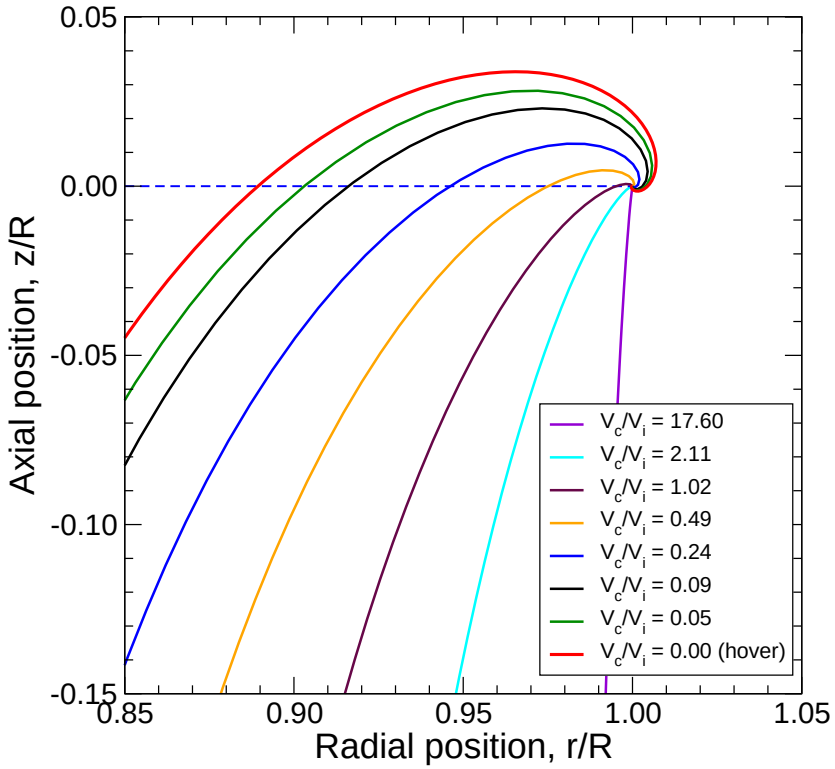

FIGURE 4.7: The shape of the wake near the edge of the actuator disk with decreasing climb velocity. The blue dashed line indicates the location of the actuator disk.

a slope of -1, demonstrating graphically that the wake structure of the hovering rotor very closely approximates a 45° logarithmic spiral. Interestingly, despite the spiral structure at the edge of the disk and the resultant non-uniform induced inflow, the final wake contraction for the hover case shown in Figure 4.8 still approaches the value predicted by a one-dimensional momentum balance of $R_c/R = 1/\sqrt{2} \approx 0.7071$.

Additionally, our findings are in agreement with another of Spalart's assertions, i.e., the extent of the spiral wake shrinks in axial flight but is still present. Figure 4.7 shows that at a climb ratio of $V_c/V_i = 2.11$, the extent of the spiral has shrunk such that it is no longer visible with our vortex ring discretization. However, at climb velocities lower than this, there is still a very clear spiral structure in which the

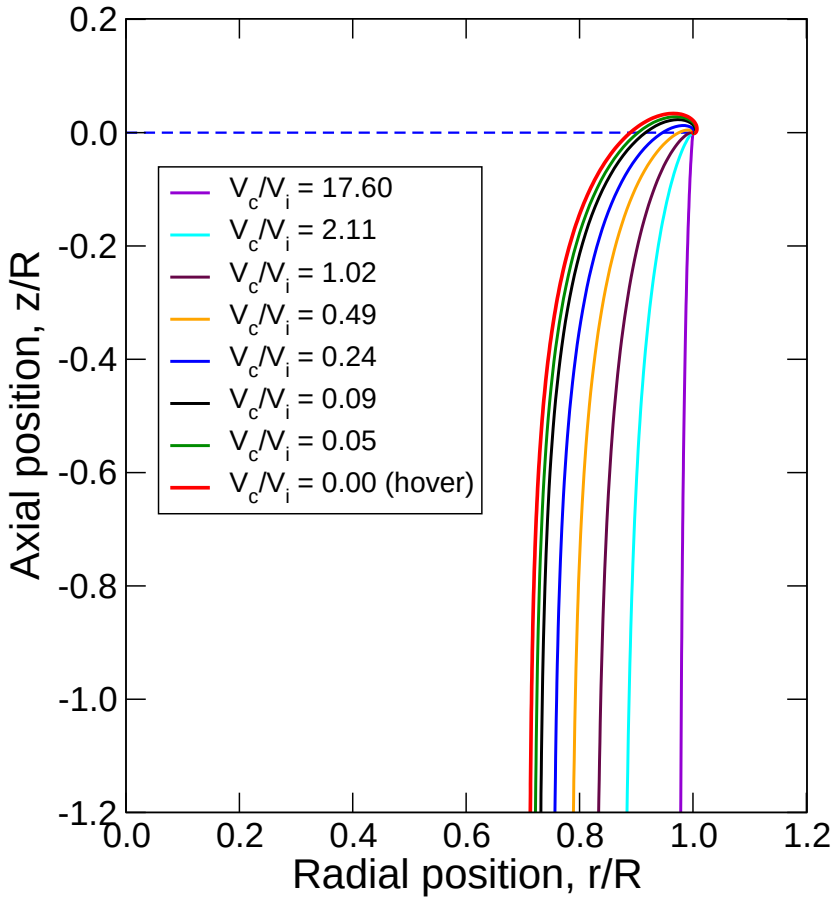

FIGURE 4.8: The shape of the wake with decreasing climb velocity. The blue dashed line indicates the location of the actuator disk.

vortex sheet goes above the actuator disk before passing back through it.

Figure 4.10 shows streamlines for the hovering case. Note that the actuator disk is drawing in flow from all points outside of the streamtube, including areas below and outside the disk. This is in contrast to the notional actuator disk often depicted as shown in Figure 4.1. Rather, fluid directly outside of the sheeet is convected upward and eventually accelerated around the edge of the spiral before being drawn into the actuator disk.

Figure 4.11 shows the axial and radial induced velocities at the actuator disk. In these plots, a downwash on the disk is taken as positive. Note that we have extended the radial coordinate to a value of 1.1, beyond the edge of the actuator

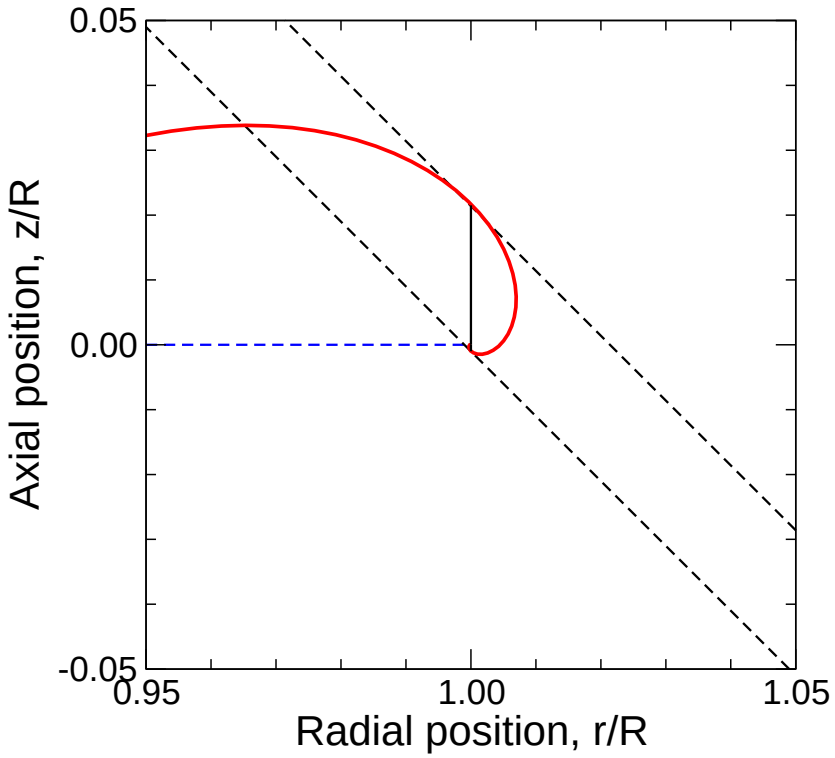

FIGURE 4.9: The shape of the wake near the edge of the actuator disk for the hovering case. Note that the tangent lines are drawn at 45°, indicating that the wake has formed a logarithmic spiral of 45° pitch.

disk, to characterize the flow in this region. For the high climb velocity case of $V_c/V_i = 17.60$, we see that the axial induced velocity distribution is nearly uniform, with a sharp dropoff at the edge of the disk to a value of approximately zero beyond the edge of the disk. This nearly uniform inflow is in line with the classical actuator disk assumptions. As the climb velocity decreases, however, the inflow becomes less uniform. The most striking example is hover. There is a sharp drop in induced inflow at $r/R = 0.87$, which is where the vortex sheet passes through the disk. At points outboard of this, the induced velocity is slightly negative, which is the result of the reversed flow at the disk's edge. The highly non-uniform inflow distribution over the actuator disk has been observed in numerical and analytical solutions by Conway [68], Greenberg and Power [48], and Schmidt and Sparenberg [46], and was

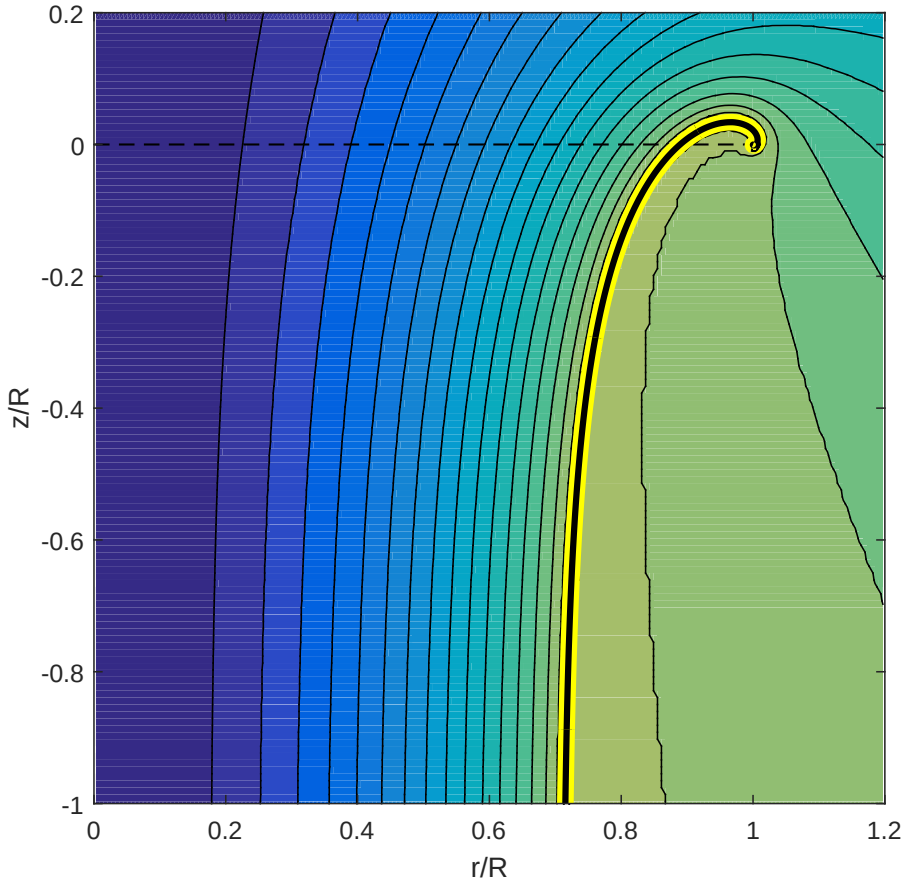

FIGURE 4.10: Streamlines for the hovering actuator disk.

a central topic of Spalart's analysis of the actuator disk in [45].

The radial velocities, shown in the bottom plot of Figure 4.11, go to zero at the center of the actuator disk and have a large negative value at the edge of the disk, indicating radial inflow. At values of V_c/V_i at or below 0.09, we observe a significant change in the radial velocity distribution. This is due to the formation of a larger spiral at the edge of the disk, resulting in a radial outflow as fluid passes through the disk before circling around the tip of the spiral and being ingested by the disk.

Finally, Figure 4.12 shows the thrust distributions for various climb velocities. We can approximate the sectional thrust using

$$dT = 4\pi\rho\left(V_C + V_i\right)V_i r dr \tag{4.16}$$

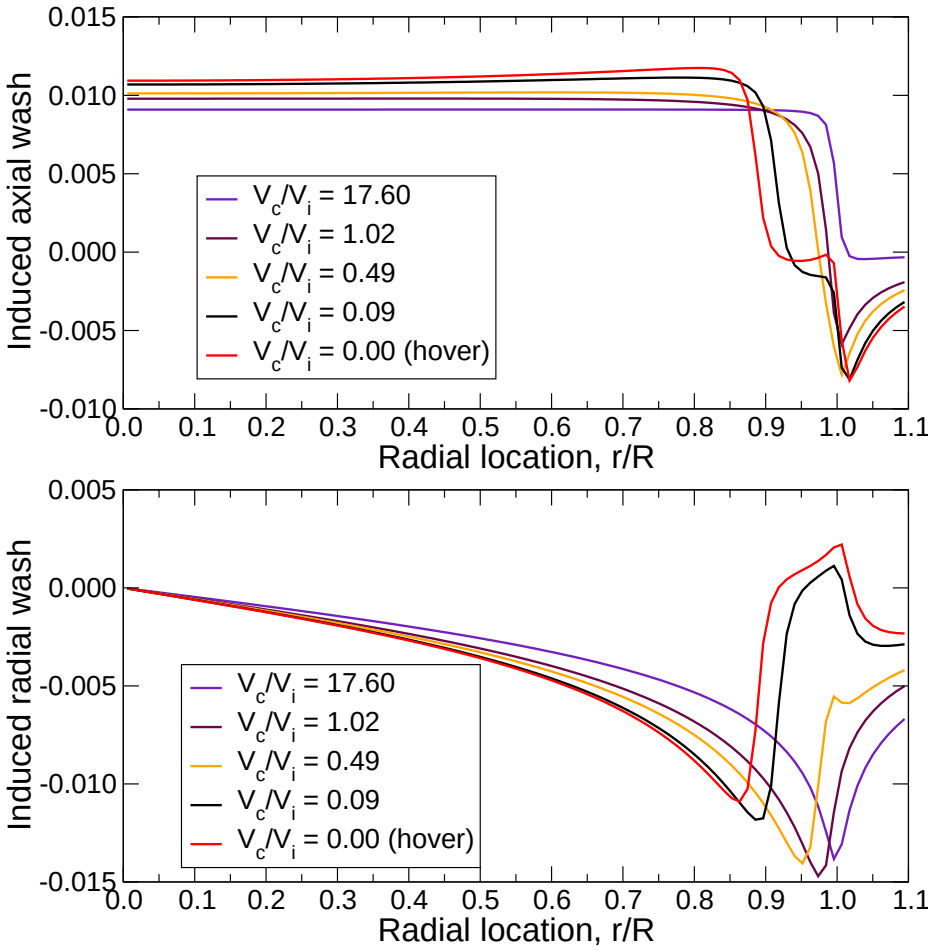

FIGURE 4.11: Top: Radial distribution of induced axial velocity for varying climb velocities. Bottom: Radial distribution of induced radial velocity for varying climb velocities.

where V_i is the radially varying induced velocity over the disk. For clarity, we have normalized the thrust distributions to a value of 1 at $r/R = 0.75$, allowing us to easily compare the thrust distributions at different climb velocities to one another. First, we observe that even at the high climb rates, the thrust rolls off at the tip. We would expect within the conventional uniform inflow actuator disk model that the thrust would be linear, with no tip roll off. However, even the high climb velocity case experiences a small degree of non-uniformity to its induced inflow and thus thrust at the very edge of the disk. As climb velocity decreases, the amount of this

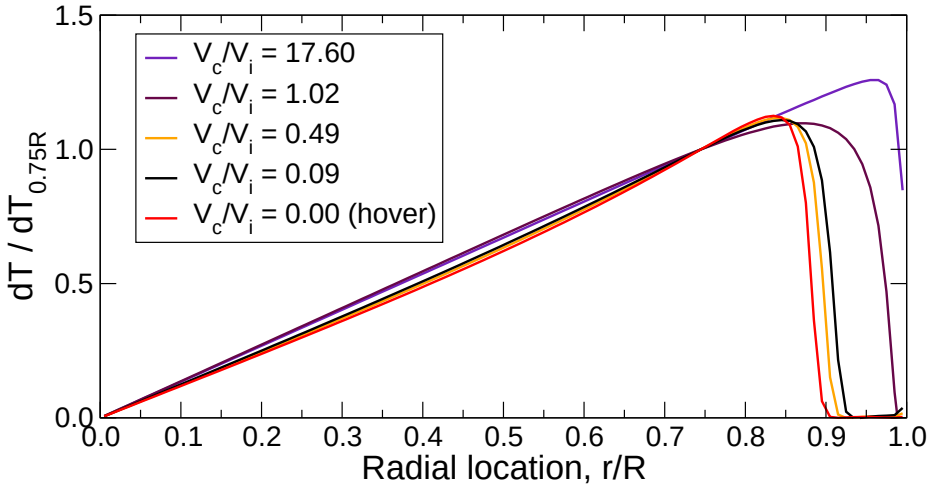

FIGURE 4.12: Radial distribution of thrust for the actuator disk with varying climb velocities. For ease of comparison, each thrust distribution is normalized by its value at $r/R = 0.75$.

rolloff increases, all the way to the hovering case, which has zero or slightly negative thrust outboard of $r/R = 0.87$. This result is explained once again by the spiral structure of the sheet creating a highly non-uniform induced inflow distribution.

4.3.2 Single Actuator Disk in Descent

Figure 4.13 shows the shape of the vortex sheet for a range of negative axial velocities, i.e., for cases where the disk is descending and the induced wash is in the opposite direction of the free stream. Figure 4.14 shows a zoomed out view of the same cases. We see that for larger magnitude negative axial velocities (decreasing V_c/V_i) the spiral at the edge of the actuator disk continues to expand. However, at values of V_c/V_i between -0.2 and -1.9, the iterative method is unable to arrive at a converged solution. This flow condition is commonly referred to as the vortex ring state [74]. Due to the similarity in magnitudes between the induced velocity at the disk and the free stream velocity, and the fact that the two velocities are in opposite directions, this flow state is characterized by significant recirculatory flow and sometimes turbulent flow conditions. At $V_c/V_i < -1.9$, the descent velocity is large enough to fully reverse

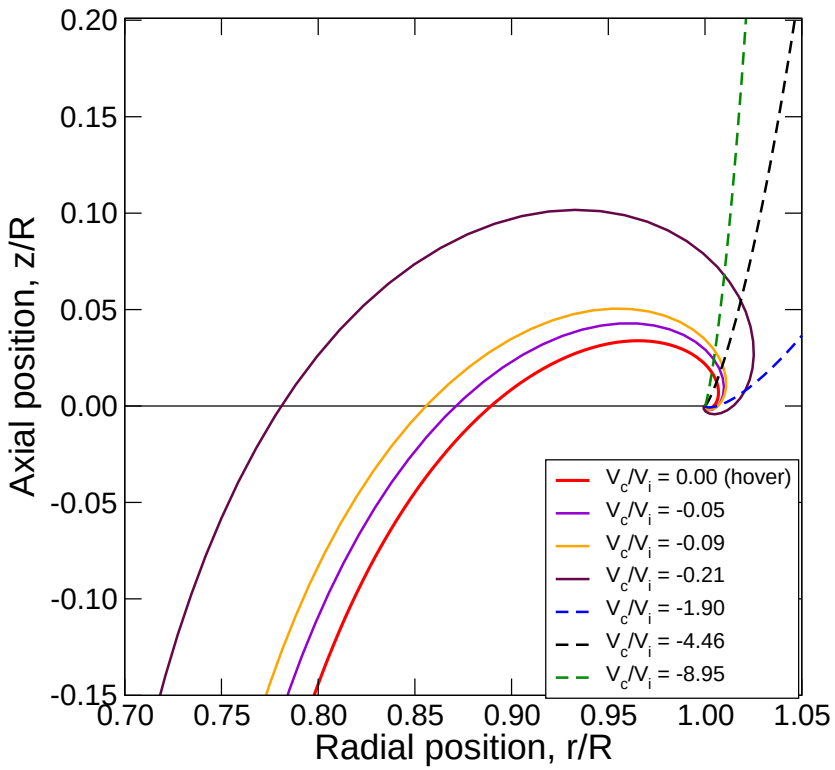

FIGURE 4.13: The shape of the wake near the edge of the actuator disk with various negative climb velocities, i.e., in descending flight. The dashed lines indicate descent velocities at which the rotor has fully transitioned into the windmill state.

the shape of the streamtube, and the iterative approach is once again able to reach a converged shape for the wake. At these large negative values of V_c/V_i, the rotor is still generating an upward thrust, however, it is functioning in a windmill state, slowing the flow and removing energy from the free stream resulting in an expansion of the streamtube. In this condition, we see that the spiral at the edge, although small, has the same orientation as in the hover and climbing axial flight cases.

4.3.3 Single Actuator Disk with Multiple Trailed Vortex Sheets

In this section, we model an actuator disk trailing multiple vortex sheets, allowing us to model piecewise constant circulation distributions. We have defined the sense of vorticity on the outermost sheet as positive; therefore an increase in bound circulation on the disk with increasing r results in a trailing vortex sheet of negative value and

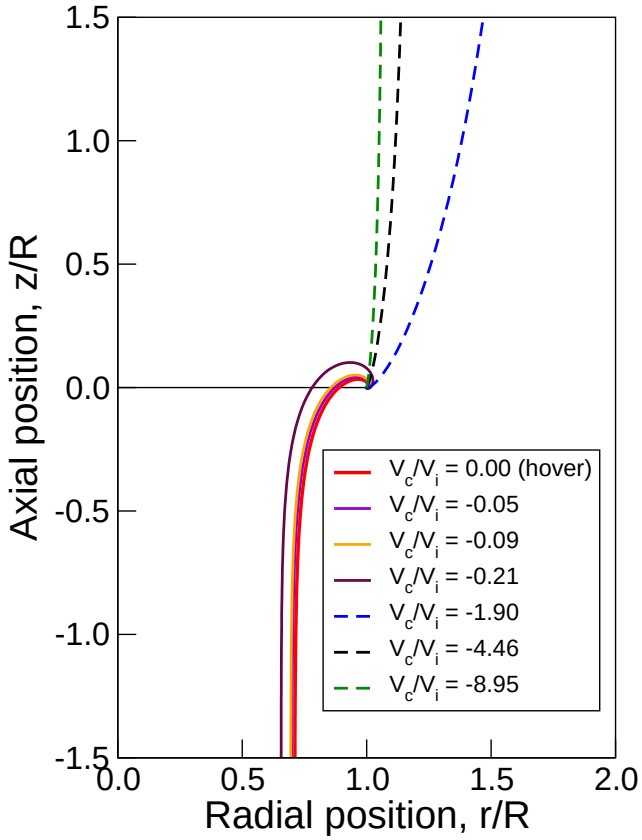

FIGURE 4.14: The shape of the wake with negative climb velocity, i.e., in descending flight. The dashed lines indicate descent velocities at which the rotor has fully transitioned into the windmill state.

vice versa.

We compare two simple cases with multiple filaments: a case with a positive trailing vortex sheet at $r/R = 0.5$, corresponding to a decrease in bound circulation outboard of this point; and a case with a negative trailing vortex sheet at $r/R = 0.5$, corresponding to an increase in bound circulation outboard of this point. Both cases are analyzed in hover. Figure 4.15 shows the shape of the wake for the two cases, and Figure 4.16 shows the streamlines for the negative vorticity case. We see that the negative vortex sheet results in a widening of the streamtubes, i.e., a slowing of the flow at the disk for radial positions inboard of the first vortex sheet. This finding is in agreement with the work of Greenberg and Powers [48],

who used a similar approach to model the axisymmetric flow of an actuator disk with a piecewise uniform circulation distribution. We also observe that the case with positive inboard trailing vorticity has a smaller final contracted radius than both the case with negative vorticity and the case with uniform circulation (Figure 4.8). This result is also in agreement with the conclusion of Greenberg and Powers [48], i. e., that additional positive vorticity on inboard sheets contributes to the contraction of the outer sheet. The case with negative trailing vorticity reduces the extent of the contraction relative to the uniformly loaded case. Also, having an inboard sheet of vorticity that is positive leads to an increase in the size of the spiral at the edge of the actuator disk and a larger region of reversed flow near the edge. The negative vorticity case, in contrast, has a smaller spiral structure that passes back through the disk at a location farther outboard.

Figure 4.17 compares the radial distributions of axial induced wash and thrust for the two cases. As we expect, a positive trailing vortex sheet leads to a decrease in both induced wash and thrust at points outboard of the sheet, while a negative trailing vortex sheet leads to an increase in both quantities. Despite having equal bound circulation from $r/R = 0.5$ to $r/R = 1.0$, the two cases have similar but not identical induced wash and thrust distributions in this region. This is because the wake shape around the edge of the disk is changed by the induced flow field of the inboard sheet, changing the induced velocity (and therefore thrust) of the entire actuator disk. As demonstrated by the similarity in thrust and induced velocity in this region, however, this effect is relatively small.

4.3.4 Coaxial Actuator Disks

In this section, we investigate the wake shape and induced flow field of coaxial actuator disks in hover. We first compare cases with equal bound circulation on the two disks, which results in unequal thrusts and torques between the two rotors due

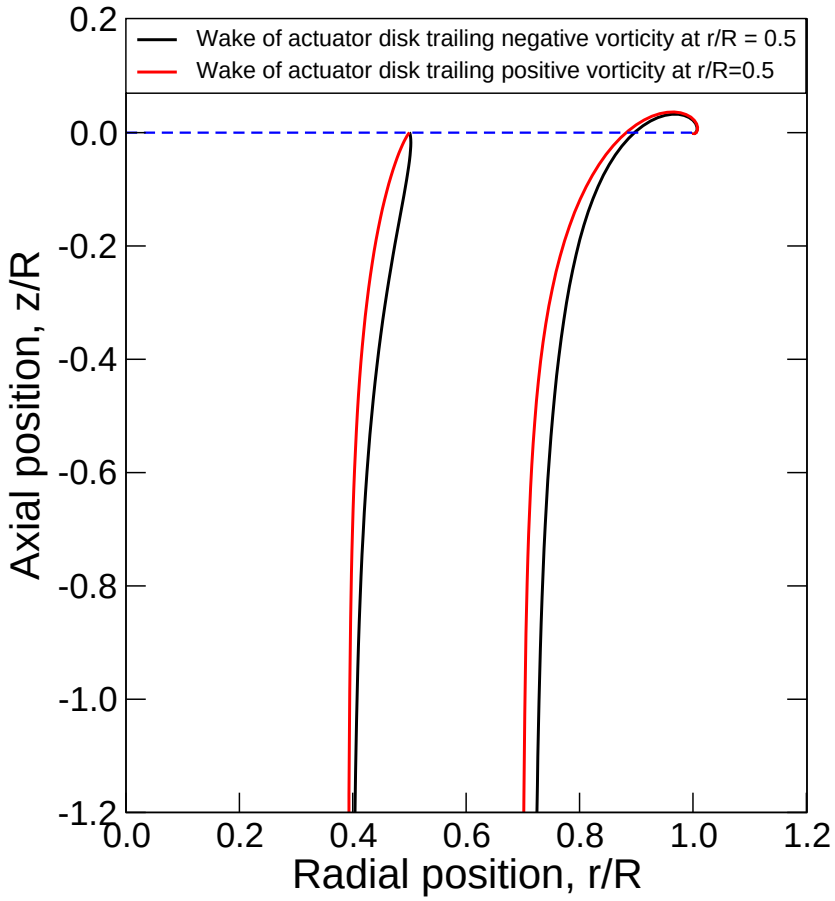

FIGURE 4.15: The shape of the wake of a non-uniformly loaded actuator disk. Each actuator disk has a vortex sheet at the tip and at $r/R = 0.5$, representing either an increase or decrease in circulation on the actuator disk, depending on the sign.

to the difference in mutually induced inflows. We then investigate cases where the lower disk sheds a sheet of negative vorticity at its intersection with the upper disk's vortex sheet leading to an increase in thrust on the outer portion of the lower disk. The net thrust distribution for this case very closely resembles the optimal rotor from Chapter 3. We then compare the mutual interference of the two rotors predicted by our vortex ring model to that predicted by the simple influence coefficient model developed by McAlister et al. [49] and used in the Chapter 3 rotor optimization.

To analyze coaxial disks, we use a logarithmic spacing parameter $m = 800$, defined in Eq. (4.15), for each vortex sheet. We also include a breakpoint in the wake, below

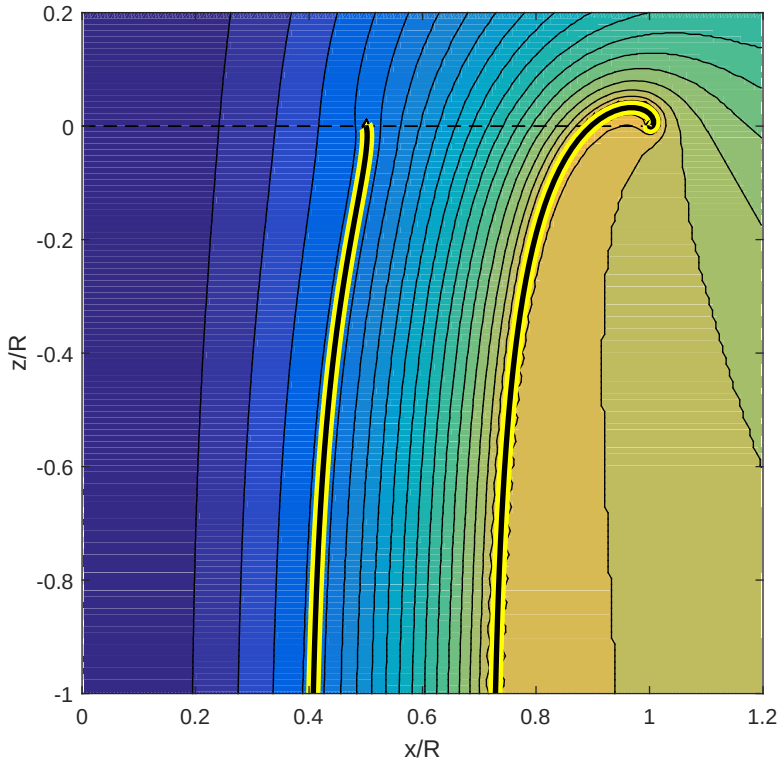

FIGURE 4.16: Streamlines of the non-uniformly loaded actuator disk with a vortex sheet at $r/R = 0.5$ of negative vorticity, resulting in a higher disk loading outboard of this point.

which the ring spacing transitions from logarithmic to linear, a technique that was found to speed up convergence of the Newton iteration. The number of rings used varies with the vertical separation of the disks, but was between 65 and 100 per vortex sheet for every case.

Equal circulation cases

Figure 4.18 shows the induced wash distributions and thrust distributions for coaxial actuator disks with an axial separation of $z/R = 0.3$ and equal circulation on the disks. We see from the top plot of the figure that the upper rotor has a relatively constant induced wash distribution, with a gradual reduction in induced wash towards the tip. This is in contrast to the single actuator disk in hover, shown in

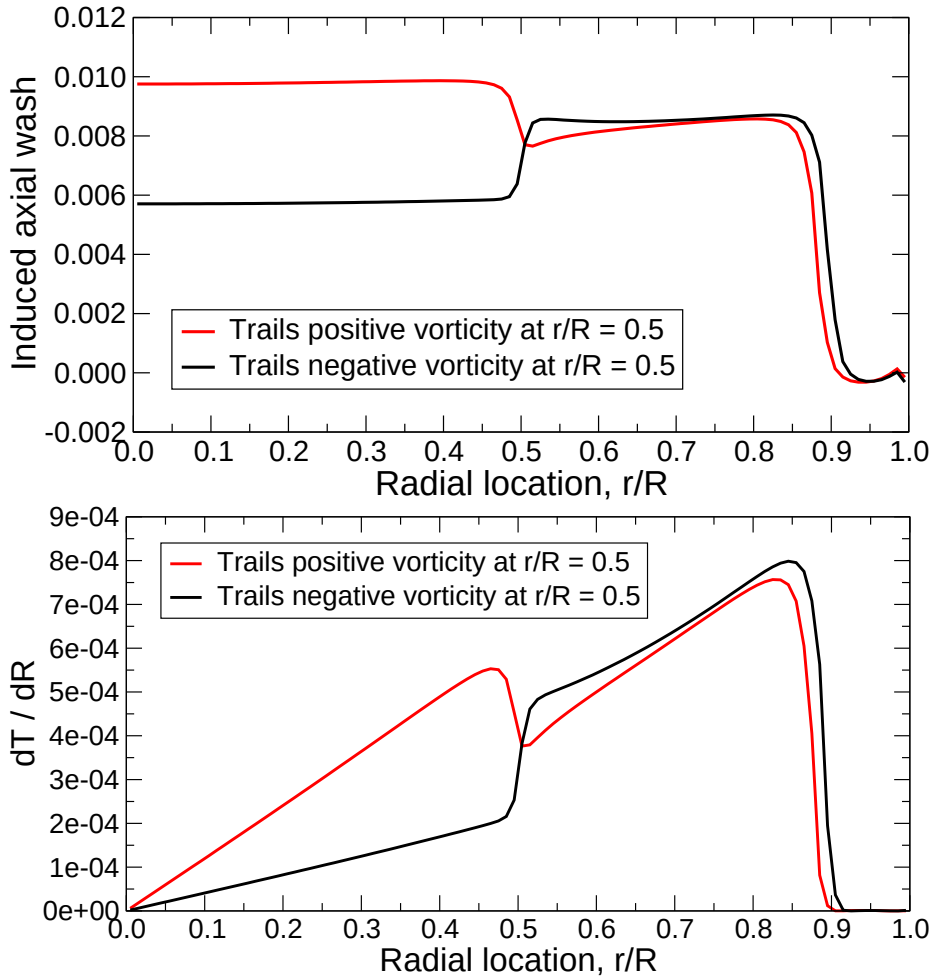

FIGURE 4.17: Top: Radial distribution of induced axial velocity for a non-uniformly loaded actuator disk with a sheet of either positive or negative vorticity at $r/R = 0.5$. Bottom: Radial distribution of thrust for the two cases.

Figure 4.11, where the induced wash is negative outboard of $r/R = 0.87$. The cause of this is well illustrated by the streamlines shown in Figure 4.19. The outer portion of the upper disk is subjected to a sizable wash caused by the lower disk drawing in flow. As a result, the edge spiral is significantly less pronounced, just as the edge spiral of a disk in axial flight is less pronounced (cf. Figure 4.7). The result is a more uniform induced wash distribution. The lower actuator disk sees the opposite effect: it is subjected to a small upward velocity induced by the upper rotor drawing in flow from its sides. This is equivalent to the lower disk operating in a descending

flight condition. The result is a more pronounced edge spiral and small or negative induced wash outboard of where this spiral passes through the actuator disk. In the far field, we observe that the velocity is not uniform, as the portion of the wake that passes through both actuator disks, which extends from the hub to $r/R \approx 0.6$, has a higher velocity than the outer portion that only passes through the lower disk.

The middle plot of Figure 4.18 divides each disk's induced wash into components resulting from the upper disk's vortex sheet and the lower disk's vortex sheet. In other words, this plot quantifies which elements of the inflow are self induced and which are a result of the interference of the other disk. We see that the lower disk induces a sommoth wash distribution on the upper disk that decreases somewhat towards the tip. The upper disk induces a large positive wash over the lower disk within its contracted wake, and a small negative induced wash over the outer portion of the lower disk.

The third plot of Figure 4.18 shows the thrust distributions for each disk. Per Eq. (4.16), the thrust is a product of the total mass flow through a disk and the velocity induced by that disk. As we can see from the middle plot of the figure, the lower disk both induces a larger wash on itself, because of the more pronounced shape of its edge spiral, and has a larger total inflow due to the upper disk's contracted wake. These effects compound in the form of a much higher thrust on the lower rotor. In total, the lower rotor generates over twice the thrust of the upper rotor. Of course, even for constant bound circulations, the lower rotor has a step change in thrust, as the area outside of the upper rotor's wake sees a drop off in inflow and a decrease in thrust.

For comparison, Figure 4.20 shows streamlines for coaxial actuator disks of equal circulation with a (larger) vertical separation of $z/R = 0.5$. Because of the larger vertical separation, the upper disk's wake has contracted to a smaller radius before impinging upon the lower disk.

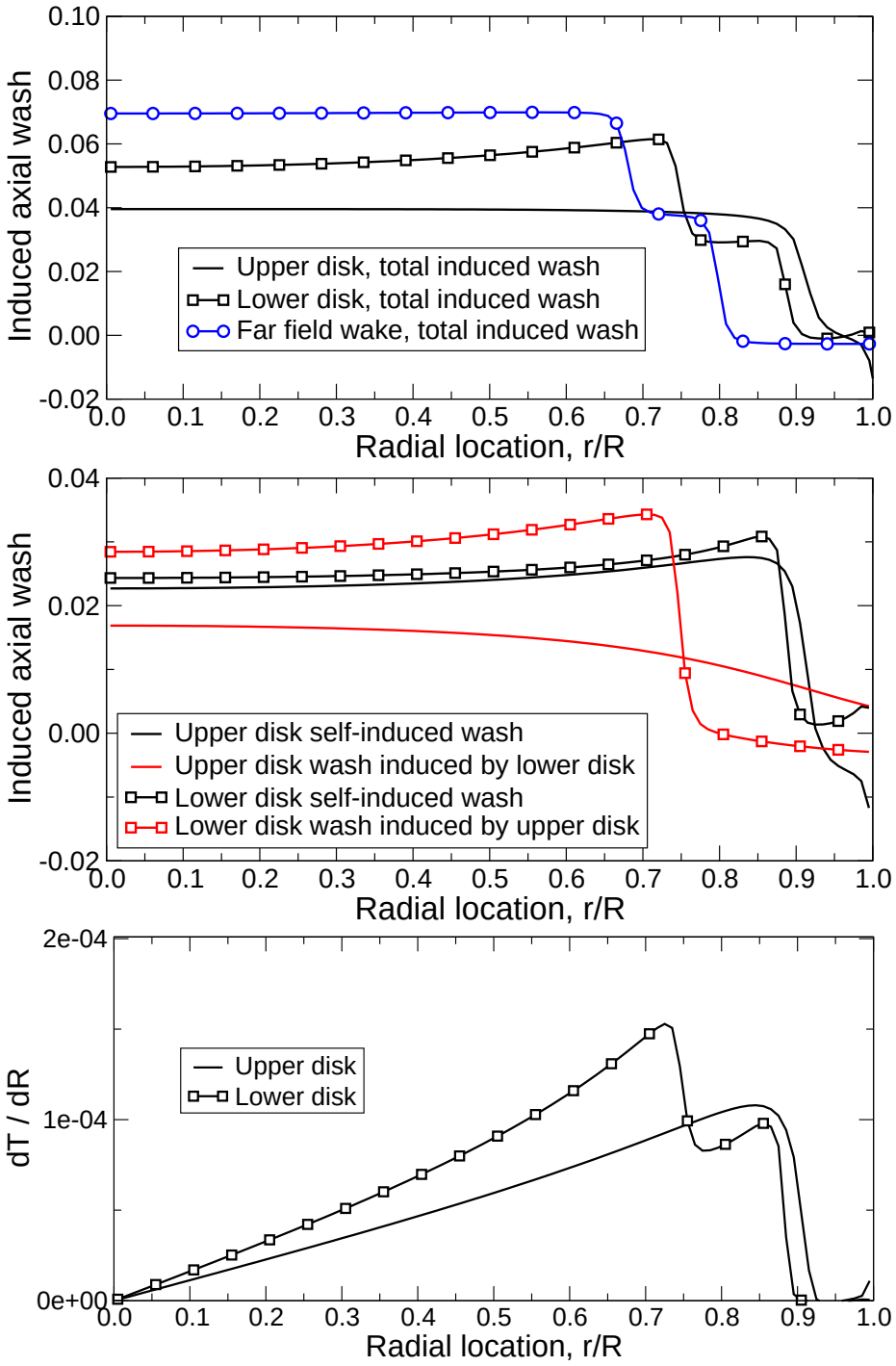

FIGURE 4.18: Top: Radial distribution of induced axial velocity for non torque-balanced coaxial actuator disks with vertical separation of $z/R = 0.3$. Middle: Radial distribution of induced axial velocity split into contributions from each of the two disks' vortex sheets. Bottom: Radial distribution of thrust.

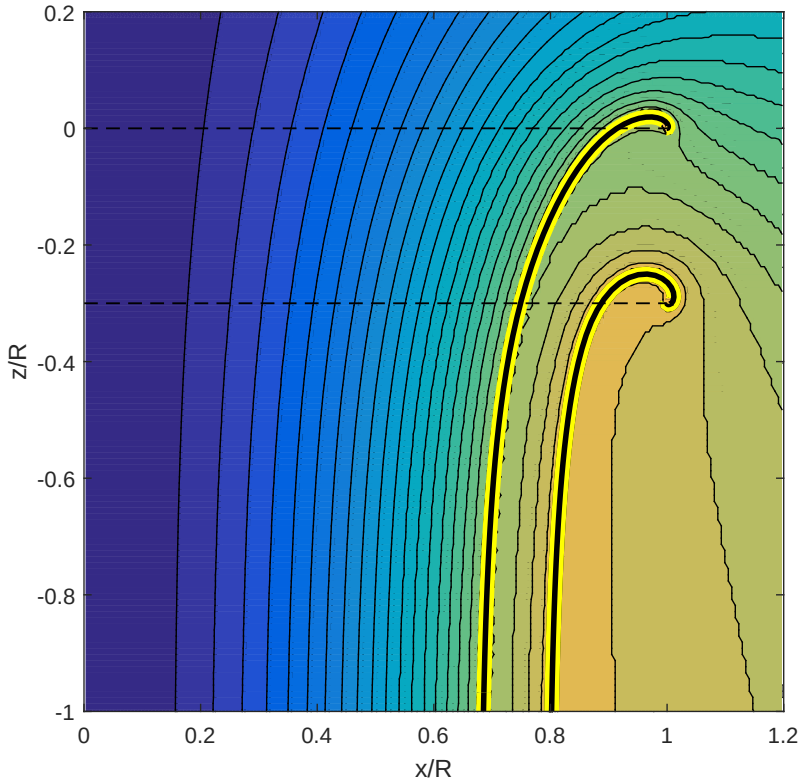

FIGURE 4.19: Streamlines of non-torque balanced coaxial actuator disks with a vertical separation of $z/R = 0.3$.

Torque balanced cases

The coaxial actuator disks investigated in the previous section had equal circulation distributions, which, due to differences in wake structure and mutual interference between the two disks, results in highly unequal thrusts on the two disks. Additionally, though not shown, the two disks also had very different induced powers (which, for equal rotation rate, is equivalent to torque). In this section we investigate coaxial actuators disks that have equal torque, thereby more closely approximating the actual operating state of a hovering coaxial rotor with no anti-torque device. Additionally, we introduce a change in vorticity to the upper disk's vortex sheet as it passes through the lower disk to model a change in the bound circulation of the lower disk. We set this change in vorticity to be negative, thereby causing an increase in

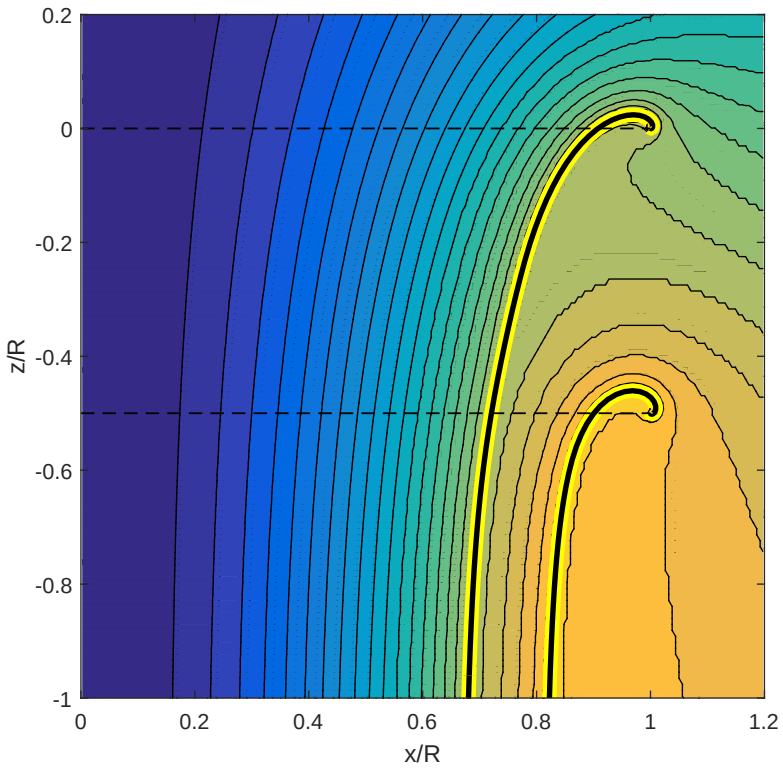

FIGURE 4.20: Streamlines of non-torque balanced coaxial actuator disks with a vertical separation of $z/R = 0.5$.

the thrust generated by the lower rotor outboard of this trailed vortex. Using this technique, we are able to approximate the thrust distributions of the optimal coaxial rotor found in Chapter 3 and make direct comparisons of our vortex ring model's mutual interference to the influence coefficient model used for the optimization. We compute the differential induced power of a given actuator disk using

$$dP_i = V_i dT \tag{4.17}$$

in combination with Eq. (4.16)

Figure 4.21 shows the axial induced wash and differential thrust distribution for torque balanced actuator disks with a vertical separation of $z/R = 0.16$, the same vertical separation used on the optimized coaxial rotor of Chapter 3. Note that the far field induced wash is now uniform within the slipstream, in contrast to the non-

torque balanced case shown in Figure 4.18 where there was a non-uniform far field flow. In the middle plot of Figure 4.21, we see a large increase in the self-induced velocity of the lower rotor at $r/R = 0.85$. This is caused by the change in vorticity of teh upper disk's vortex sheet as it passes through the lower disk. Finally, the thrust distributions shown in the bottom plot also reflect this large increase in circulation due to the additional trailed vorticity. To achieve equal induced power losses, the upper disk generates 56% of the total system thrust, which is a similar thrust sharing ratio to that found in Chapter 3.

Figures 4.22 and 4.23 show the streamlines for torque balanced cases with vertical separations of $z/R = 0.16$ and $z/R = 0.3$, respectively. Although not plotted here, the $z/R = 0.3$ case has a qualitatively similar thrust distribution to the $z/R = 0.16$ case, with a large increase in thrust over the outer portion of the lower disk. Not surprisingly, we observe a very slight expansion in the upper disk's vortex sheet as it passes through the lower disk and changes vorticity. This is slightly more pronounced in the $z/R = 0.3$ case.

Finally, Figure 4.24 compares the mutual interference predicted by our vortex ring model to that predicted by the influence coefficient model developed by McAlister et al. [49]. The McAlister coefficient model was used in the Chapter 3 BEMT coaxial optimization to predict the influence of the lower rotor on the upper rotor. Additionally, it was used to determine the contraction of the upper rotor's wake at the lower rotor. The upper rotor's outflow was then mapped to this contracted radius on the lower rotor and scaled to conserve mass. Compared to the present actuator disk model, the influence coefficient model underpredicts the wash on the upper rotor induced by the lower rotor, and does not capture the increased induced flow near the edge of the disk. The influence of the upper rotor on the lower rotor is qualitatively similar between the two models. Inside of the contracted streamtube, the predicted induced velocities are in reasonably good agreement. Outside of the

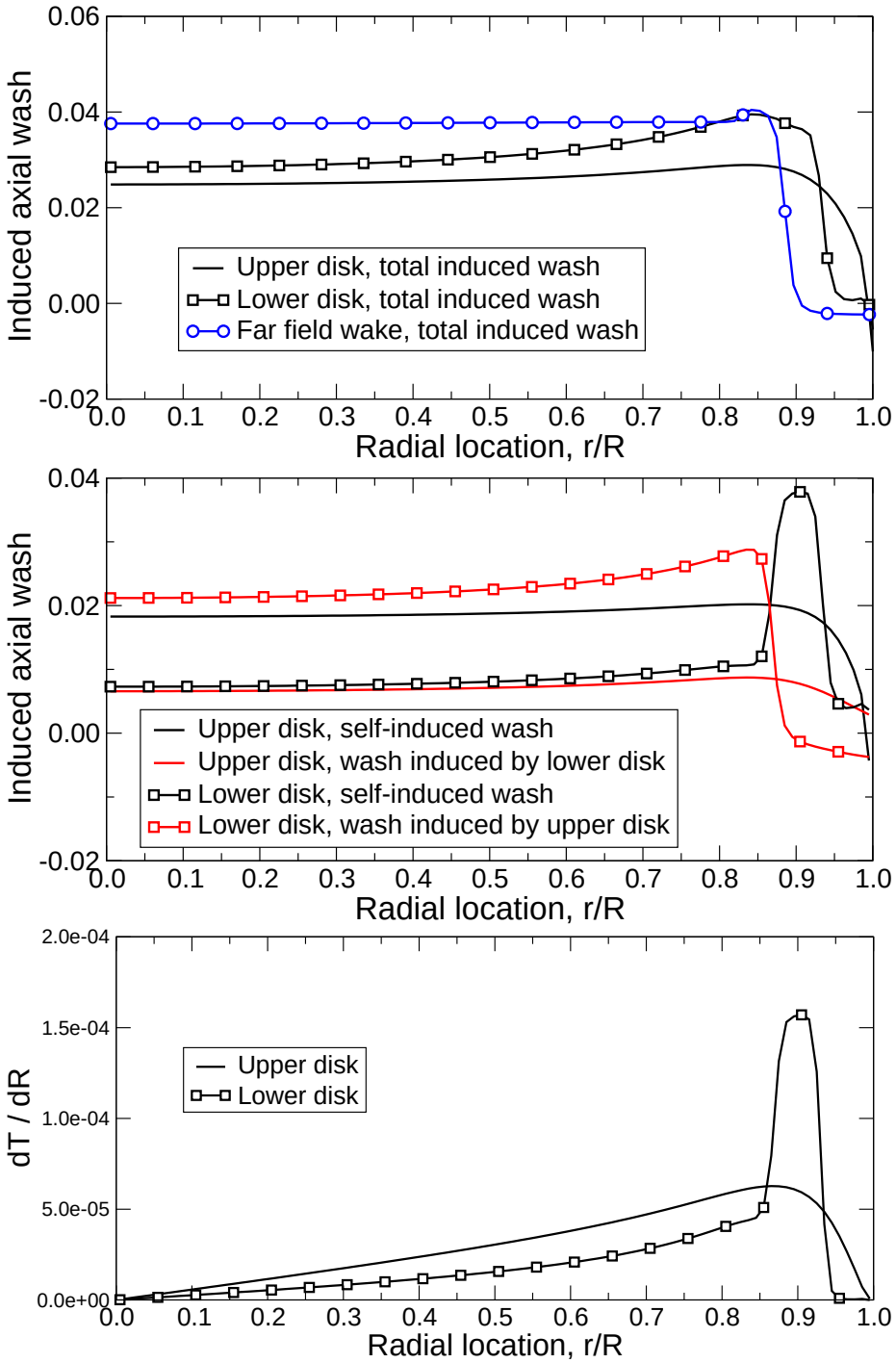

FIGURE 4.21: Top: Radial distribution of induced axial velocity for torque-balanced actuator disks with vertical separation of $z/R = 0.16$. Middle: Radial distribution of induced axial velocity split into contributions from each of the two disks' vortex sheets. Bottom: Radial distribution of thrust.

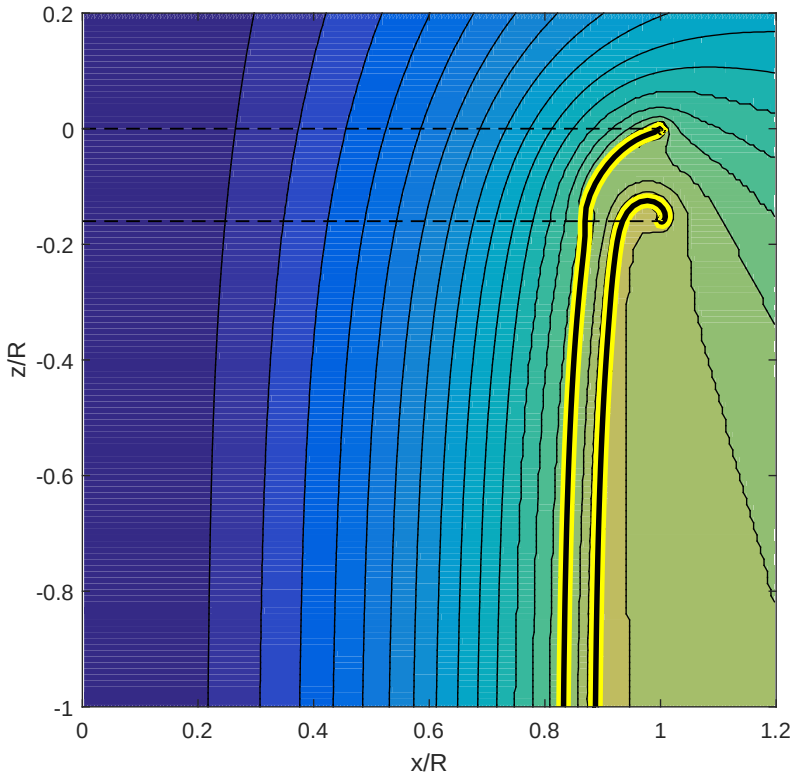

FIGURE 4.22: Streamlines of torque balanced coaxial actuator disks with a vertical separation of $z/R = 0.16$.

contracted streamtube, the influence coefficient model assumes zero influence on the lower rotor, while the actuator disk model predicts a small negative induced velocity drawn up through the lower rotor by the upper rotor. As a final observation, the predicted wake contraction as a function of vertical separation by the influence coefficient model is in good agreement with our actuator disk model.

4.4 Conclusions

We have developed a vortex ring model of the axisymmetric flow through an actuator disk. We represent the continuous vortex sheet of the wake using discrete vortex rings with non-uniform spacing. We impose a no through flow boundary condition on the vortex sheet and determine its position via Newton iteration. The model can be

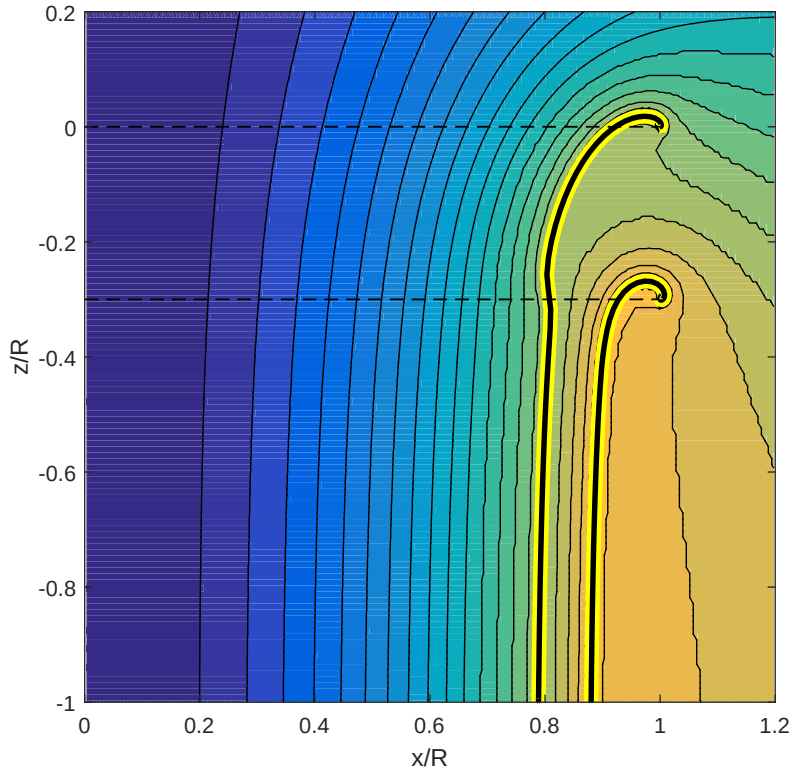

FIGURE 4.23: Streamlines of torque balanced coaxial actuator disks with a vertical separation of $z/R = 0.3$.

used for multiple vortex sheets, allowing us to analyze non-uniformly loaded single and dual coaxial actuator disks. We investigated a variety of cases and arrived at the following conclusions:

1. The singularity that occurs where the vortex sheet terminates at the edge of the actuator disk is resolved through the formation of a 45° logarithmic spiral in hover, as originally hypothesized by Spalart [45]. The spiral structure of the wake results in a non-uniform inflow, particularly near the edge of the disk, that includes reversed flow through the actuator disk.

2. In axial flight, the size of this spiral decreases, although it is always theoretically present, vanishing in the limit where V_c/V_i approaches infinity.

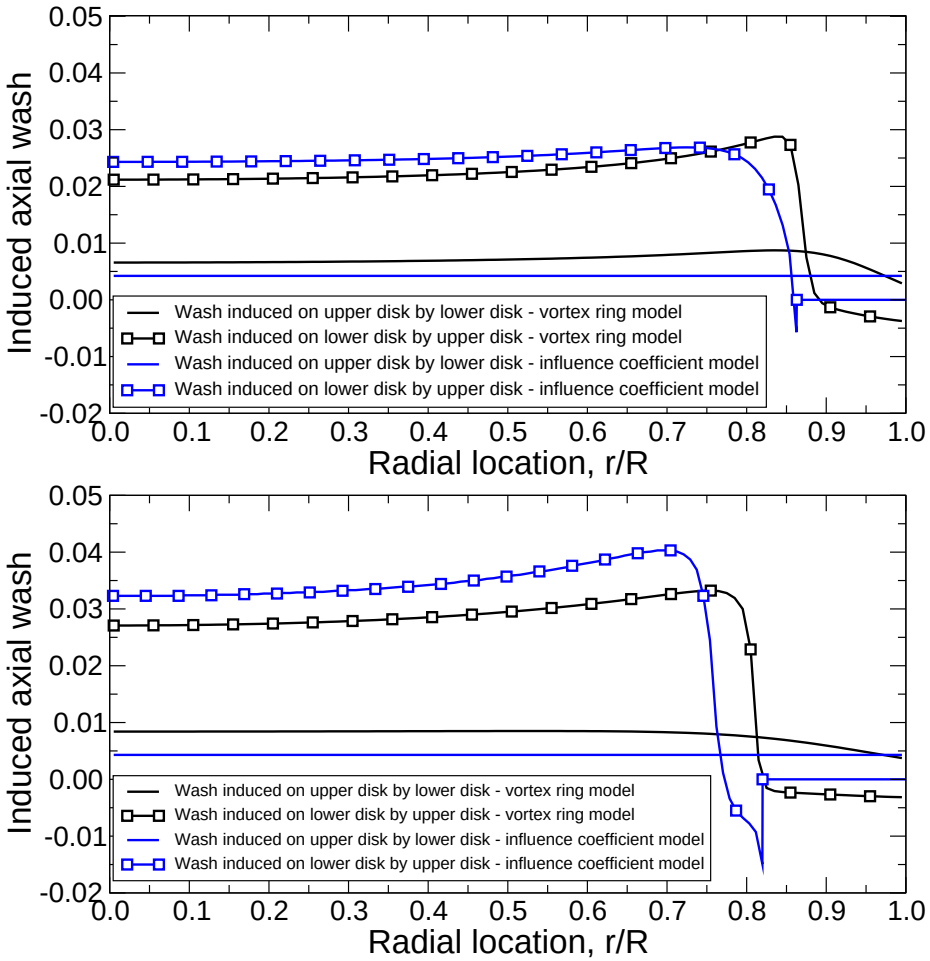

FIGURE 4.24: Top: Comparison of the mutual interference predicted by the axisymmetric potential flow vortex ring model with those predicted by the influence coefficient model of McAlister [49] for a vertical separation $z/R = 0.16$. Bottom: Same comparison for a vertical separation of $z/R = 0.3$.

3. In the case of descending flight, the size of the spiral structure increases with descent rate until the wake enters the vortex ring state. In the vortex ring state, no converged solution can be found using the methods described here. Once the descent velocity is sufficiently high, the disk enters a windmill state, which also produces a spiral vortex sheet structure at the actuator disk tip of the same orientation as the climb and hover cases. In the windmill state, the vortex sheet convects in the direction of the free stream flow, compared to the

low descent velocity cases where the vortex sheet convection and free stream are in opposite directions.

4. Actuator disks with multiple vortex sheets still contain the spiral structure at the terminus of the sheet, although the spiral is significantly smaller (or undetectable) on the inboard filaments. The case with multiple trailed vortex sheets of positive vorticity increases the total contraction of the wake, while the case with an inboard sheet of negative vorticity decreases the final wake contraction.

5. Coaxial actuator disks have a pronounced spiral structure on the lower disk, where the upwash induced by the upper disk acts as a descent velocity for the edge of the lower disk. The upper disk sees the opposite effect, with a net flow through the disk in the traditional direction induced by the lower disk, suppressing the spiral structure and more closely resembling an actuator disk in climbing axial flight.

6. For the non-torque-balanced coaxial actuator disks, the far field flow is not uniform, but rather has a change in velocity from the fluid that passes through both actuator disks and the fluid that enters the slipstream through the lower disk only. For both torque-balanced coaxial cases analyzed here, the far field velocities are nearly uniform.

7. The mutual interference effects predicted by our vortex ring model agree reasonably well with the predictions made using the influence coefficient model of McAlister et al. [49] and used in Chapter 3, with two notable differences. First, the influence of the lower rotor on the upper rotor is underpredicted by the McAlister model compared to the vortex ring model. Second, the influence of the upper rotor on the outer portion of the lower rotor is approximated

as zero in the McAlister model, while the vortex ring model predicts a small upwash through the lower disk in this region.

5

Multipoint Optimization of Conventional and Coaxial Helicopters

In Chapter 2 we described a technique for determining the optimal blade twist, chord distribution, and periodic blade pitch inputs for a conventional or coaxial rotor in high speed forward flight, using either conventional collective and cyclic or higher harmonic control. We applied this method to a compound vehicle in forward flight operating at a single high speed advance ratio. In the design of a practical rotor, it may be advantageous to optimize rotor design to balance performance between two or more flight conditions, for example, between two different advance ratios or between a forward flight advance ratio and hover. As evidenced by the optimal forward flight coaxial rotors shown in Chapter 2 (*cf.* Figure 2.5) and the optimal hovering rotor design of Chapter 3 (*cf.* Figure 3.15), the hovering and high speed flight regimes have considerably different optimal designs. It is interesting to explore what rotor design best balances performance between these two conditions, and what performance tradeoffs must be made at each flight condition to achieve a balanced solution.

There have been a number of previous investigations on the effect of rotor blade shape and geometry on helicopter rotor performance at multiple flight conditions. Johnson [16], Yeo and Johnson [22, 75], Johnson, Moodie, and Yeo [23], and Moodie and Johnson [7] have all sought to optimize various rotor parameters – including blade twist and chord distributions – of a compound helicopter configuration to balance hover and forward flight performance. In each of these studies, a rotor design that optimizes the performance between two conditions was typically determined using parametric variation informed by the sensitivities of a very limited number of design variables describing blade chord and twist. The performance of each combination of twist variables was computed using the comprehensive code CAMRAD and then examined graphically in a plot of forward flight performance versus hover performance.

Rand and Khromov [25] describe a method for performing a multipoint optimization of compound helicopters. The authors were able to determine the hover-forward flight Pareto frontiers, defined as the set of rotor designs for which it is impossible to improve upon the performance in one of the two flight conditions without degrading the performance in the other [76], by first randomly varying important design parameters and plotting the hover versus cruise performance. Figure 5.1 shows the results of this first step, with each point indicating a given rotor design and red solid lines indicating the apparent Pareto frontiers. Designs that are "non-dominated," i.e., near the apparent Pareto frontier, were then further optimized via gradient based optimization techniques.

In this chapter, we describe a method for performing a multipoint optimization that is capable of mapping the entire Pareto frontier directly for any arbitrary number of design variables, eliminating the need to evaluate the performance of a rotor for hundreds or thousands of random parametric variations. The problem is posed as a constrained optimization problem and solved directly using Newton iteration. We

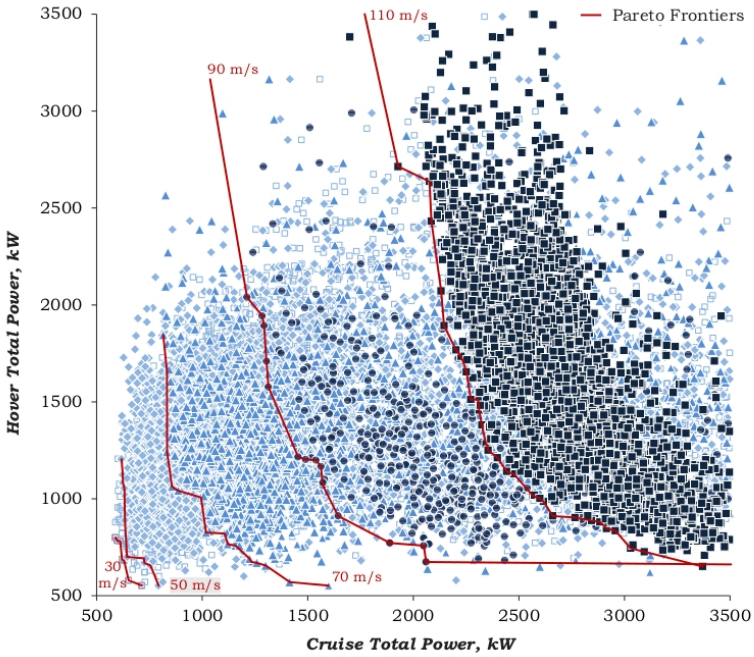

FIGURE 5.1: Pareto frontiers for various forward flight velocities and hover, determined by randomly varying design variables, from Rand and Khromov [25].

apply the method to both conventional and coaxial rotors, for both hovering and forward flight conditions, and for both conventional (collective and cyclic) blade pitch control and higher harmonic control.

5.1 Approach: Cruise/Cruise Multipoint Optimization

For a single point forward flight optimization, we use the approach described in Chapter 2 to determine the design variables that minimize total power while producing a certain lift and/or thrust, and keep the helicopter in pitch and roll trim. For ease of reference, we provide here a very brief summary of the single point forward flight optimization. The aerodynamic model we use is a lifting-line/vortex-lattice model, that is, the blades are modeled with a single line of vortex filaments and the prescribed wake is modeled with a lattice of quadrilateral vortex rings. Sectional drag polars modeled using C81 tables are used to account for profile losses, including

both viscous and compressible losses.

Using this lift-line/vortex-lattice model, the unknown circulation strengths are related to the blade geometry and control inputs through a set of nonlinear equations of the form

$$\mathbf{R}(\boldsymbol{\Gamma}, \boldsymbol{\theta}) \tag{5.1}$$

where $\boldsymbol{\Gamma}$ is the vector of circulation values at a number of discrete spanwise and azimuthal locations, and $\boldsymbol{\theta}$ is the vector of rotor design variables and control inputs. The vector of design variables $\boldsymbol{\theta}$ can include fixed blade twist and blade chord distributions along the blade span, and conventional or higher harmonic blade pitch control inputs.

The aerodynamic forces and moments acting on the rotor and given in integral form in Eqs. (2.1) and (2.2) can be expressed in terms of the circulation, i.e.,

$$\mathbf{F} = \mathbf{B}\boldsymbol{\Gamma} \tag{5.2}$$

$$\mathbf{M} = \mathbf{D}\boldsymbol{\Gamma} \tag{5.3}$$

where $\mathbf{B}$ and $\mathbf{D}$ are matrices relating the circulation distribution to the forces and moments generated, respectively.

Additionally, the total power loss for the rotor (the wasted power) is given by

$$P = \frac{1}{2}\boldsymbol{\Gamma}^T\mathbf{K}\boldsymbol{\Gamma} + P_{\mathrm{v}} \tag{5.4}$$

The matrix $\mathbf{K}$ relates the circulation distribution $\boldsymbol{\Gamma}$ to the induced power P_{i}. P_{v} is the profile power loss, and accounts for both viscous and compressible contributions to the drag of the airfoil (cf. Eqs. (2.7) and (2.9) from Chapter 2).

To cast the problem as a variational problem, we adjoin to the power (the cost function to be minimized) the force and moment constraints using Lagrange multipliers, that is,

$$\Pi = \frac{1}{2}\boldsymbol{\Gamma}^T\mathbf{K}\boldsymbol{\Gamma} + P_{\mathrm{v}} + \boldsymbol{\lambda}_F^T \cdot (\mathbf{B}\boldsymbol{\Gamma} - \mathbf{F}_{\mathrm{R}}) + \boldsymbol{\lambda}_M^T \cdot (\mathbf{D}\boldsymbol{\Gamma} - \mathbf{M}_{\mathrm{R}}) + \boldsymbol{\lambda}_R^T \cdot \mathbf{R}(\boldsymbol{\Gamma}, \boldsymbol{\theta}) \tag{5.5}$$

where $\mathbf{M}_{\mathrm{R}}$ and $\mathbf{F}_{\mathrm{R}}$ are the prescribed forces and moments. To find the constrained optimum, one takes the variation of Eq. (5.5) and sets the result to zero for arbitrary variations in the unknown circulation, control inputs, and Lagrange multipliers. The result is a large set of nonlinear algebraic equations that are solved numerically for the optimum.

To perform a multipoint optimization, the process is similar except that now we consider two flight conditions denoted by the subscripts 1 and 2. These two flight conditions could represent different advance ratios, tip Mach numbers, disk loadings, elevation, or other conditions of interest. Of course, the blade geometries (chord and twist distributions) will be the same for the two flight conditions. The azimuthal variation of blade pitch, on the other hand, will necessarily be different for the two flight conditions to maintain flight trim. Thus, the total set of design variables describing the rotor geometry and control inputs for the two flight conditions are

$$\boldsymbol{\theta} = \left\{ \begin{array}{c} \boldsymbol{\theta}_{\mathrm{twist}} \\ \boldsymbol{\theta}_{\mathrm{chord}} \\ \boldsymbol{\theta}_{\mathrm{root1}} \\ \boldsymbol{\theta}_{\mathrm{root2}} \end{array} \right\} \tag{5.6}$$

where $\boldsymbol{\theta}_{\mathrm{twist}}$ and $\boldsymbol{\theta}_{\mathrm{chord}}$ are the design variables that describe the common fixed blade twist and chord distributions, respectively. $\boldsymbol{\theta}_{\mathrm{root1}}$ and $\boldsymbol{\theta}_{\mathrm{root2}}$ describe the root pitch inputs (conventional or higher harmonic control) at flight condition 1 and 2, respectively, which are independent and have no effect on rotor performance at the other flight condition.

Because the two flight conditions in general occur at different advance ratios, the wake geometries for the two conditions will be different, and separate vortex lattice grids must be used for each. Therefore, the matrices $\mathbf{A}$, $\mathbf{B}$, $\mathbf{D}$, and $\mathbf{K}$, as well as the circulation vector $\boldsymbol{\Gamma}$, will differ for the two conditions, and are distinguished by the subscripts 1 or 2.

In the multipoint optimization, we minimize a weighted sum of the power loss for the two flight conditions, with a weight of α applied to flight condition 1 and β to flight condition 2, where $\beta = 1 - \alpha$. When $\alpha = 1$, for example, the optimization minimizes only the power at the first flight condition, while satisfying the trim constraints and evaluating performance at both flight conditions. By varying α between 0 and 1, we are able to find the Pareto frontier.

As before, we seek to minimize the (weighted) power loss, while satisfying the trim constraints at the two flight conditions. Thus we adjoin separate (unweighted) moment and force constraints for each flight condition to the power loss. The resulting Lagrangian power is given by

$$\begin{aligned}\Pi = &\alpha\left(\frac{1}{2}\boldsymbol{\Gamma}_1^T\mathbf{K}_1\boldsymbol{\Gamma}_1 + P_{v1}\right) + \beta\left(\frac{1}{2}\boldsymbol{\Gamma}_2^T\mathbf{K}_2\boldsymbol{\Gamma}_2 + P_{v2}\right)\\ &+ \boldsymbol{\lambda}_{F1}{}^T\cdot(\mathbf{B}_1\boldsymbol{\Gamma}_1 - \mathbf{F}_{R1}) + \boldsymbol{\lambda}_{F2}{}^T\cdot(\mathbf{B}_2\boldsymbol{\Gamma}_2 - \mathbf{F}_{R2})\\ &+ \boldsymbol{\lambda}_{M1}{}^T\cdot(\mathbf{D}_1\boldsymbol{\Gamma}_1 - \mathbf{M}_{R1}) + \boldsymbol{\lambda}_{M2}{}^T\cdot(\mathbf{D}_2\boldsymbol{\Gamma}_2 - \mathbf{M}_{R2})\\ &+ \lambda_{R1}\cdot\mathbf{R}_1(\boldsymbol{\Gamma}_1,\boldsymbol{\theta}) + \lambda_{R2}\cdot\mathbf{R}_2(\boldsymbol{\Gamma}_2,\boldsymbol{\theta})\end{aligned} \tag{5.7}$$

where

$$\mathbf{R}_1(\boldsymbol{\Gamma}_1,\boldsymbol{\theta}) = \mathbf{R}_2(\boldsymbol{\Gamma}_2,\boldsymbol{\theta}) = 0 \tag{5.8}$$

We can approximate the change in the circulation due to a change in design variables at each flight condition by

$$\begin{aligned}\boldsymbol{\Gamma}_1 &\approx \boldsymbol{\Gamma}_{01} + \mathbf{A}_1\Delta\boldsymbol{\theta}\\ \boldsymbol{\Gamma}_2 &\approx \boldsymbol{\Gamma}_{02} + \mathbf{A}_2\Delta\boldsymbol{\theta}\end{aligned} \tag{5.9}$$

where $\boldsymbol{\Gamma}_{01}$ and $\boldsymbol{\Gamma}_{02}$ are the circulation distributions at flight conditions 1 and 2 at the current estimate of the design variables $\boldsymbol{\theta}$. The matrices $\mathbf{A}_1$ and $\mathbf{A}_2$ are obtained by linearizing Eq. (5.8) and are derived in Appendix A.

Substituting Eq. (5.9) into Eq. (5.7) and setting the variation of Π to zero for

arbitrary changes in the design variables and Lagrange multipliers gives the desired system of linearized equations for the multipoint optimization, i.e.,

$$\begin{bmatrix} \frac{1}{2}\alpha\mathbf{A}_1^T(\mathbf{K}_1+\mathbf{K}_1^T)\mathbf{A}_1+\frac{1}{2}\beta\mathbf{A}_2^T(\mathbf{K}_2+\mathbf{K}_2^T)\mathbf{A}_2 & \mathbf{A}_1^T\mathbf{B}_1^T & \mathbf{A}_1^T\mathbf{D}_1^T & \mathbf{A}_2^T\mathbf{B}_2^T & \mathbf{A}_2^T\mathbf{D}_2^T \\ \mathbf{B}_1\mathbf{A}_1 & \mathbf{0} & \mathbf{0} & \mathbf{0} & \mathbf{0} \\ \mathbf{D}_1\mathbf{A}_1 & \mathbf{0} & \mathbf{0} & \mathbf{0} & \mathbf{0} \\ \mathbf{B}_2\mathbf{A}_2 & \mathbf{0} & \mathbf{0} & \mathbf{0} & \mathbf{0} \\ \mathbf{D}_2\mathbf{A}_2 & \mathbf{0} & \mathbf{0} & \mathbf{0} & \mathbf{0} \end{bmatrix} \begin{Bmatrix} \Delta\boldsymbol{\theta} \\ \boldsymbol{\lambda}_{F1} \\ \boldsymbol{\lambda}_{M1} \\ \boldsymbol{\lambda}_{F2} \\ \boldsymbol{\lambda}_{M2} \end{Bmatrix} \approx$$

$$\begin{Bmatrix} -\alpha(\mathbf{A}_1^T\mathbf{K}_1\boldsymbol{\Gamma}_{01}-\mathbf{k}_{v1})-\beta(\mathbf{A}_2^T\mathbf{K}_2\boldsymbol{\Gamma}_{02}-\mathbf{k}_{v2}) \\ \mathbf{F}_{R1}-\mathbf{B}_1\boldsymbol{\Gamma}_{01} \\ \mathbf{M}_{R1}-\mathbf{D}_1\boldsymbol{\Gamma}_{01} \\ \mathbf{F}_{R2}-\mathbf{B}_2\boldsymbol{\Gamma}_{02} \\ \mathbf{M}_{R2}-\mathbf{D}_2\boldsymbol{\Gamma}_{02} \end{Bmatrix} \quad (5.10)$$

The terms $\mathbf{K}_{v1}$ and $\mathbf{K}_{v1}$ are the gradients of the profile power terms P_{v1} and P_{v2} with respect to the change in design variables and are also derived in Appendix A.

Equation (5.10) describes (approximately) a single Newton step in the direction of the constrained minimum. Because we use piecewise linear C81 tables to describe the profile drag, we omit the Hessian matrix terms associated with the profile power that appears on the left-hand side. Equation (5.10) is solved for the change in the design variables, $\boldsymbol{\Delta\theta}$, and the design variables $\boldsymbol{\theta}$ are then updated. We then update the circulation at each flight condition such that $\mathbf{R}_1(\boldsymbol{\Gamma}_1,\boldsymbol{\theta})=0$ and $\mathbf{R}_2(\boldsymbol{\Gamma}_2,\boldsymbol{\theta})=0$, i.e., we solve for $\boldsymbol{\Gamma}_1$ and $\boldsymbol{\Gamma}_2$ using the vortex lattice solver. Next, we update the matrices $\mathbf{A}_1$ and $\mathbf{A}_2$ at the new set of design variables, and continue iterating until the design variables have converged to a set that satisfies the trim constraints and minimizes the weighted sum of total power. Finally, we repeat this optimization procedure for a range of values of α between 0 and 1 to map out the Pareto frontier. Note that we also include an inequality constraint on the minimum allowable chord value (not shown in Eq. 5.10) to prevent unrealistically small or negative chord distributions. When activated, this constraint is implemented using Mathematical Programming via Augmented Lagrangians.

5.2 Computational Results: Cruise/Cruise Multipoint Optimization

In this section, we apply the multipoint optimization technique to two different rotor systems – a conventional four-bladed rotor and a coaxial rotor system comprised of an upper and lower four-bladed rotor. For each rotor system, we perform a multipoint optimization for two different forward advance ratios. In a later section, we perform a multipoint optimization of these same rotors for a combination of hover and forward flight conditions.

5.2.1 Conventional Rotor

We first perform an optimization analysis for a conventional rotor in forward flight, which is intended to roughly approximate the AH-64 Apache rotor. The coefficient of lift of the vehicle is prescribed to be $C_L = 0.00926$. The rotor has a 10% root cutout and operates at a shaft angle of $-5°$ (tilted forward in the flight direction). We use a NACA0012 airfoil from root to tip and use C81 data tables to model the sectional coefficients of lift and drag based on the local angle of attack and local normal Mach number. Note that this analysis does not account for blade dynamics such as flapping or lead/lag motion (we assume a rigid rotor). Table 5.1 lists the parameters for the two design points analyzed: a low speed advance ratio of $\mu = 0.2$, and a high speed advance ratio of $\mu = 0.5$.

Table 5.1: Conventional Rotor Parameters.

	Hover	Flight Condition 1	Flight Condition 2
Advance ratio, μ	0.0	0.20	0.50
Relative tip Mach number	0.0	0.65	0.90
Coefficient of lift	0.00926	0.00926	0.00926
Shaft angle	0.0°	-5.0°	-5.0°

Using the techniques described in the previous section, we computed the optimal rotors along the Pareto frontier. For these calculations, we used a vortex-lattice mesh

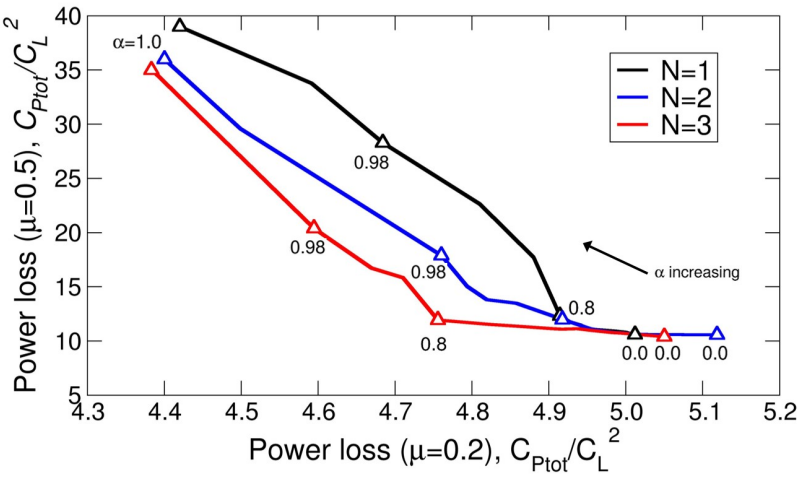

FIGURE 5.2: Pareto frontiers for a conventional rotor using $N = 1$, $N = 2$, and $N = 3$ harmonic control.

with 18 quadrilateral vortex ring elements in the spanwise direction and 15 elements in the azimuthal direction per quarter turn for each of the four blades for a total of 1080 vortex ring elements of unknown strength at each flight condition. Images of these vortex rings are repeated for multiple quarter turn revolutions of the rotor to form a complete wake extending 40 quarter revolutions from the primary lattice.

The computed power loss Pareto frontiers are shown in Figure 5.2 for varying levels of higher harmonic control. The notation $N = 1$ means harmonic blade pitch controls up to 1/rev are used (collective and cyclic); $N = 2$ means harmonics up to 2/rev control are used, and so on. Plotted is the total power loss at $\mu = 0.5$ versus the total power loss at $\mu = 0.2$ along the Pareto frontier. The value of the weighting parameter α decreases as these lines are traversed from left to right, shifting the weighting of the power loss from the $\mu = 0.2$ to the $\mu = 0.5$ flight condition.

We see in Figure 5.2 that there are significant performance tradeoffs to be made when designing a conventional rotor operating at these two disparate flight conditions. Consider first the case of conventional swashplate control ($N = 1$). The most efficient rotor at $\mu = 0.2$ ($\alpha = 1$) is highly inefficient at the high speed ($\mu = 0.5$)

flight condition, with power losses nearly four times the losses for a rotor design to operate only at $\mu = 0.5$ ($\alpha = 0$). Selecting an intermediate value of α that more evenly weights the performance of the rotor at both flight conditions dramatically reduces the total power loss for the high speed condition, with an attendant modest increase in total power loss at the low speed condition. For example, using the rotor found for $\alpha = 0.8$ produces a rotor with near minimum power loss at the high speed flight condition ($\mu = 0.5$), with a power loss at the low speed condition ($\mu = 0.2$) only 11% greater than a single point design at $\mu = 0.2$

Higher harmonic control further reduces the total power loss, pushing the Pareto frontier down and to the left. Note that adding additional degrees of freedom to the design space, in this case higher harmonics of blade pitch control, will always improve the Pareto frontier – or at worst leave it unchanged. Higher harmonic control is seen here to be particularly effective at moving the Pareto frontier for values of α in the range of 0.8 to 0.98. In particular, the $\alpha = 0.8$ solution is seen to move the "knee" or "corner" of the frontier well to the left, producing a rotor with nearly minimum total power loss at the high speed flight condition, with only a small increase in power over the single point minimum at the low speed condition.

Figures 5.3 and 5.4 show the optimal rotor designs using $N = 1$ and $N = 3$ harmonic blade pitch control, respectively, for various values of α. For both levels of harmonic control, the $\alpha = 1.0$ blade (designed to minimize power at $\mu = 0.2$) has a monotonically decreasing twist distribution from root to tip. The rotors optimized using values of α below 1.0, thus including some weighting for the $\mu = 0.5$ flight condition total power loss, instead use a positive twist gradient on the inner 10% of the rotor. Additionally, the $\alpha = 1.0$ (low speed limit) planforms (for both $N = 1$ and $N = 3$) have a large chord on the inboard portion of the blade that tapers towards the tip. The $\alpha = 0.0$ (high speed limit) planforms have narrow chords at the root, with chords increasing to a maximum near a radius of 80% the tip radius. Especially

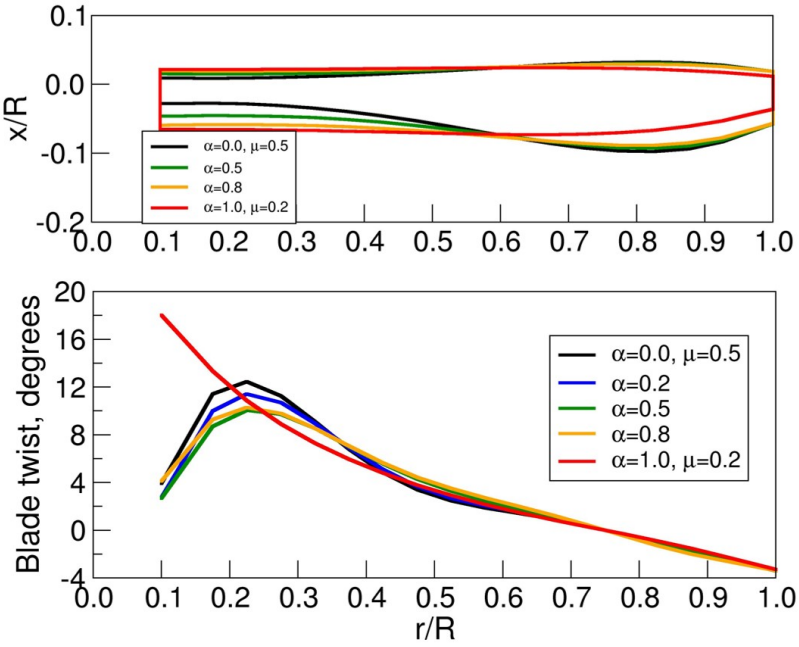

FIGURE 5.3: Optimal rotor designs for $N = 1$ control with varying values of α for a conventional rotor.

for the $N = 3$ case, the chord at the root is unrealistically small. (In an earlier paper, the authors have applied root chord constraints to prevent this problem [40].) For multipoint designs, e.g., $N = 3$ and $\alpha = 0.8$, the blade planform appears quite reasonable, with a nearly constant chord, with a slight bulge in the chord at a radius of 80% and a slight taper outboard.

5.2.2 Coaxial Rotor

Next, we perform a multipoint optimization analysis for a slowed rotor coaxial system of the type found on the Sikorsky X2 Technology Demonstrator (X2 TD), with two coaxial counterrotating four bladed rotors. We optimize the performance between two design points: a low speed flight condition ($\mu = 0.30$), and the high speed design intent advance ratio ($\mu = 0.85$) as described by Bagai [12]. Each rotor has a root cutout of 10% and a vertical separation of 10% of the rotor diameter. Again, we neglect blade dynamics, a reasonable assumption for the rigid rotors used on the

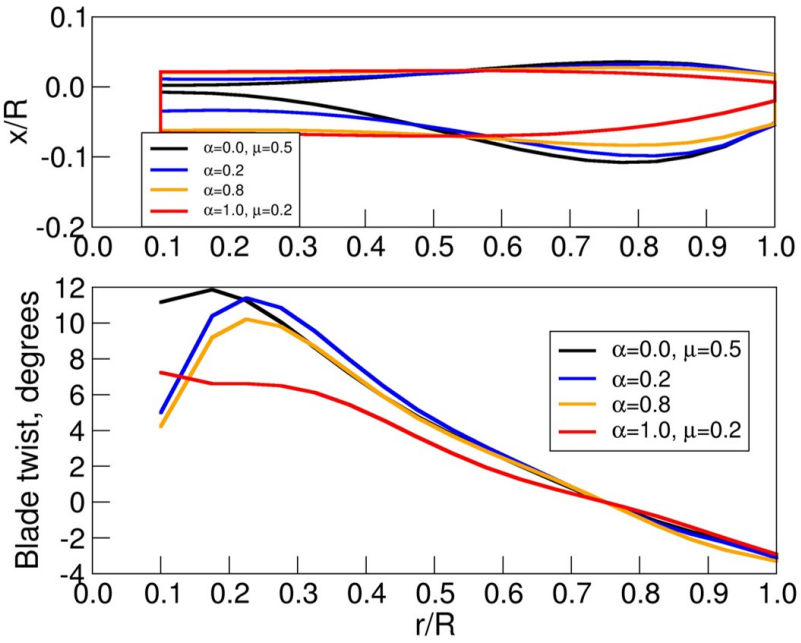

FIGURE 5.4: Optimal rotor designs for $N = 3$ control with varying values of α for a conventional rotor.

Table 5.2: Coaxial Rotor Parameters.

	Hover	Flight Condition 1	Flight Condition 2
Advance ratio, μ	0.0	0.30	0.85
Relative tip Mach number	0.0	0.75	0.90
Coefficient of lift, C_L	0.0166	0.0166	0.0232
Shaft angle	0.0°	-5.0°	-5.0°

X2 TD and other coaxial lift offset rotors. Note that we allow the geometries of the upper and lower rotors to differ from one another.

Because of the difference in rotor speed for the two advance ratios, the nondimensional disk loading will vary between the two advance ratios. Additionally, the tip Mach number will vary based on rotor rotation rate and vehicle speed. Relevant parameters for the two design conditions were estimated using Figures 9 and 10 in a paper by Bagai [12] and are shown in Table 5.2.

The power loss Pareto frontier is shown in Figure 5.5 for varying levels of harmonic

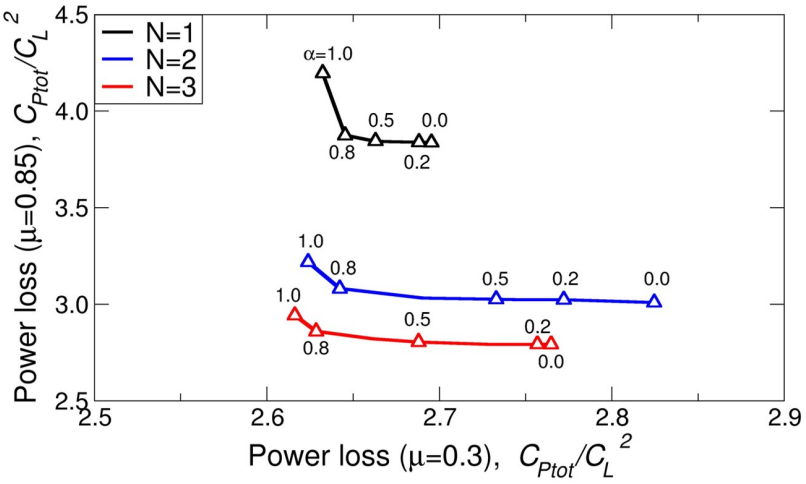

FIGURE 5.5: Pareto frontiers for a coaxial rotor using $N = 1$, $N = 2$, and $N = 3$ harmonic control.

control. Higher harmonic control of the azimuthal blade pitch ($N = 2$ and $N = 3$) dramatically reduces the power loss of optimal rotors at the high-speed flight condition ($\mu = 0.85$). While higher harmonic control does not significantly affect the shape of the Pareto frontier, it significantly reduces power at the high-speed flight condition, improving performance across all values of α. The reductions in power at the low-speed condition ($\mu = 0.3$) are more modest, and only for rotor designs heavily weighted for good performance at the low-speed condition ($\alpha \approx 1$).

Also, each of the Pareto frontiers has a fairly sharp "corner" or "knee," which corresponds to a value of $\alpha \approx 0.8$. For this weighting, the performance of the multipoint optimized coaxial rotor at the two different advance ratios is nearly as good as the performance of rotors optimized separately at these two flight conditions. In other words, there is only a small penalty in performance for designing for the two flight conditions.

Figures 5.6 and 5.7 show the optimal rotor design for $N = 1$ and $N = 3$ harmonic control at varying values of α. Note that while there are some small changes in planform and twist distribution with varying α, in general each of the rotors looks

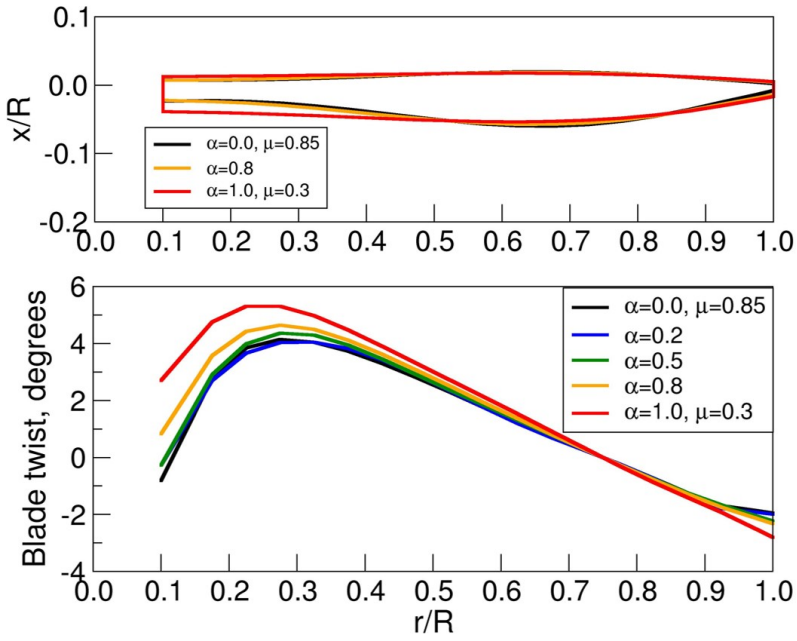

FIGURE 5.6: Optimal rotor designs for $N = 1$ control with varying values of α for a coaxial rotor.

very similar. The similarity of each of these rotors is expected based on Figure 5.5, as the multipoint design would likely be unable to achieve near-optimal performance at both flight conditions if the single point optimal rotors were significantly different. This is again in contrast to the conventional rotor analyzed in the previous section, in which the $\alpha = 0$ and $\alpha = 1$ rotors had significantly different twist and chord distributions that could not be succesfully combined to achieve close to optimal performance at both flight conditions.

5.3 Approach: Hover/Cruise Multipoint Optimization

In this section, we describe a multipoint optimization algorithm for the design of a rotor operating at two flight conditions, one in hover and the other in cruise. The hover flight condition represents an additional challenge, because the hover performance cannot be modeled using the prescribed rigid vortex-lattice wake analysis used for forward flight conditions.

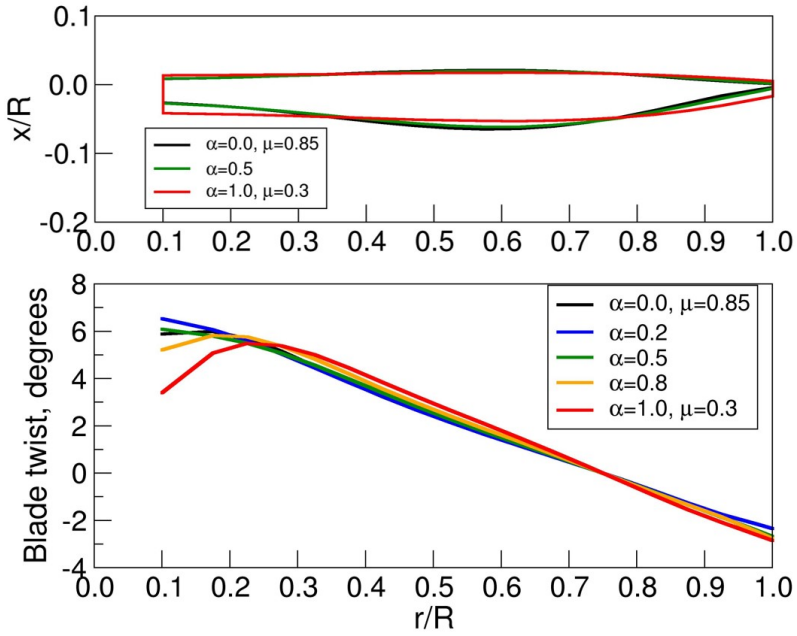

FIGURE 5.7: Optimal rotor designs for $N = 3$ control with varying values of α for a coaxial rotor.

In selecting a method of hover analysis, we seek an approach that is computationally inexpensive, extendable to coaxial rotors, and reasonably accurate. Based on the results of the Chapter 3 coaxial hover optimization and the findings of other researchers [19, 59], we choose to use BEMT to analyze the hovering flight conditions for both conventional and coaxial rotors because of its accuracy, simplicity, and computational efficiency. We choose to neglect the swirl component of induced velocity based on the similarity in performance and optimal rotor design between the swirl and no swirl cases (cf. Chapter 3) and the added complexity of including swirl.

For this analysis, we use the Prandtl tip loss factor to account for the presence of a finite number of blades. We account for the induced velocities of the upper rotor on the inner portion of the lower rotor and assume the upper rotor and outer portion of the lower rotor are unaffected by the mutual interference of the rotors. However, a more refined accounting of the mutual interferences of the rotors can be included in this analysis, for example by using the influence coefficient method described by

Rand and Khromov [20].

The fundamental equations and assumptions for BEMT as applied to coaxial rotors are outlined in Chapter 3.

For a single point optimization of a given hovering or axial flight condition, it is relatively straightforward to determine the spanwise induced wash distribution that results in minimum induced power using the calculus of variations and BEMT as described by Rand and Khromov [20] and as was performed in Chapter 3 for both the swirl and no swirl cases. The profile power can then be minimized at this minimum induced power wash distribution by setting the chord and twist to maximize the value of c_ℓ/c_d at every radial station while maintaining the minimum power induced wash distribution. Note that sequentially minimizing the induced and profile powers is *not* guaranteed to minimize total power. Nevertheless, we have found this approach provides a solution very close to the minimum total power blade design.

This optimization method, although efficient, cannot be combined with our existing forward flight analysis to perform a hover/cruise multipoint optimization. This is because the set of design variables that minimizes our multipoint objective function, Eq. (5.19), is found using Newton iteration, as required by our single point forward flight optimization. In order to mesh the hover optimization with our forward flight model to simultaneously solve our multipoint objective function, the hover optimization must also be solved using Newton iteration. As a result, we cast the hover optimization as a Newton iteration, allowing us to efficiently incorporate hover into the multipoint optimization.

We first consider solving for the optimal single point design of a rotor system in hover using Newton iteration. For a coaxial rotor in hover, we seek to minimize the total power subject to constraints that the upper and lower rotors produce equal and opposite torques, and that the total thrust be equal to a specified value. Thus,

we adjoin to the power the thrust and power constraints using Lagrange multipliers, with the result

$$\Pi = P_{\text{tot}} + \lambda_T(T - T_{\text{R}}) + \lambda_Q(P_{\text{u}} - P_\ell) \tag{5.11}$$

The power and thrust are a function of the design variables, which include the twist and chord distributions the blades of the upper and lower rotors.

To solve the optimization problem with Newton iteration, we start with some initial guess of the design variables θ. We then find the second-order Taylor expansion of the power in terms of the design variables, i.e.,

$$P_{\text{tot}}\left(\boldsymbol{\theta} + \Delta\boldsymbol{\theta}\right) \approx P_{\text{tot}}\left(\boldsymbol{\theta}\right) + \Delta\boldsymbol{\theta}^T \frac{\partial P_{\text{tot}}\left(\boldsymbol{\theta}\right)}{\partial \boldsymbol{\theta}} + \frac{1}{2}\Delta\boldsymbol{\theta}^T \frac{\partial^2 P_{\text{tot}}\left(\boldsymbol{\theta}\right)}{\partial \boldsymbol{\theta}^2}\Delta\boldsymbol{\theta} \tag{5.12}$$

Similarly, the total thrust and the power of the upper and lower rotors can be approximated with the first-order Taylor expansions

$$T\left(\boldsymbol{\theta} + \Delta\boldsymbol{\theta}\right) \approx T\left(\boldsymbol{\theta}\right) + \Delta\boldsymbol{\theta}^T \frac{\partial T\left(\boldsymbol{\theta}\right)}{\partial \boldsymbol{\theta}} \tag{5.13}$$

$$P_{\text{u}}\left(\boldsymbol{\theta} + \Delta\boldsymbol{\theta}\right) \approx P_{\text{u}}\left(\boldsymbol{\theta}\right) + \Delta\boldsymbol{\theta}^T \frac{\partial P_{\text{u}}\left(\boldsymbol{\theta}\right)}{\partial \boldsymbol{\theta}} \tag{5.14}$$

$$P_\ell\left(\boldsymbol{\theta} + \Delta\boldsymbol{\theta}\right) \approx P_\ell\left(\boldsymbol{\theta}\right) + \Delta\boldsymbol{\theta}^T \frac{\partial P_\ell\left(\boldsymbol{\theta}\right)}{\partial \boldsymbol{\theta}} \tag{5.15}$$

Substituting these expansions into Eq. (5.11), and simplifying notation by noting that all values of P and T are those found at the current set of design variables $\boldsymbol{\theta}$, e.g., $P = P\left(\boldsymbol{\theta}\right)$, gives

$$\begin{aligned}\Pi = P_{\text{tot}} &+ \Delta\boldsymbol{\theta}^T \frac{\partial P_{\text{tot}}}{\partial \boldsymbol{\theta}} + \frac{1}{2}\Delta\boldsymbol{\theta}^T \frac{\partial^2 P_{\text{tot}}}{\partial \boldsymbol{\theta}^2}\Delta\boldsymbol{\theta} \\ &+ \lambda_T\left(T\left(\boldsymbol{\theta}\right) + \Delta\boldsymbol{\theta}^T \frac{\partial T}{\partial \boldsymbol{\theta}}_{\text{R}}\right) \\ &+ \lambda_Q\left(P_{\text{u}} + \Delta\boldsymbol{\theta}^T \frac{\partial P_{\text{u}}}{\partial \boldsymbol{\theta}} - P_\ell - \Delta\boldsymbol{\theta}^T \frac{\partial P_\ell}{\partial \boldsymbol{\theta}}\right)\end{aligned} \tag{5.16}$$

Next, to find an estimate of the constrained optimum design, we take the variation of this expression with respect to the change in design variables $\Delta\boldsymbol{\theta}$ and the Lagrange multipliers with the result

$$\begin{aligned}
\delta\Pi &= 0 \\
&= \left(\frac{\partial P_{\text{tot}}}{\partial \boldsymbol{\theta}} + \frac{\partial^2 P_{\text{tot}}}{\partial \boldsymbol{\theta}^2}\Delta\boldsymbol{\theta} + \lambda_T \frac{\partial T}{\partial \boldsymbol{\theta}} - \lambda_Q \left[\frac{\partial P_{\text{u}}}{\partial \boldsymbol{\theta}} - \frac{\partial P_\ell}{\partial \boldsymbol{\theta}}\right]\right)\delta\Delta\boldsymbol{\theta} \\
&+ \left(T + \Delta\boldsymbol{\theta}^T \frac{\partial T}{\partial \boldsymbol{\theta}} - T_{\text{R}}\right)\delta\lambda_T \\
&+ \left(P_{\text{u}} + \Delta\boldsymbol{\theta}^T \frac{\partial P_{\text{u}}}{\partial \boldsymbol{\theta}} - P_\ell - \Delta\boldsymbol{\theta}^T \frac{\partial P_\ell}{\partial \boldsymbol{\theta}}\right)\delta\lambda_Q
\end{aligned} \tag{5.17}$$

Equation (5.17) must be zero for arbitrary variations $\delta\Delta\boldsymbol{\theta}$, $\delta\lambda_T$, and $\delta\lambda_Q$. Therefore, the terms in parentheses must be identically zero. The result is a system of linear equations describing the change in the design variables, i.e.,

$$\begin{bmatrix} \frac{\partial^2 P_{\text{tot}}}{\partial \boldsymbol{\theta}^2} & \frac{\partial T}{\partial \boldsymbol{\theta}}^T & \frac{\partial (P_{\text{u}} - P_\ell)}{\partial \boldsymbol{\theta}}^T \\ \frac{\partial T}{\partial \boldsymbol{\theta}} & 0 & 0 \\ \frac{\partial (P_{\text{u}} - P_\ell)}{\partial \boldsymbol{\theta}} & 0 & 0 \end{bmatrix} \begin{Bmatrix} \Delta\boldsymbol{\theta} \\ \lambda_T \\ \lambda_Q \end{Bmatrix} = \begin{Bmatrix} -\frac{\partial P_{\text{tot}}}{\partial \boldsymbol{\theta}} \\ T_{\text{R}} - T \\ P_\ell - P_{\text{u}} \end{Bmatrix} \tag{5.18}$$

Equation (5.18) is solved for the unknown change in design variables and Lagrange multipliers, and the design variables are updated. The entire process is then repeated until a converged design is found, and is effectively a Newton iteration.

While in reality the power of each rotor is not independent of the other rotor's design variables (for instance, the lower rotor's power is directly affected by the upper rotor's design and resulting wake), in using only first order gradient terms to satisfy the torque constraint, we make the simplifying but incorrect assumption that they are independent, i.e., that the upper rotor design variables only affect the upper rotor's power and that the lower rotor design variables only affect the lower rotor's power. This assumption is acceptable to satisfy the torque constraint, and is not made in the second order expression for total power that we are seeking to minimize.

The algorithm described above is implemented in Fortran 95. The derivative terms in Eq. (5.18) are difficult to express analytically. Instead, we use the Tapenade

automatic differentiation compiler [73] in reverse (adjoint) mode to generate the Fortran code needed to compute the gradient terms, and the forward differentiation mode of Tapenade to generate the code to compute the Hessian matrix.

Having described the single point hover optimization problem, we next consider the multipoint optimization of a rotor operating at two flight conditions, one in hover and one in cruise. We seek to minimize the weighted sum of the total power loss at the two flight conditions, again subject to trim constraints. Thus, our Lagrangian power is given by

$$\begin{aligned}\Pi = \alpha\left(\frac{1}{2}\boldsymbol{\Gamma}_1^T\mathbf{K}_1\boldsymbol{\Gamma}_1 + P_{v1}\right) + \beta P_{\text{tot}} + \boldsymbol{\lambda}_{R1}\cdot\mathbf{R}_1(\boldsymbol{\Gamma}_1,\boldsymbol{\theta}) \\ +\ \boldsymbol{\lambda}_{F1}{}^T\cdot(\mathbf{B}_1\boldsymbol{\Gamma}_1 - \mathbf{F}_{R1}) + \boldsymbol{\lambda}_{M1}{}^T\cdot(\mathbf{D}_1\boldsymbol{\Gamma}_1 - \mathbf{M}_{R1}) \\ +\ \lambda_T(T - T_{\text{R}}) + \lambda_Q(P_{\text{u}} - P_\ell)\end{aligned} \tag{5.19}$$

where the forward flight power is weighted by α and the hover power is weighted by β. By combining the powers from the two disparate flight conditions (and, therefore, very different computational analysis techniques) in this way, we express the multipoint objective function as a simple sum of powers and constraints dependent on common design variables, making the formulation of the multipoint optimization relatively straightforward.

Next, taking the variation of Π and setting the result to zero gives

$$\begin{bmatrix} \frac{1}{2}\alpha\mathbf{A}_1^T(\mathbf{K}_1+\mathbf{K}_1^T)\mathbf{A}_1 + \beta\frac{\partial^2 P_{\text{tot}}}{\partial\boldsymbol{\theta}^2} & \mathbf{A}_1^T\mathbf{B}_1^T & \mathbf{A}_1^T\mathbf{D}_1^T & \frac{\partial T}{\partial\boldsymbol{\theta}}^T & \frac{\partial(P_{\text{u}}-P_\ell)}{\partial\boldsymbol{\theta}}^T \\ \mathbf{B}_1\mathbf{A}_1 & \mathbf{0} & \mathbf{0} & \mathbf{0} & \mathbf{0} \\ \mathbf{D}_1\mathbf{A}_1 & \mathbf{0} & \mathbf{0} & \mathbf{0} & \mathbf{0} \\ \frac{\partial T}{\partial\boldsymbol{\theta}} & \mathbf{0} & \mathbf{0} & \mathbf{0} & \mathbf{0} \\ \frac{\partial(P_{\text{u}}-P_\ell)}{\partial\boldsymbol{\theta}} & \mathbf{0} & \mathbf{0} & \mathbf{0} & \mathbf{0} \end{bmatrix} \begin{Bmatrix} \Delta\boldsymbol{\theta} \\ \boldsymbol{\lambda}_{F1} \\ \boldsymbol{\lambda}_{M1} \\ \lambda_T \\ \lambda_Q \end{Bmatrix} = \\ \begin{Bmatrix} -\alpha(\mathbf{A}_1^T\mathbf{K}_1\boldsymbol{\Gamma}_{01} - \mathbf{k}_{v1}) - \beta\frac{\partial P_{\text{tot}}}{\partial\boldsymbol{\theta}} \\ \mathbf{F}_{R1} - \mathbf{B}_1\boldsymbol{\Gamma}_{01} \\ \mathbf{M}_{R1} - \mathbf{D}_1\boldsymbol{\Gamma}_{01} \\ T_{\text{R}} - T \\ P_\ell - P_{\text{u}} \end{Bmatrix} \tag{5.20}$$

Once we have solved the Eq. (5.20) system of linear equations, we update the total vector of design variables and recompute the thrust and power at the new set of design variables. We then recompute the gradients and Hessian and iterate until the design variables have converged.

5.4 Computational Results: Hover/Cruise Multipoint Optimization

In this section, we apply the multipoint optimization technique to the same two rotor systems previously considered a conventional four-bladed rotor and a coaxial rotor system with four-bladed rotors – but now designed to operate in both hover and high-speed forward flight conditions.

5.4.1 Conventional Rotor

The conventional rotor parameters are given in Table 5.1. For the case considered here, the forward flight power loss (condition 2 in Table 5.1) is weighted by α; the hover total power is weighted by β. For these calculations, we again used a vortex-lattice mesh with 18 quadrilateral vortex ring elements in the spanwise direction and 15 elements in the azimuthal direction per quarter turn for each of the four blades for a total of 1080 vortex ring elements of unknown strength for the forward flight condition, with images of these vortex rings extending 40 quarter revolutions from the primary lattice. For the hover power computations, we discretized the rotor using 18 spanwise stations to match the spanwise discretization for the forward flight mesh.

Figure 5.8 shows the Pareto frontiers for varying levels of harmonic control. Plotted is the inverse of the figure of merit (FOM) versus the high-speed cruise power. We see there is is a large tradeoff in performance between hover performance and cruise performance. No single design can achieve performances close to the single point optimum at both flight conditions, even when using $N = 3$ harmonic control.

Higher harmonic control provides a benefit in the multipoint optimization by reducing power in forward flight, improving the Pareto frontier across all values of α. Note that for all levels of harmonic control, there is a fairly sharp knee around $\alpha = 0.2$. These rotor designs have minimum cruise power loss, with some moderate

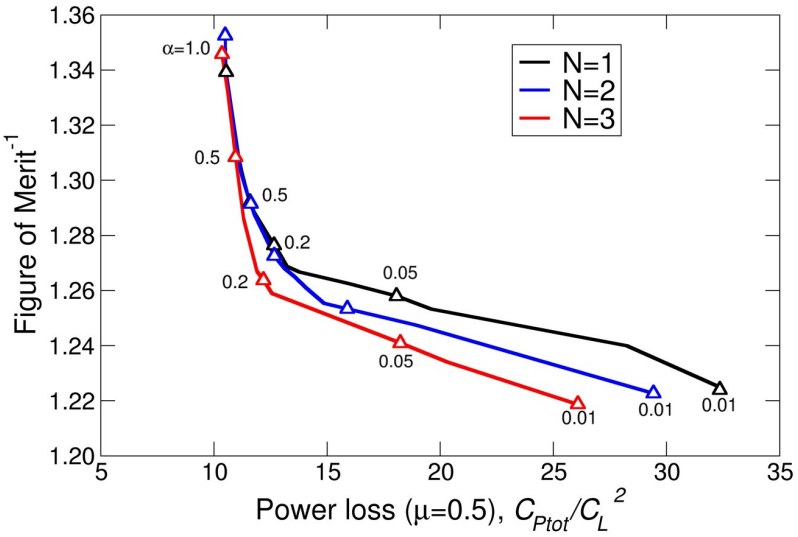

FIGURE 5.8: Hover/cruise Pareto frontiers for a conventional rotor using $N = 1$, $N = 2$, and $N = 3$ harmonic control.

penalty in hover performance.

The single point optimal hovering rotor, which corresponds to a value of $\alpha = 0$ and is shown in Figure 5.9, is not capable of achieving trimmed flight at $\mu = 0.5$, even with $N = 3$ harmonic control. In Figure 5.8, we show results for the low forward flight weighting of $\alpha = 0.01$, which leads to some slight variation in hover performance between the different levels of harmonic control. Note that the single point hovering flight limit ($\alpha = 0$) is the same regardless of the level of harmonic control. Because of the azimuthal symmetry of the hover problem, 1/rev and higher harmonic control cannot reduce power. For reference, the single point optimal hovering rotor has an inverse figure of merit of 1.18.

Figures 5.9 and 5.10 show the optimal conventional rotor designs using $N = 1$ and $N = 3$ harmonic control at varying values of α. Note that the planform and twist distributions of the optimal hovering rotor ($\alpha = 0.0$) and the optimal $\mu = 0.5$ forward flight rotor ($\alpha = 1.0$) are dramatically different. The optimal hovering rotor has the expected hyperbolic twist and chord distribution (modified slightly to maintain optimality with the inclusion of the Prandtl tip loss factor), while the optimal forward flight rotor has a positive twist on the inner 10% of the blade, as

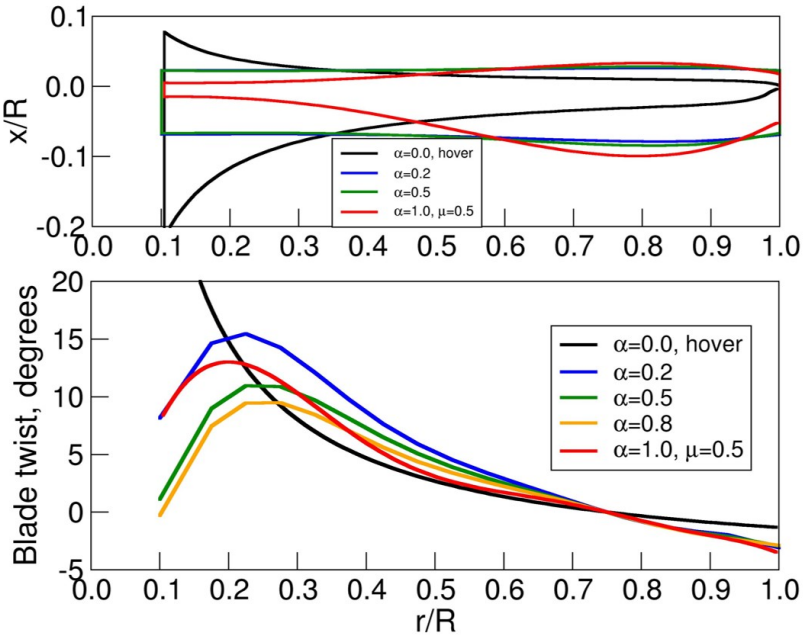

FIGURE 5.9: Optimal hover/cruise multipoint rotor designs for $N = 1$ control with varying values of α for a conventional rotor.

well as a very small inboard chord that increases to a peak chord at a radial position of about 80% span. Varying α tends to blend these two disparate blade designs, although certain features in the optimized hovering rotor, such as the very large twist and chord distributions on the inner portion of the blade, disappear almost immediately with increasing nonzero α.

5.4.2 Coaxial Rotor

We now analyze the coaxial rotor based on the Sikorsky X2 TD as previously described. The rotor parameters are given in Table 5.2. For the case considered here, the forward flight power loss (condition 2 in Table 5.2) is weighted by α; the hover total power is weighted by β. In the hover analysis, we assume a wake contraction ratio of $r_c/R = 0.82$. The figure of merit for the hover condition is defined as $FOM = C_T^{3/2}/\sqrt{2}C_P$. (Note for co-axial rotors, there is not a single standard for measuring figure of merit. Leishman et al. [60] present alternative definitions of the figure of merit.)

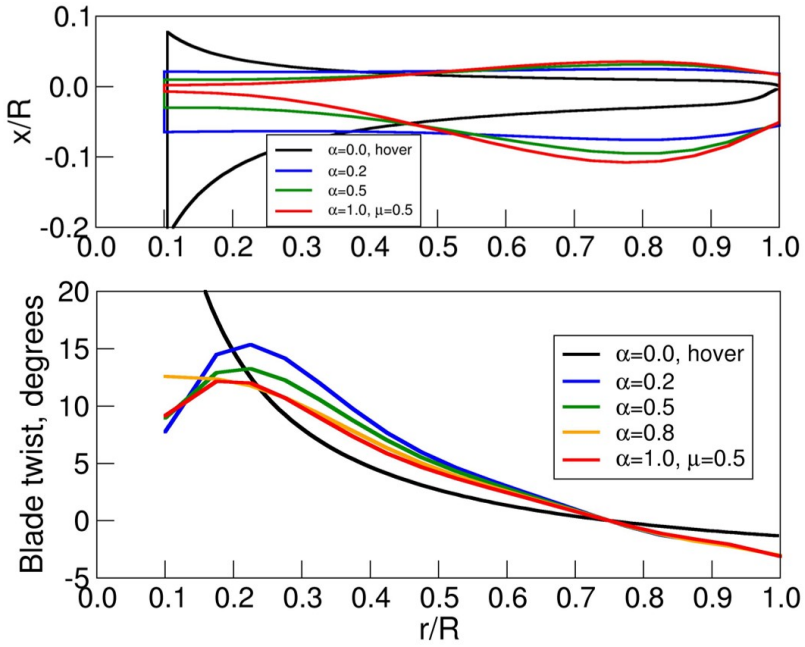

FIGURE 5.10: Optimal hover/cruise multipoint rotor designs for $N = 3$ control with varying values of α for a conventional rotor.

Figure 5.11 shows the computed Pareto frontiers for the coaxial hover/cruise multipoint optimization for varying levels of harmonic control. There is no longer the sharp corner present in the cruise/cruise coaxial multipoint optimization; rather, there is no single rotor design that can achieve close to optimal performance between the two flight conditions. Again, as we expect, higher harmonic control does not provide a benefit to rotors optimized only for hover ($\alpha = 0$). However, $N = 2$ and $N = 3$ control is effective at reducing the optimal hovering rotor's power loss in forward flight. In general, higher harmonic control provides large benefits to performance across the entire Pareto frontier.

It is also interesting to note that a rotor designed only for forward flight ($\alpha = 1$) results in an increase in hovering power of only about 5 to 7 percent above the hover only optimum ($\alpha = 0$), depending on the level of harmonic control. This is in contrast to the high sensitivity of forward flight performance to rotor design, where the $\alpha = 0.0$ hovering rotor results in a three times increase in total power loss at $\mu = 0.85$. Also, we see that there is a knee in the Pareto frontier curves at values of

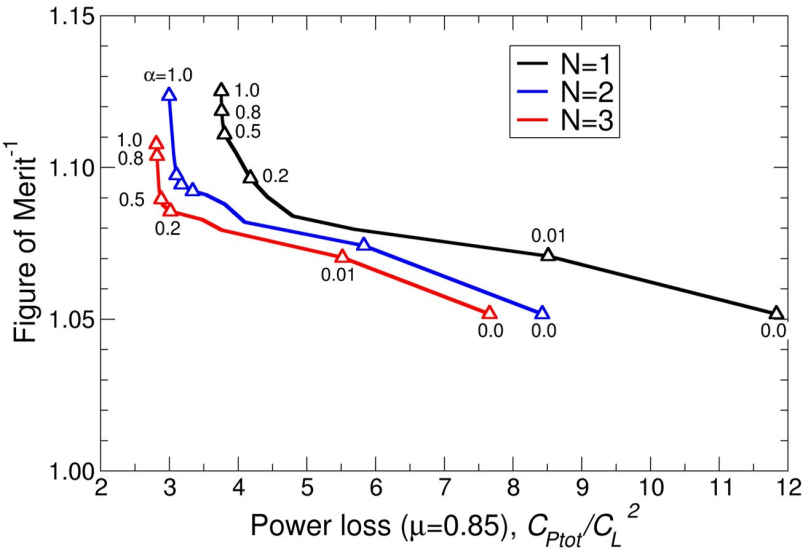

FIGURE 5.11: Hover/cruise Pareto frontiers for a coaxial rotor using $N = 1$, $N = 2$, and $N = 3$ harmonic control.

α of about 0.2, producing rotors with good hover performance with nearly optimal cruise performance.

Figures 5.12 and 5.13 show the $N = 1$ and $N = 3$ optimal rotors at varying values of α. Note that in each of these cases, the twist and chord distribution on the upper and lower rotors are defined by independent sets of design variables; in other words, there is no constraint or requirement that they be equal. The hovering rotor uses significantly different twist and chord distributions on the upper and lower rotor. These differences arise because of the different inflows on the upper and lower rotors in hover. While beneficial in hover, the differences in upper and lower blade design quickly disappear with increased weighting towards the forward flight condition. The $\alpha = 0.2$ rotor shows some slight differences in upper and lower twist, but above this value, the twist of the upper and lower rotor are effectively equal. Furthermore, the planforms of the optimal rotors rapidly approach the $\alpha = 1.0$ design for values of α greater than about 0.2. This rapid convergence to the optimal forward flight rotor is due in part to the high sensitivity of forward flight performance to blade design.

Figure 5.14 shows the circulation distribution for the coaxial rotor using conventional control ($N = 1$) at $\mu = 0.85$ for three levels of α: the hovering optimal

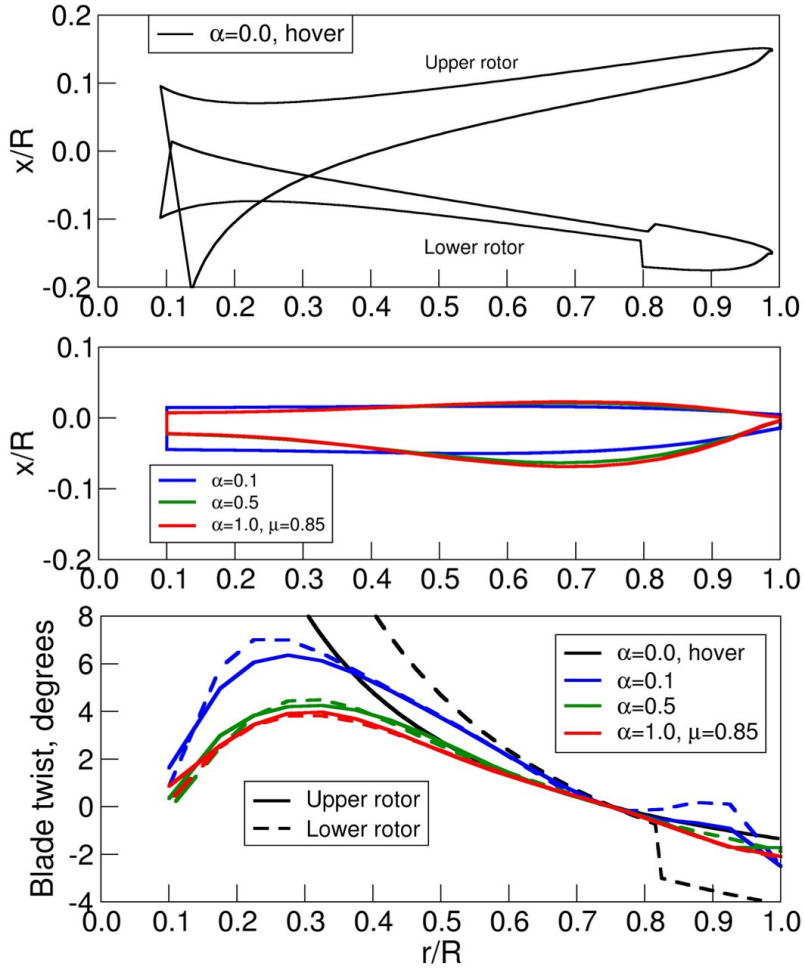

FIGURE 5.12: Optimal hover/cruise multipoint rotor designs for $N = 1$ control with varying values of α for a coaxial rotor.

rotor ($\alpha = 0.0$), the $\mu = 0.85$ optimal rotor ($\alpha = 1.0$), and a rotor determined by multipoint optimization ($\alpha = 0.5$). We see that the optimal hovering rotor, with no consideration of the forward flight power loss in its design, generates regions of very high circulation on the inner portion of the blade on both the advancing and retreating sides, leading to high induced and profile power losses. The $\alpha = 0.5$ rotor, with equal weighting on both flight conditions, generates a circulation distribution that is very similar to – and nearly as efficient efficient as – the $\alpha = 1.0$ rotor while also providing a modest benefit in hover efficiency.

Figure 5.15 shows the same combination of circulation distributions, this time

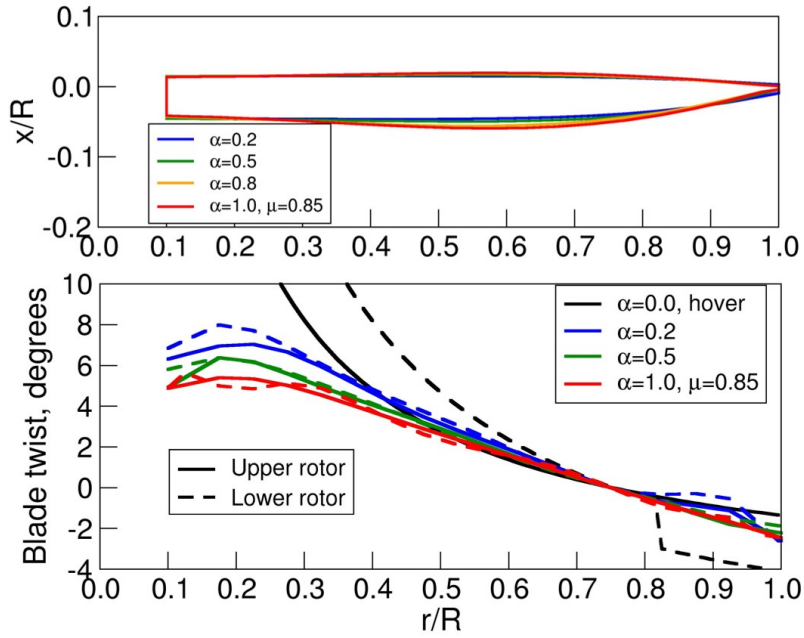

FIGURE 5.13: Optimal hover/cruise multipoint coaxial rotor designs for $N = 3$ control with varying values of α for a coaxial rotor.

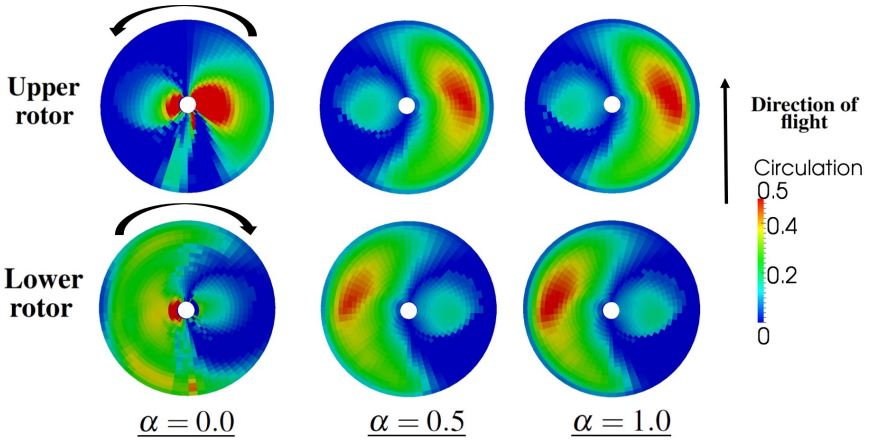

FIGURE 5.14: Normalized circulation distributions for the optimal $N = 1$ coaxial rotor with varying values of α at $\mu = 0.85$.

using $N = 3$ higher harmonic control. The increased degrees of freedom of azimuthal pitch control allow the $\alpha = 1$ rotor to decrease the regions of high circulation in forward flight, particularly on the retreating side, resulting in a lower total power. As in the $N = 1$ case, the $\alpha = 0.5$ rotor nearly replicates the $\alpha = 1.0$ rotor forward flight optimal circulation distribution.

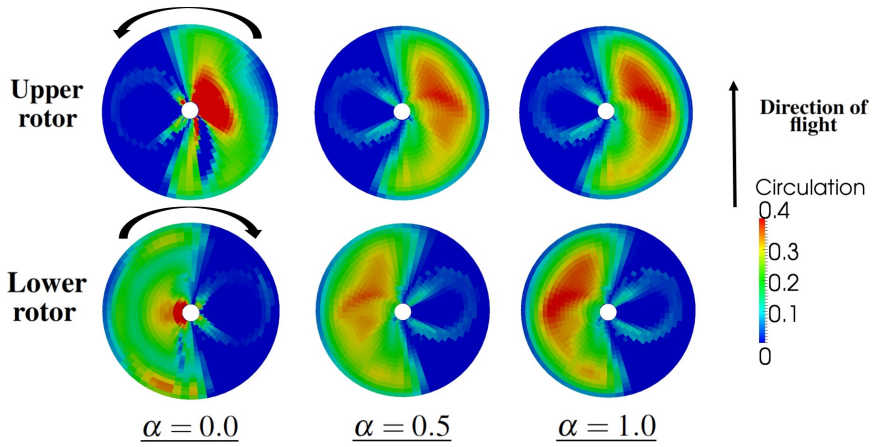

FIGURE 5.15: Normalized circulation distributions for the optimal $N = 3$ coaxial rotor with varying values of α at $\mu = 0.85$.

Finally, Figure 5.16 shows the radial distribution of thrust and total power loss for the $\alpha = 0.0$, $\alpha = 0.5$, and $\alpha = 1.0$ rotors in hover. Without the use of hyperbolic twist and chord distributions and the signficantly different upper and lower twist and chord distributions, the $\alpha = 0.5$ and $\alpha = 1.0$ rotors are unable to match the optimal hovering rotor. In fact, the thrust and power of the $\alpha = 0.5$ rotor much more closely resemble the $\alpha = 1.0$ rotor, as the twist and chord required to match the hovering optimal's thrust and power distributions impose a large penalty on forward flight performance and are therefore eliminated even at small values of α.

5.5 Conclusions

In this chapter, we have described a method of multipoint aerodynamic rotor optimization. The method can be applied to conventional or coaxial rotors, and can be used to optimize performance between any two advance ratios, or a single advance ratio and hover, by minimizing the weighted sum of the aerodynamic losses at two different flight conditions. We used the method to perform cruise/cruise optimization and hover/cruise optimizations on representational conventional and coaxial rotors. Based on the results presented in this paper, we reached the following conclusions:

1. For the conventional rotor optimized for the $\mu = 0.2$ and $\mu = 0.5$ flight conditions, it is not possible to achieve optimal or near optimal performance at both

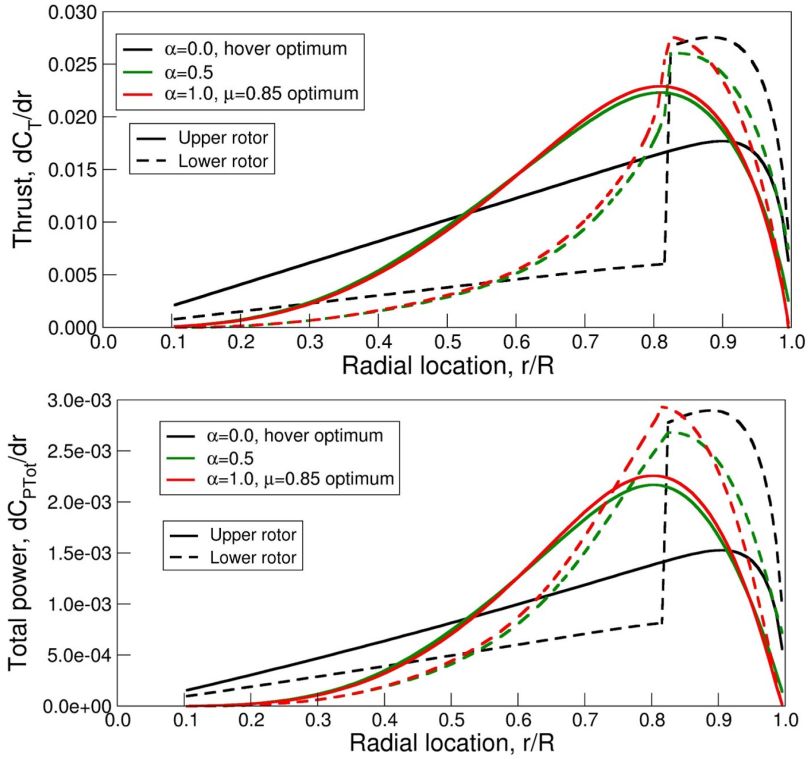

FIGURE 5.16: Radial thrust and total power distributions for the optimal $N = 1$ coaxial rotor in hover with varying values of α.

flight conditions using a single rotor design. As a result, performance tradeoffs must be made in selecting a rotor design. Weighting the $\mu = 0.5$ power loss more heavily results in a moderate penalty in performance at $\mu = 0.2$; however, heavily weighting the $\mu = 0.2$ power loss results in a very large penalty in performance at $\mu = 0.5$, with a total power loss that is three times the single point optimum. As a result, the optimal rotor design quickly approaches the $\mu = 0.5$ optimum with increased values of α (i.e., increased weighting towards the $\mu = 0.5$ flight conditions). Higher harmonic control provides a relatively small benefit at both advance ratios, and is marginally effective at improving the shape and location of the Pareto frontier.

2. For the conventional rotor optimized for hover and forward flight at $\mu = 0.5$, there is a large tradeoff in performance between the two flight conditions. The (single point optimal) hover and forward flight optimal rotor designs are dra-

matically different, and a single rotor design cannot achieve optimal or near optimal performance at both flight conditions. As α is varied, the multipoint optimal rotor blends characteristics from the two single point designs, resulting in balancing of performance between the two flight conditions. In such a case, the desired rotor shape should be carefully selected from designs along the Pareto efficiency curve based on mission requirements. Higher harmonic control once again marginally improves the location of the Pareto efficiency curve across all values of α.

3. For the coaxial rotor optimized for the $\mu = 0.3$ and $\mu = 0.85$ flight conditions, the Pareto efficiency curve has a very sharp corner or "knee," indicating that near optimal performance can be achieved at both flight conditions with a single rotor design. Higher harmonic control significantly reduces power at the $\mu = 0.85$ flight condition, improving the Pareto efficiency curve while not significantly altering its general shape.

4. For the coaxial rotor optimized for hover and $\mu = 0.85$ flight, a substantial tradeoff in performance must again be made between the two flight conditions, as there is no sharp knee in the Pareto curve. However, the forward flight performance of the rotor is more sensitive to changes in rotor design away from the $\mu = 0.85$ optimal rotor, resulting in the multipoint optimum rotor design being dominated by the $\mu = 0.85$ optimal twist and chord distributions, even at small weighting towards this flight condition. For example, certain design characteristics that are beneficial in hover, such as using different blade designs on the upper and lower rotor, impose a large penalty on forward flight performance and are quickly eliminated as the forward flight condition is more heavily weighted. Higher harmonic control substantially improves the location and shape of the Pareto frontier.

6

Conclusions

In this dissertation, we have developed computational models to assess the optimal design and performance of conventional and coaxial helicopters in both hover and forward flight using conventional and higher harmonic control. Conventional helicopters are inefficient in forward flight and have a low maximum flight speed and high power requirements compared to fixed wing aircraft. Compounding the propulsive force of the rotor with an auxiliary source of propulsion such as a propeller can allow for increased top speeds and more efficient flight. Additionally, using a rigid coaxial rotor system within a compound configuration can further improve both forward flight and hover efficiency. The use of higher harmonic control within these compound configurations offers the potential for further aerodynamic performance improvement. Although the implementation of higher harmonic control involves substantial technological challenges, a logical first step is to assess its potential to reduce power loss from a strictly aerodynamic perspective.

6.1 Conclusions

We have investigated two distinct areas of compound and coaxial helicopter design – hover and forward flight performance analysis and optimization – and then joined these two analyses into a single multipoint optimization. We provide here conclusions for each investigation, followed by a summary of more general conclusions and proposed future work.

Optimal design of compound vehicles in forward flight that use higher harmonic control: We investigated the performance and optimal design of a compound vehicle using counter-rotating coaxial rigid rotors, a propeller, and, optionally, a fixed wing. We determined the blade geometry, azimuthal blade pitch inputs, optimal shaft angle (rotor angle of attack), and division of propulsive and lifting forces among the components that minimize the total power for a given forward flight condition. The optimal design problem was cast as a variational statement that is discretized using a vortex lattice wake to model inviscid forces, combined with two-dimensional drag polars to model profile losses. The resulting nonlinear constrained optimization problem was solved via Newton iteration. We found that varying the required propulsive force of the vehicle has a large effect on the optimal shaft angle, which in turn has an effect on the optimal rotor design. Additionally, the optimal shaft angle is strongly dependent on the propeller design and efficiency. As a result, it is important in compound vehicle design to consider the entire propeller/rotor system rather than treating the components separately. The resulting optimal shaft angle will not necessarily result in either the rotor or the propeller operating in a minimum power state.

We also found that for the coaxial case considered, higher harmonic control reduces total vehicle power loss by as much as 15 percent compared to conventional control. Higher harmonic control results in a more efficient rotor system, leading

to an increasingly negative (forward tilted) optimal shaft angle. This allows the rotor system to provide a larger fraction of the vehicle's propulsive force. The use of higher harmonic control reduces both induced and viscous components of power in part by reducing circulation on the retreating side of each rotor and concentrating circulation on the advancing side, resulting in a circulation and lift distribution that more closely resembles the rubber rotor optimum.

Both the conventional and higher harmonic control cases achieve efficient forward flight by operating with a high lateral lift offset equal to about one-half the rotor radius. Such high values of lift offset may not be structurally feasible. Constraining the maximum lateral lift offset of a coaxial rotor system to a smaller value significantly increases the rotor and vehicle power losses. For example, when the maximum lateral lift offset is limited to 30 percent of the rotor radius, total vehicle power loss increases by over 40 percent for both conventional and higher harmonic control.

Higher harmonic control dramatically reduces rotor power losses at negative shaft angles when the maximum lateral lift offset is constrained. At high positive shaft angles, the benefit of higher harmonic control is greatly diminished.

The use of a lifting wing to supplement coaxial rotor lift has a very modest effect on aircraft efficiency, decreasing overall vehicle power loss by less than 1 percent. A wing may be more effective at reducing power if the rotor system is also constrained in lift offset or if a conventional single rotor is used rather than the rigid coaxial design, cases that were not analyzed in this study.

Optimal design of a coaxial rotor in hover: We developed a model to analyze and optimize coaxial rotors in hover. Building on prior work in the field by Leishman and Ananthan [19] and Rand and Khromov [20], we developed a blade element momentum theory model including the swirl component of induced velocity to quantify the effects of swirl on performance, optimal induced wash distribution, and optimal blade twist and chord. The optimization accounts for the presence of a finite

number of blades using the Prandtl tip loss factor, the effect of profile drag using experimentally or computationally determined drag polars, and the mutual interference between the two rotors using an empirically determined influence coefficient method.

We find that the optimal hovering coaxial rotor uses a significantly lower, and in some cases negative, thrust distribution on the inner portion of the lower rotor. The outer portion of the lower rotor, operating outside of the contracted wake of the upper rotor, then generates a majority of the lower rotor's thrust. We determined that the optimal coaxial rotors with and without swirl are nearly identical at radial stations outboard of $r/R = 0.3$. At values of $r/R < 0.3$, the rotors optimized accounting for swirl have signficantly different optimal twist and chord distributions than the non-swirl case. As expected, swirl has a larger effect on performance at higher thrust coefficients. Computations accounting for swirl have an optimal figure of merit 3.5% lower than the equivalent no swirl model at the very high thrust coefficient of $C_T = 0.02$. At the typical disk loadings seen on helicopters, the effect of swirl on rotor design and performance predictions within the framework of blade element momentum theory is relatively small. Other model refinements, such as more detailed wake modeling and improved mutual interference models, may have a larger impact on optimal rotor design and performance predictions than the inclusion of the swirl component of induced velocity. Finally, we found that the optimal coaxial hovering rotor has significantly different twist and chord distributions on the upper and lower rotors, resulting from the different inflow distributions acting on each rotor as a result of their mutual interference. However, using the optimal upper rotor blade design on both rotors leads to a relatively small decrease in performance, indicating that near optimal hover performance can be achieved using the same blade design on the upper and lower rotors.

Axisymmetric potential flow model of single or coaxial actuator disks

in hover: To better understand the mutual interference of coaxial rotors in hover, we modeled the rotor or coaxial rotors as actuator disks (though not necessarily uniformly loaded) and the wake as contracting cylindrical vortex sheets, which we in turn represented as discrete vortex rings. We assumed the system is steady in time and axisymmetric, requiring us to model only a single azimuthal slice of the disk and its wake to determine the shape of the wake and the induced velocity throughout the flowfield. We use multiple vortex sheets, allowing us to analyze any piecewise constant distribution of bound circulation on the disk or disks. We solve for the wake position that results in all vortex sheets being aligned with the streamlines of the flow field via Newton iteration.

We find that the singularity that occurs where the vortex sheet terminates at the edge of the actuator disk is resolved through the formation of a 45° logarithmic spiral in hover, as hypothesized by Spalart [45]. The spiral structure of the wake results in a highly non-uniform inflow that includes reversed flow through the actuator disk near its edge. In axial flight, the size of this spiral decreases, vanishing in the limit where V_c/V_i approaches infinity. In cases of descending flight, the size of the spiral structure increases until the wake enters the vortex ring state, where solutions can not be found using the methods described here. At high descent velocities, the vortex sheet enters a windmill brake state, which also has a spiral-like structure of the same orientation as the climb velocity and hover cases. In this case, flow recirculates not through the actuator disk but around the outer edge of the disk. Actuator disks with multiple vortex sheets still contain the spiral structure, although it is significantly smaller or undetectable on the inboard filaments, and presumably would vanish for smooth distributions of circulation (except at the tip).

Coaxial actuator disks have a pronounced spiral structure on the lower disk, where the upwash induced by the upper disk acts as a descent velocity for the edge of the lower disk. The upper disk sees the opposite effect, with a net downward flow

through the disk induced by the lower disk, reducing the size of the spiral structure and more closely resembling an actuator disk in climbing axial flight. The mutual interference effects predicted by our vortex ring model agree reasonably well with the predictions made using the influence coefficient model of McAlister et al. [49] and used in the coaxial hover optimization described in Chapter 3.

Multipoint Optimization of Conventional and Coaxial Helicopters: Finally, we combined versions of the hover and forward flight optimizations to develop a formal multipoint optimization of conventional and coaxial rotors that can be used to determine the rotor design that best balances performance between hover and cruise, or alternatively, two disparate cruise flight conditions.

For a conventional rotor optimized for hover and forward flight at $\mu = 0.5$, there is a large tradeoff in performance between the two flight conditions. The (single point optimal) hover and forward flight rotor designs are dramatically different, and a single rotor design cannot achieve optimal or near optimal performance at both flight conditions. The multipoint optimal rotor blends characteristics from the two single point designs, resulting in balancing of performance between the two flight conditions. The desired rotor shape should be carefully selected from designs along the Pareto efficiency frontier based on mission requirements. Higher harmonic control marginally improves performance along the Pareto efficiency frontier.

For a coaxial rotor optimized for hover and $\mu = 0.85$ flight, a substantial tradeoff in performance must again be made between the two flight conditions, as there is no sharp knee in the Pareto curve. The performance of the rotor at the high speed forward flight point is more sensitive to changes in rotor design than the hovering flight condition Rotor designs that come the closest to optimal performance at each of the the two flight conditions, therefore, more closely resemble the high speed optimal design. Certain design characteristics that are beneficial in hover, such as using different blade designs on the upper and lower rotor, impose a large

penalty on forward flight performance and are quickly eliminated as the forward flight condition is more heavily weighted. Higher harmonic control substantially improves the location and shape of the Pareto frontier.

6.2 Future Work

There are numerous opportunities for improvement and refinement to the forward flight analysis presented in this dissertation. In the near field analysis used to relate the design variables to the far field circulation, we approximate each blade as a lifting line and the airfoil aerodynamics as quasi-steady, meaning that at each discrete azimuthal position (i.e., time step), the lift and drag coefficients of the blade can be determined from steady airfoil characteristics. While this approach is correct in the limit of low reduced frequency, it does not accurately account for the unsteady effects at work on a rotor, where rapid changes in loading can lead to reduced frequencies of certain harmonics of interest for airloads calculations of up to 0.4 [77]. Unsteady effects, including dynamic stall, can be better modeled either through empirical approximations of nonlinear unsteady stall effects, as was done in the analysis by Egolf et al. [78], through the use of a single panel lifting surface model, as was done in the comprehensive code CAMRAD described by Johnson [79], or through the use of a multiple panel lifting surface model similar to the model investigated by Wachspress and Yu [80]. Including blade dynamics in the analysis is another area for potential improvement, as blade flapping and other structural dynamic effects would clearly change the effective pitch angle and thus the performance of the optimal rotors shown here. It should be noted, however, that with each successive refinement and added layer of complexity, the approach loses some of its utility as a first principles aerodynamic model. The strength of this approach in its current form is its ability to approximate aerodynamic improvements available with various design features and quickly identify the rotor geometry, pitch inputs and lift distribution that

yield optimal aerodynamic performance for any arbitrary compound and/or coaxial configuration. There already exist several validated comprehensive codes capable of analyzing the dynamics and aerodynamics of an existing rotor to great detail, and it was not the goal of this work to develop a method that could in any way replace the predictive capabilities of these existing models.

For the hover model, the next step would be a free wake model similar to the free-vortex model described by Syal and Leishman [21], which uses a Weissinger-L representation of the blade. Once again, however, while the higher fidelity model is more accurate than the simpler BEMT approach, the ability to gain fundamental insights into optimal rotor design can sometime be impeded by the increased complexity.

Finally, for the multipoint optimization, the approach could easily be extended to three or more flight conditions and used to determine a rigorous optimum rotor design for a given mission profile.

Appendix A

Determining Closed Form Expressions for the Gradients of Circulation and Viscous Power

A.1 Determining the Entries of the **A** Matrix

To determine the entries of the **A** matrix, we start with the following expression for circulation at the i^{th} panel, obtained from equating the lift calculated by the Kutta-Joukowski theorem with the definition of the sectional coefficient of lift:

$$L_i = \rho u_i \Gamma_i = \frac{1}{2}\rho {u_i}^2 c_i \left(c_{\ell\alpha}\right)_i \alpha_i \tag{A.1}$$

where ρ is the denisty, u is the velocity normal to the span of the blade, c is the chord value, $c_{\ell\alpha}$ is the lift curve slope, and α is the angle of attack. Solving for the circulation Γ_i gives,

$$\Gamma_i = \frac{1}{2} u_i c_i \left(c_{\ell\alpha}\right)_i \alpha_i \tag{A.2}$$

Taylor expanding this equation and retaining first-order terms to approximate $\Delta\Gamma_i$ due to changes in the local angle of attack α_i and local changes in chord c_i gives

$$\Delta\Gamma_i = \frac{1}{2} u_i c_i \left(c_{\ell\alpha}\right)_i \Delta\alpha_i + \frac{1}{2} u_i c_{li} \Delta c_i \tag{A.3}$$

The $\Delta\alpha_i$ term can be replaced by the sum of two distinct changes in angle of attack: a change in the induced angle of attack, $\Delta\alpha_{\text{ind}_i}$, and a change in the angle of attack due to a change in the design variables vector, which will be referred to as $\Delta\theta_{\text{pitch}_i}$. Thus,

$$\Delta\Gamma_i = \frac{1}{2}u_i c_i \left(c_{\ell\alpha}\right)_i \left(\Delta\theta_{\text{pitch}i} - \Delta\alpha_{\text{ind}_i}\right) + \frac{1}{2}u_i c_{l_i}\Delta c_i \tag{A.4}$$

Next, we wish to put $\Delta\alpha_{\text{ind}_i}$ in terms of a change in the circulation distribution, $\mathbf{\Delta\Gamma}$. Starting with the following definition

$$\alpha_{\text{ind}_i} = \tan^{-1}\left(\frac{w_i}{u_i}\right) \tag{A.5}$$

and Taylor expanding Equation (A.5) in terms of the induced wash, w_i, and retaining first order terms gives

$$\Delta\alpha_{\text{ind}_i} = \left(\frac{1}{1+\left(\frac{w_i}{u_i}\right)^2}\right)\frac{\Delta w_i}{u_i} \tag{A.6}$$

The wash at each panel is related to the circulation through the influence coefficient matrix $\mathbf{W}$:

$$\mathbf{w} = \mathbf{W\Gamma} \tag{A.7}$$

and therefore, to first order

$$\Delta\mathbf{w} = \mathbf{W}\Delta\mathbf{\Gamma} \tag{A.8}$$

and for the i^{th} panel,

$$\Delta w_i = \mathbf{W}_i\Delta\mathbf{\Gamma} \tag{A.9}$$

where $\mathbf{W}_i$ is the i^{th} row of the matrix $\mathbf{W}$. Substituting Equation (A.9) into Equation (A.6) and simplifying gives the following expression for $\Delta\alpha_{\text{ind}_i}$, i.e.,

$$\Delta\alpha_{\text{ind}_i} = \left(\frac{u_i}{{u_i}^2 + {w_i}^2}\right)\mathbf{W}_i\Delta\mathbf{\Gamma} \tag{A.10}$$

Substituting this expression into Equation (A.4) and reorganizing terms gives

$$\Delta\Gamma_i + \frac{1}{2}c_i\left(c_{\ell\alpha}\right)_i\left(\frac{{u_i}^2}{{u_i}^2+{w_i}^2}\right)\mathbf{W}_i\Delta\boldsymbol{\Gamma} = \frac{1}{2}u_i c_i\left(c_{\ell\alpha}\right)_i\Delta\theta_{\text{pitch}i} + \frac{1}{2}u_i c_{li}\Delta c_i \tag{A.11}$$

Writing this equation in matrix form gives

$$\mathbf{R}_\Gamma\Delta\boldsymbol{\Gamma} = \mathbf{R}_{\theta\text{Full}}\begin{pmatrix}\Delta\boldsymbol{\theta}_{\text{pitch}}\\ \Delta\mathbf{c}\end{pmatrix} \tag{A.12}$$

with the elements of matrix $\mathbf{R}_\Gamma$ defined as follows:

$$\mathbf{R}_{\Gamma ij} = \delta_{ij} + \frac{1}{2}c_i\left(c_{\ell\alpha}\right)_i\left(\frac{{u_i}^2}{{u_i}^2+{w_i}^2}\right)\mathbf{W}_{ij} \tag{A.13}$$

and with $\mathbf{R}_{\theta\text{Full}}$ made up of two diagonal matrices, $\mathbf{R}_\theta$ and $\mathbf{R}_\text{c}$, with their elements defined in Equations A.15 and A.16:

$$\mathbf{R}_{\theta\text{Full}} = \{\mathbf{R}_\theta|\mathbf{R}_\text{c}\} \tag{A.14}$$

$$\mathbf{R}_{\theta ij} = \delta_{ij}\frac{1}{2}u_i c_i\left(c_{\ell\alpha}\right)_i \tag{A.15}$$

$$\mathbf{R}_{\text{c}ij} = \delta_{ij}\frac{1}{2}u_i c_{li} \tag{A.16}$$

Note that in Equation (A.12) the vector $\Delta\boldsymbol{\Gamma}$ is of length M, where M is equal to the number of panels in the vortex lattice grid. The vectors $\Delta\boldsymbol{\theta}$ and $\Delta\mathbf{c}$ are each of length M, and the matrix $\mathbf{R}_{\theta\text{Full}}$ has dimensions $M \times 2M$.

Finally, to relate a small change in the vector of design variables $\boldsymbol{\theta}$ to the change in circulation, we use the $\mathbf{S}_\text{total}$ matrix. This matrix relates the design variables $\boldsymbol{\theta}$ to the value of the chord and blade pitch at every panel in the wake, $\mathbf{c}$ and θ_pitch respectively.

$$\mathbf{S}_\text{total}\theta = \begin{Bmatrix}\theta_\text{pitch}\\ \mathbf{c}\end{Bmatrix} \tag{A.17}$$

We then define $\mathbf{R}_\theta$ as

$$\mathbf{R}_\theta = \mathbf{R}_{\theta\text{Full}}\mathbf{S}_{\text{total}} \tag{A.18}$$

allowing Equation (A.12) to be written as

$$\Delta\boldsymbol{\Gamma} = {\mathbf{R}_\Gamma}^{-1}\mathbf{R}_\theta\Delta\theta_{\text{pitch}} \tag{A.19}$$

The matrices $\mathbf{R}_\Gamma$ and $\mathbf{R}_\theta$ are the Jacobians of $\mathbf{R}$ with respect to $\boldsymbol{\Gamma}$ and $\boldsymbol{\theta}$, respectively. Lastly, defining

$$\mathbf{A} = {\mathbf{R}_\Gamma}^{-1}\mathbf{R}_\theta \tag{A.20}$$

we have formed a single matrix $\mathbf{A}$ of dimensions $M \times h$, where M is the number of panels in the vortex lattice grid and h is the number of design variables, that relates the change in each design variable to the corresponding change in circulation to first order accuracy, as stated in Equation (2.15).

A.2 Determining the Entries of the Vector $\mathbf{K}_v$

We start with the following equation for the viscous power loss at the i^{th} panel in the wake

$$P_{vi} = \frac{\rho u_i^2}{2} c_i c_{di} \Delta A_i \tag{A.21}$$

where ΔA_i is the area of the i^{th} panel in the wake. Taylor expanding in terms of changes in the chord distribution, c, and changes in the coefficient of drag due to changes in the angle of attack θ, and retaining first order terms yields

$$\Delta P_{vi} = \frac{\rho u_i^2}{2} \left(\Delta c_i c_{di} + c_i \left(c_{d\alpha}\right)_i \Delta\alpha_i\right) \Delta A_i \tag{A.22}$$

Expressing the change in angle of attack as two separate components, one due to a change in induced angle of attack and one due to a change in design variables, and

using the expression for $\Delta\alpha_{\text{ind}i}$ from Equation (A.10) gives

$$\Delta P_{vi} = \frac{\rho u_i^2}{2}\left(\Delta c_i c_{di} + c_i\left(c_{d\alpha}\right)_i \Delta\theta_{\text{pitch}i} - c_i\left(c_{d\alpha}\right)_i \left(\frac{u_i}{{u_i}^2 + {w_i}^2}\right)\mathbf{W}_i\Delta\boldsymbol{\Gamma}\right)\Delta A_i \tag{A.23}$$

Using Equation (2.15) to replace $\Delta\boldsymbol{\Gamma}$, and including the matrices $\mathbf{S}_\theta$ and $\mathbf{S}_c$ to put changes in pitch angle $\Delta\boldsymbol{\theta}$ and chord $\Delta\mathbf{c}$ at each panel in terms of the change in design variables $\Delta\boldsymbol{\theta}_\theta$ and $\Delta\boldsymbol{\theta}_c$, gives the following equation

$$\Delta P_{vi} = \mathbf{P}_c^T\mathbf{S}_c\Delta\boldsymbol{\theta}_c + \mathbf{P}_\theta^T\mathbf{S}_\theta\Delta\boldsymbol{\theta}_\theta - \mathbf{P}_\theta^T\mathbf{W}\mathbf{A}\Delta\boldsymbol{\theta} \tag{A.24}$$

This equation shows that the first-order change in viscous power has distinct contributions from the change in chord design variables $\Delta\boldsymbol{\theta}_c$ and the change in pitch angle design variables, $\Delta\boldsymbol{\theta}_\theta$. Additionally, there is a third term that results from the change in circulation due to the change in the entire design variables vector $\Delta\boldsymbol{\theta}$. The elements of the vectors $\mathbf{P}_c$, $\mathbf{P}_\theta$ and $\mathbf{P}_\theta$ are defined as follows

$$\mathbf{P}_{ci} = \frac{\rho u_i^2}{2}c_{di}\Delta A_i \tag{A.25}$$

$$\mathbf{P}_{\theta i} = \frac{\rho u_i^2}{2}c_i\left(c_{d\alpha}\right)_i\Delta A_i \tag{A.26}$$

$$\mathbf{P}_{\theta i} = \frac{\rho u_i^2}{2}c_i\left(c_{d\alpha}\right)_i\left(\frac{u_i}{{u_i}^2 + {w_i}^2}\right)\Delta A_i \tag{A.27}$$

We want to combine the terms on the right hand side of Equation (A.24) into a single vector, $\mathbf{K}_v$, such that

$$\Delta P_v = \mathbf{K}_v^T\Delta\boldsymbol{\theta} \tag{A.28}$$

To form the $\mathbf{K}_v$ matrix, we make use of the fact that the vector $\Delta\boldsymbol{\theta}$ is simply a concatenation of the $\Delta\boldsymbol{\theta}_\theta$ and $\Delta\boldsymbol{\theta}_c$ vectors, as shown in Equation (5.6), allowing us to sum components of Equation (A.24) as follows

$$\mathbf{K}_v = \left\{\begin{array}{c}\mathbf{S}_\theta^T\mathbf{P}_\theta \\ \mathbf{S}_c^T\mathbf{P}_c\end{array}\right\} + \left\{\begin{array}{c}\mathbf{A}^T\mathbf{W}^T\mathbf{P}_\theta\end{array}\right\} \tag{A.29}$$

Note that the vector $\mathbf{A}^T\mathbf{W}^T\mathbf{P}_\theta$ is of length h, meaning it has an entry for each design variable. The vector $\mathbf{S}_\theta^T\mathbf{P}_\theta$ has an entry for each twist design variable, while the vector $\mathbf{S}_c^T\mathbf{P}_c$ has an entry for each chord design variable, making the concatenation of these two vectors of length h as well and allowing the two vectors to be summed.

Bibliography

[1] K.C. Hall and S.R. Hall. A variational method for computing the optimal aerodynamic performance of conventional and compound helicopters. *Journal of the American Helicopter Society*, 55(4):42006 – 1, 2010.

[2] R. A. Ormiston. A new formulation for lifting rotor performance including comparison with full-scale data. In *American Helicopter Society 64th Annual Forum Proceedings*, Montreal, Canada, April 29–May 1 2008.

[3] J. G. Leishman. *Principles of Helicopter Aerodynamics with CD Extra*. Cambridge university press, 2006.

[4] W. Johnson. *Helicopter theory*. Courier Corporation, 2012.

[5] R. A. Ormiston. Applications of the induced power model and performance of conventional and advanced rotorcraft. In *American Helicopter Society Aeromechanics Specialists' Conference*, San Francisco, CA, January 20–22 2010.

[6] M. Orchard and S. Newman. The fundamental configuration and design of the compound helicopter. *Proc. Institution of Mechanical Engineers, Part G: Journal of Aerospace Engineering*, 217, 2013.

[7] A. M. Moodie and H. Yeo. Design of a cruise-efficient compound helicopter. *Journal of the American Helicopter Society*, 57(3), 2012.

[8] J. W. R. Taylor and F. T. Jane. *Jane's All the World's Aircraft, 1965-66*. McGraw-Hill Book Company, 1969.

[9] J. Paur. X3 helicopter sets speed record at nearly 300 mph. Internet article: http://www.wired.com/autopia/2013/06/eurocopter-x3-speed-record/, June 2013.

[10] D. Quick. Eurocopter's x3 hybrid helicopter demonstrator reaches 180 knot milestone. Internet article: http://www.gizmag.com/eurocopter-x3-hybrid-helicopter-demonstrator/17253/, December 2010.

[11] Advancing Blade Concept. Technology demonstrator. applied technology laboratory. *US Army Research and Technology Laboratories (AVRADC0M), Fort Eustis, VA*, 1977.

[12] A. Bagai. Aerodynamic design of the x2 technology demonstrator main rotor blade. In *American Helicopter Society 64th Annual Forum Proceedings*, Montreal, Canada, April 29– May 1 2008.

[13] J. Croft. Sikorsky x2 hits 250 kt goal. http://www.flightglobal.com/news/articles/sikorsky-x2-hits-250kt-goal-347379/, September 2010.

[14] M. Hirschberg. Raider rolls out. *Vertiflite*, 60(6), 2014.

[15] D. Quick. Sikorsky's x2 demonstrator sets unofficial world record speed of 250 knots. Internet article: http://www.gizmag.com/sikorsky-x2-demonstrator-250-knot-milestone/16424/, September 2010.

[16] W. Johnson. Influence of lift offset on rotorcraft performance. In *American Helicopter Society Specialist's Conference on Aeromechanics*, San Francisco, California, January 23– 25 2008.

[17] C. P. Coleman. A survey of theoretical and experimental coaxial rotor aerodynamic research. In *19th European Rotorcraft Conference*, Cernobbio-Como, Italy, September 1993.

[18] T. Nagashima and K. Nakanishi. Optimum performance and wake geometry of a co-axial rotor in hover. *Vertica*, 7(3):225 – 239, 1983.

[19] J. G. Leishman and S. Ananthan. An optimum coaxial rotor system for axial flight. *Journal of the American Helicopter Society*, 53(4):366 – 381, 2008.

[20] O. Rand and V. Khromov. Aerodynamic optimization of coaxial rotor in hover and axial flight. In *27th International Congress of the Aeronautical Sciences*, 2010.

[21] M. Syal and J. G. Leishman. Aerodynamic optimization study of a coaxial rotor in hovering flight. *Journal of the American Helicopter Society*, 57(4):1 – 15, 2012.

[22] H. Yeo and W. Johnson. Optimum design of a compound helicopter. *Journal of the American Helicopter Society*, 46(4):1210 – 1221, 2009.

[23] W. Johnson, A. M. Moodie, and H. Yeo. Design and performance of lift-offset rotorcraft for short-haul missions. Technical report, DTIC Document, 2012.

[24] C. Russell and W. Johnson. Exploration of configuration options for a large civil compound helicopter. In *American Helicopter Society 69th Annual Forum*, Phoenix, Arizona, May 21– 23 2013.

[25] O. Rand and V. Khromov. Compound helicopter: Insight and optimization. In *American Helicopter Society 69th Annual Forum*, Phoenix, Arizona, May 21–23 2013.

[26] W. Stewart. Second harmonic control on the helicopter rotor. *Aeronautical Research Council R & M*, 2997, 1952.

[27] P.R. Payne. Higher harmonic rotor control: the possibilities of third and higher harmonic feathering for delaying the stall limit in helicopters. *Aircraft Engineering and Aerospace Technology*, 30(8):222–226, 1958.

[28] P. J. Arcidiacono. Theoretical performance of helicopters having second and higher harmonic feathering control. *Journal of the American Helicopter Society*, 6(2):8–19, 1961.

[29] R.C. Moffitt and J.R. Bissell. Theory and application of optimum airloads to rotors in hover and forward flight. In *American Helicopter Society 38th Annual Forum Proceedings*, Anaheim, CA, May 4 –7 1982.

[30] R.C. Moffitt and S. Rivera. An implicit multi-point lifting line optimizer for twist and chord. In *American Helicopter Society International Technical Specialists' Meeting on Rotorcraft Multidisciplinary Design Optimization*, Atlanta, GA, April 27–28 1993.

[31] S. R. Hall, K. Y. Yang, and K. C. Hall. Helicopter rotor lift distributions for minimum-induced power loss. *Journal of Aircraft*, 31(4):837 – 845, July – August 1994.

[32] R. Cheng, T. R. Theodore, and R. Celi. Effects of higher harmonic control on rotor performance. In *American Helicopter Society 56th Annual Forum*, Virginia Beach, Virginia, May 2– 4 2000.

[33] R.A. Ormiston. Induced power of the helicopter rotor. In *American Helicoper Society 60th Annual Forum and Technology Display*, Baltimore, MD, June 8–10 2004.

[34] R.A. Ormiston. Further investigations of helicopter rotor induced power. In *American Helicopter Society 61st Annual Forum Proceedings*, Grapevine, TX, June 1–3 2005.

[35] D. A. Wachspress, T. R. Quackenbush, and C. L. Solomon. On minimum induced power of the helicopter rotor. In *American Helicopter Society's 61st Annual Forum*, Grapevine, Texas, June 2005.

[36] J. Shaw, N. Albion, E.J. Jr. Hanker, and R. S. Teal. Higher harmonic control: Wind tunnel demonstration of fully effective vibratory hub force suppression. *Journal of the American Helicopter Society*, 34(1):14–25, 1989.

[37] S. A. Jacklin, K.Q. Nguyen, A. Blass, and P. Richter. Full-scale wind tunnel test of a helicopter individual blade control system. In *American Helicopter Society 50th Annual Forum*, Washington, D.C., May 1994.

[38] S. A. Jacklin, A. Blass, S. M. Swanson, and D. Teves. Second test of a helicopter individual blade control system in the nasa ames 40- by 80-foot wind tunnel. In *Proceedings of the American Helicopter Society 2nd International Aeromechanics Specialists' Conference*, Bridgeport, Connecticut, October 1995.

[39] S. Goldstein. On the vortex theory of screw propellers. *Proceedings of the Royal Society of London. Series A*, 123(792):440–465, 1929.

[40] K. C. Hall and E. B. Giovanetti. Minimum power requirements and optimal rotor design for conventional and compound helicopters using higher harmonic control. In *American Helicopter Society's 69th Annual Forum*, Phoenix, Arizona, May 2013.

[41] E. B. Giovanetti. Minimum power requirements and optimal rotor design for conventional, compound, and coaxial helicopters using higher harmonic control. Master's thesis, Duke University, 2013.

[42] E. B. Giovanetti and K. C. Hall. Optimum design of compound helicopters using higher harmonic control. In *American Helicopter Society's 70th Annual Forum*, Montreal, Canada, May 2014.

[43] E. B. Giovanetti and K. C. Hall. Optimum design of compound helicopters that use higher harmonic control. *Journal of Aircraft*, 41(1):104–109, 2015.

[44] E. B. Giovanetti and K. C. Hall. Minimum loss load, twist, and chord distributions for coaxial helicopters in hover. In *American Helicopter Society's 71st Annual Forum*, Virgina Beach, Virginia, May 2015.

[45] P. R. Spalart. On the simple actuator disk. *Journal of fluid mechanics*, 494:399–405, 2003.

[46] G. H. Schmidt and J. A. Sparenberg. On the edge singularity of an actuator disk with large constant normal load. *Journal of Ship Research*, 21(2), 1977.

[47] J. T. Conway. Exact actuator disk solutions for non-uniform heavy loading and slipstream contraction. *Journal of Fluid Mechanics*, 365:235–267, 1998.

[48] M. D. Greenberg and S. R. Powers. Nonlinear actuator disk theory and flow field calculations, including nonuniform loading. Technical report, 1970.

[49] K. W. McAlister, C. Tung, O. Rand, and V. Khromov. Experimental and numerical study of a model coaxial rotor. In *American Helicopter Society 62nd Annual Forum Proceedings*, Phoenix, Arizona, May 2006.

[50] E. B. Giovanetti and K. C. Hall. Axisymmetric potential flow model of single or coaxial actuator disks. In *American Helicopter Society's 72nd Annual Forum*, West Palm Beach, Florida, May 2016.

[51] E. B. Giovanetti and K. C. Hall. A variational approach to multipoint aerodynamic optimization of conventional and coaxial helicopter rotors. In *American Helicopter Society's 71st Annual Forum*, Virgina Beach, Virginia, May 2015.

[52] R.A. Ormiston. An analytical formulation for lifting rotor induced power. In *AHS International 65th Annual Forum and Technology Display*, Grapevine, TX, May 27–29 2009.

[53] G. Jacobellis, F. Gandhi, and M. Floros. A physics-based approach to trim optimization of coaxial helicopters in high-speed flight. In *American Helicopter Society 71st Annual Forum Proceedings*, Virginia Beach, Virginia, May 2015.

[54] R. H. Miller. On the computation of airloads acting on rotor blades in forward flight. *Journal of the American Helicopter Society*, 7(2):56–66, 1962.

[55] R. H. Miller. Rotor blade harmonic air loading. *AIAA Journal*, 2(7):1254–1269, 1964.

[56] R.A. Ormiston. On the definitions of rotor and rotorcraft power and performance. In *AHS International 69th Annual Forum and Technology Display*, Phoenix, AZ, May 21–23 2013.

[57] R.D. Harrington. Full-scale-tunnel investigation of the static-thrust performance of a coaxial helicopter rotor. Technical Report TN 2318, NACA, 1951.

[58] A. Gessow. Effect of rotor-blade twist and plan-form taper on helicopter hovering performance. Technical Report TN 1542, NACA, 1948.

[59] O. Juhasz, M. Syal, R. Celi, V. Khromov, O. Rand, G. Ruzicka, and R. Strawn. Comparison of three coaxial aerodynamic prediction methods including validation with model test data. *Journal of the American Helicopter Society*, 59(3):1 – 14, 2014.

[60] J. G. Leishman and M. Syal. Figure of merit definition for coaxial rotors. *Journal of the American Helicopter Society*, 53(3):290 – 300, 2008.

[61] R. Modarres and D. Peters. A compact momentum theory including swirl. In *American Helicopter Society 69th Annual Forum*, Phoenix, Arizona, May 21–23 2013.

[62] A. Betz. Schraubenpropeller mit geringstem energieverlust. mit einem zusatz von l. prandtl. *Nachrichten von der Gesellschaft der Wissenschaften zu Göttingen, Mathematisch-Physikalische Klasse*, 1919:193–217, 1919.

[63] ed. Durand, W.F. *Aerodynamic Theory, Vol. IV*, volume 4. Dover Publications, 1980.

[64] W. J. M. Rankine. *On the mechanical principles of the action of propellers*. RINA, 1865.

[65] R. E. Froude. On the part played in propulsion by differences of fluid pressure. *Transactions of the Institute of Naval Architects*, 30:390 – 405, 1889.

[66] G.R. Hough and D.E. Ordway. The generalized actuator disk. Technical report, DTIC Document, 1964.

[67] J. T. Conway. Analytical solutions for the actuator disk with variable radial distribution of load. *Journal of Fluid Mechanics*, 297:327 – 355, 1995.

[68] J. T. Conway. Exact actuator disk solutions for non-uniform heavy loading and slipstream contraction. *Journal of Fluid Mechanics*, 365:235 – 267, 1998.

[69] B. D. Cox. *Vortex ring solutions of axisymmetric propeller flow problems*. MIT Department of Naval Architecture and Marine Engineering, 1968.

[70] F. W. Lanchester. A contribution to the theory of propulsion and the screw propeller. *Journal of the American Society for Naval Engineers*, 27(2):509–510, 1915.

[71] G. A. M. van Kuik. On the revision of the actuator disc momentum theory. *Wind Engineering*, 15(5):276–289, 1991.

[72] D. I. Pullin. The large-scale structure of unsteady self-similar rolled-up vortex sheets. *Journal of Fluid Mechanics*, 88(03):401–430, 1978.

[73] L. Hascoet and V. Pascual. *Tapenade 2.1 User's Guide*. Project Tropics, INRIA Sophia-Antipolis, 2004.

[74] A. Brand, M. Dreier, R. Kisor, and T. Wood. The nature of vortex ring state. In *American Helicopter Society 63rd Annual Forum Proceedings*, Virginia Beach, Virginia, May 2007.

[75] H. Yeo and W. Johnson. Investigation of maximum blade loading capability of lift-offset rotors. *Journal of the American Helicopter Society*, 59(1):1–12, 2014.

[76] R. E. Steuer. *Multiple Criteria Optimization: Theory, Computation, and Application*. New York: John Wiley and Sons Inc., 1986.

[77] A. Datta. Fundamental understanding, prediction and validation of rotor vibratory loads in steady-level flight. 2004.

[78] T. A. Egolf and A. J. Landgrebe. Helicopter rotor wake geometry and its influence in forward flight. volume 1. generalized wake geometry and wake effect on rotor airloads and performance. Technical report, DTIC Document, 1983.

[79] W. Johnson. A comprehensive analytical model of rotorcraft aerodynamics and dynamics. part 1. analysis development. Technical report, DTIC Document, 1980.

[80] D. A. Wachspress and M. K. Yu. Lifting surface blade model for comprehensive rotorcraft analysis. In *American Helicopter Society's 71st Annual Forum*, Virginia Beach, Virginia, May 2015.

Biography

Eli Battista Giovanetti was born August 8, 1987 in Charlottesville, Virginia. In 2009, Eli received his Bachelor of Science degree with distinction in Mechanical Engineering from the University of Virginia. Following graduation, Eli worked for two years as an engineer at the Knolls Atomic Power Laboratory in Niskayuna, New York. In 2013, Eli received his Master of Science degree in Mechanical Engineering from Duke University with a thesis titled "Minimum Power Requirements and Optimal Rotor Design of Conventional, Compound, and Coaxial Helicopters Using Higher Harmonic Control." Eli received his PhD from Duke University in 2015.

Eli has been supported by various funding sources and awards throughout his graduate career. In 2011, he received the Pratt-Gardner fellowship for first year PhD students. In 2013, Eli won the National Defense Science and Engineering Graduate (NDSEG) Fellowship. The same year, he was also selected as the winner of the Charles H. Kaman Scholarship through the Vertical Flight Foundation. In 2014, Eli was the South East region's winner of the American Helicopter Society's Robert L. Lichten Award.